**Universidad de Oviedo**
***Universidá d'Uviéu***
***University of Oviedo***

**PhD Thesis**

---

# Development and optimization of reconfigurable planar lenses and reflectors

---

Author
**Pablo Alcón García**

Supervisor
**Luis Fernando Herrán Ontañón**

**June, 2017**

**Programa de Doctorado en Tecnologías de la Información y Comunicaciones en Redes Móviles**

# RESUMEN DEL CONTENIDO DE TESIS DOCTORAL

| **1.- Título de la Tesis** | |
|---|---|
| Español/Otro Idioma: Desarrollo y optimización de lentes y reflectores planos reconfigurables | Inglés: Development and optimization of reconfigurable planar lenses and reflectors |

| **2.- Autor** | |
|---|---|
| Nombre: Pablo Alcón García | DNI/Pasaporte/NIE: |
| Programa de Doctorado: Tecnologías de la Información y Comunicaciones en Redes Móviles (TICRM) | |
| Órgano responsable: Comisión Académica del Programa de Doctorado de Tecnologías de la Información y Comunicaciones en Redes Móviles | |

## RESUMEN (en español)

Las antenas reconfigurables, capaces de conformar diferentes diagramas de radiación, son usadas en muchas aplicaciones de radio frecuencia. Entre las distintas antenas, los arrays de reflectores y las lentes reconfigurables son interesantes debido a la ausencia de red de distribución, que ahorra en costes y complejidad de fabricación. Además, el método de onda guiada permite que dichos arrays sean diseñados de forma modular: los elementos radiantes y los desfasadores son optimizados independientemente. Para obtener la mejor capacidad de reconfiguración, el desfasador debe ser continuo, ofreciendo un rango de control de fase completo, con bajas pérdidas inserción y variación de las mismas, manteniendo un tamaño de circuito pequeño que permita reducir la separación entre los elementos del array.
Los desfasadores basados en reflexión (RTPS) usando varactores como cargas ajustables ofrecen buenas características pero necesitan mejoras, ya que las implementaciones tradicionales son costosas, provocan incremento del tamaño de circuito o requieren elementos concentrados cuyos parásitos deterioran el rendimiento. Para solucionarlo, esta tesis introduce el acoplador híbrido transformador de impedancia compleja, capaz de realizar el rol de un híbrido de coeficiente de acoplamiento arbitrario junto a la adaptación de dos impedancias complejas en cada par de puertos aislados. La elección de la impedancia de adaptación define el rendimiento del desfasador, permitiendo elegir diferentes distintas soluciones con relaciones de compromiso entre rango de control de fase y pérdidas, mientras se mantiene un circuito compacto. Esta estructura es utilizada para fabricar un prototipo de desfasador a 9 GHz, obteniendo un rango de fase de 180º, que triplica la que se obtendría con el mismo varactor y una topología básica, a la vez que se mantiene una variación de pérdidas por debajo de 2.2 dB. Se obtuvo una mayor reducción de las pérdidas a 1.2 dB utilizando resistencias en paralelo, que se habría reducido a 0.3 dB de no ser por sus parásitos.
Una celda de array reflector se diseña típicamente a incidencia normal, pero se demuestra que la adaptación empeora a medida que el ángulo de incidencia de la onda incidente aumenta, afectando potencialmente al comportamiento del desfasador. Es por tanto necesario tener los ángulos de incidencia para lograr adaptación adecuada en cada elemento del array. También se observó que empleando el desfasador por reflexión como red de un solo puerto encaja de mejor manera en el array reflector, y consigue mejoras adicionales en rango de fase y pérdidas, superando las obtenidas por dos RTPS en cascada. Se fabricó un prototipo a 9 GHz, consiguiendo un rango de control de fase de 320º, con unas pérdidas de 3.4 a 5.2 dB, cuya variación puede ser reducida a 1 dB sin afectar al rango de fase si se incorpora una única resistencia en paralelo. Con estos medios, se fabricó un array reflector reconfigurable de 4×4 elementos, logrando barrido de haz de -10º a 30º en acimut y de -20º a 20º en elevación.
En las lentes de array, comunicar la entrada y salida en el método de onda guiada requiere capas adicionales, estructuras más complejas o mayor separación entre elementos. Esta tesis propone en su lugar conectarlas mediante el uso de guía de onda integrada en sustrato, realizando la primera lente de array en dicha tecnología. Asimismo, se presenta un desfasador en SIW basado en ranuras inclinadas cargadas que reemplaza a los RTPS en SIW que se

encuentran en la literatura, logrando rendimiento equivalente en una fracción de su tamaño (con una potencial reducción del 90% en longitud y del 50% en anchura). El prototipo medido proporciona a 9 GHz 180º de rango de fase con pérdidas de 4.2 a 7.5 dB. Se simula el desfasador junto a la lente de array propuesta, logrando barrido de haz. Se fabricó un prototipo de lente de array de 2×2 elementos como prueba de concepto, obteniendo una pequeña corrección del haz principal en broadside.

**RESUMEN (en Inglés)**

Reconfigurable antennas, capable of conforming different radiation patterns, are used on many radio frequency applications. From among these antennas, reconfigurable reflectarrays and array lenses are interesting due to the lack of distribution networks, which save costs and manufacturing complexity. Furthermore, the guided-wave approach to those arrays allows to perform a modular design: the radiating elements and the phase shifter are optimized independently. For the best reconfigurability capabilities, the phase shifter should be continuous, offering full phase control range, low insertion losses and loss variation, while keeping a small circuit footprint for reducing the array element spacing.
Reflection-type phase shifters (RTPS) using varactors as tunable loads offer good characteristics but need improvements, as traditional implementations are costly, incur in increase of circuit size or require lumped components whose parasitics deteriorate performance. To overcome that, this thesis introduces the complex impedance transforming hybrid coupler, capable of fulfilling the role of a hybrid coupler of arbitrary coupling coefficient while matching two different complex impedances in each pair of isolated ports. The choice of the matching impedance defines the performance of the phase shifter, allowing to select trade-offs between phase control range and insertion losses, while maintaining a compact circuit footprint. This structure is employed to manufacture a phase shifter prototype at 9 GHz, obtaining a phase agility of 180º that triples that of the basic topology with the same varactor while keeping insertion loss variation below 2.2 dB. A further reduction of the insertion loss ripple to 1.2 dB is achieved employing parallel resistors, which would have been further reduced to 0.3 dB if not for their packaging parasitics.
A reflectarray cell is typically designed at normal incidence, but it was shown that the matching deteriorates as the incidence angle of the impinging plane wave increases, potentially affecting the phase shifter performance. It is then necessary to take the incidence angles into account to achieve proper matching for each element of the array. It was also observed that employing the RTPS as a one port network fits a reflectarray better, and achieves additional improvements in phase agility and insertion loss, surpassing those of cascaded phase shifters. A prototype was manufactured and measured at 9 GHz obtaining a 320º phase control range with an insertion loss from 3.4 to 5.2 dB, whose variation can be further reduced to 1 dB by a single parallel resistor without affecting the phase agility. With this means, a 4×4 elements reconfigurable reflectarray was fabricated, obtaining beam steering from −10º to 30º in azimuth and from −20º to 20º in elevation.
In the array lens, communicating the input and output layers in the guided-wave approach requires extra layers, more complex structures or increased element spacing. This thesis proposes instead to link them through a substrate integrated waveguide (SIW), making it the first array lens based on that technology. A novel SIW phase shifter is also posited, based on loaded tilted slots that replaces the SIW reflection-type phase shifters found in the literature, obtaining equivalent performance within a fraction of its size (with a potential reduction of 90% in length, and 50% in width). The measured prototype bestows at 9 GHz 180ºphase agility with insertion losses from 4.2 to 7.1 dB. The phase shifter is simulated in conjunction with the proposed array lens, realizing beam steering. A 2×2 elements array lens prototype was manufactured as proof of concept, achieving a small beam correction in broadside.

**Universidad de Oviedo**
***Universidá d'Uviéu***
***University of Oviedo***

**PhD Thesis**

---

# Development and optimization of reconfigurable planar lenses and reflectors

---

Author
**Pablo Alcón García**

Supervisor
**Luis Fernando Herrán Ontañón**

**June, 2017**

**Programa de Doctorado en Tecnologías de la Información y Comunicaciones en Redes Móviles**

# Acknowledgments

This work was supported by the Gobierno del Principado de Asturias under the Plan de Ciencia, Tecnología e Innovación (PCTI) by grant BP12-032, by the Ministerio de Economía e Innovación under project TEC2014-54005-P (MIRIIEM) and by the Gobierno del Principado de Asturias/FEDER under project GRUPIN14-114.

# Resumen

Las antenas reconfigurables son dispositivos capaces de producir diferentes diagramas de radiación, ya sea mediante el cambio entre distintas configuraciones fijas o bien a través de conformado de haz adaptativo. Su uso es importante en muchas aplicaciones inalámbricas y de detección incluyendo comunicaciones móviles, de satélites, radares y enlaces terrestres. Las antenas de aperturas tradicionales, tales como reflectores y lentes, pueden ser usadas a tal fin, pero requieren movilidad mecánica para barrido de haz, siendo además el conformado de haz imposible a menos que se usen sofisticados sistemas de alimentación. En contraste, las antenas de array de síntesis de fase permiten ajustes eléctricos alimentando cada elemento del array de antenas con una fase distinta, realizando escaneo de haz en tiempo real. No obstante, su implementación es difícil ya que necesitan redes de distribución complejas, o módulos transceptores para cada elemento del array produciendo altos costes de fabricación. Por el otro lado, los arrays reflectores y las lentes de array son una combinación entre antenas de apertura y arrays de antenas, ofreciendo la alta ganancia de antenas de apertura con la facilidad de fabricación, bajo coste y peso típico de arrays de antenas impresas. Además, la síntesis de fase puede realizarse para cada elemento del array directamente, evitando así la complejidad de otros arrays.

Un array reflector consiste en una antena alimentadora (típicamente una bocina) y un array de elementos radiantes. La antena alimentadora produce una onda electromagnética que se transmite por el espacio e incide sobre el array, siguiendo un camino distinto para cada elemento, que refleja la onda produciendo una corrección de fase distinta. La suma de las ondas reflejadas resultan en un nuevo diagrama de radiación. La antena alimentadora está normalmente desplazada respecto al centro del array para evitar bloquear el diagrama de radiación reflejado.

En una lente de array, el principio de funcionamiento es similar. La antena alimentadora radia una onda electromagnética hacia el array de antenas impresas. Sin embargo, en vez de reflejar la onda corregida, ésta es acoplada a otra capa de antenas, que a su vez radian la onda corregida en fase al lado contrario, resultando en una onda transmitida a través del array. De esta manera, la antena alimentadora no puede bloquear el diagrama de radiación, y puede ser usado no solo en conformado de haz en campo lejano, sino también para obtener puntos focales en la proximidad de la apertura de la lente.

Tanto en los reflectores como en las lentes, el conformado de haz puede hacerse reconfigurable añadiendo elementos ajustables a los arrays. De esta manera, las redes de distribución de los arrays de síntesis de fase son sustituidos por la antena que alimenta el

array, permitiendo la fabricación de antenas reconfigurables de bajo coste y perfil que no requieran movilidad mecánica. Esta tesis consiste en el análisis y optimización de arrays reflectores y lentes de array de bajo coste, confiriendo un entendimiento del proceso de diseño, analizando las mayores restricciones y ofreciendo nuevas soluciones para conseguir la máxima reconfigurabilidad del diagrama de radiación a una única frecuencia de operación.

El objetivo de la tesis es, después de analizar el estado del arte de reflectores y lentes reconfigurables, desarrollar prototipos funcionales de lentes y reflectores reconfigurables de bajo coste empleando desfasadores continuos. Como ejemplo de aplicación serán usados para realizar barrido de haz en banda X. Se prefiere una perspectiva modular siguiendo el método de onda guiada para facilitar la optimización, y por tanto el primero paso consiste en la realización del desfasador más adecuado para ser implementado en los arrays. Las metas de diseño son un rango completo de agilidad de fase de 360° para máximo ajuste de fase, bajas pérdidas de inserción y variación de las mismas para minimizar el efecto de éstas en el diagrama de radiación, y un pequeño tamaño de circuito para reducir la separación entre elementos del array, manteniendo el foco en bajo coste y complejidad. Los desfasadores basados en reflexión ofrecen buenas cualidades, pero están limitados por el rendimiento de la carga ajustable empleada. Las mejoras que se encuentran en la literatura requieren un aumento significativo del tamaño del circuito o el añadido de componentes concentrados cuyos parásitos de empaquetado afectan negativamente al rendimiento del circuito en banda X. La deconstrucción de este tipo de desfasador, centrándose en el acoplador híbrido y los requisitos de la carga ajustable para el mejor resultado, debería conducir a nuevas topologías que otorguen soluciones más adecuadas.

Con la unidad de desfasador establecida, el siguiente objetivo es utilizarla para desarrollar arrays reconfigurables. Ya que el array reflector es la antena más usada de las dos objeto de estudio, debería ser más sencillo realizar la implementación. Basándose en una topología de array reflector fijo, un estudio debería establecer la mejor manera de insertar el desfasador sin tener que realizar grandes cambios. La posibilidad de que el desfasador sea usado como una red de un puerto puede llevar a consideraciones que no fueron tenida en cuenta antes. Debe establecerse un proceso de diseño y posteriormente validarse con un prototipo de array reflector reconfigurable.

El número de lentes de array reconfigurables que pueden encontrarse en la literatura no es tan extenso, y por tanto desarrollar una lente puede requerir el uso de tecnologías que no han sido previamente usadas en ese contexto. Con el objetivo de reducir el número de capas, la complejidad de fabricación y la separación entre elementos, se debe proponer una nueva celda unidad, a la vez que se mantenga el método de onda guiada para favorecer la implementación posterior de mejoras en el desfasador. Se debe diseñar un prototipo para validación experimental.

Finalmente, se deben obtener conclusiones del desarrollo de los arrays reconfigurables, estableciendo las ventajas y desventajas encontradas en el proceso de diseño y sus resultados.

La tesis ha sido dividida en cinco capítulos, comenzando con uno de introducción que describe la motivación del tema de estudio de la tesis, establece los objetivos a cumplir y

presenta los antecedentes tecnológicos en los que se basa el trabajo.

El capítulo 2 ahonda en los desfasadores basados en reflexión, que poseen cualidades apropiadas para arrays de síntesis de fase debido a su bajo coste y casi nulo consumo de potencia. En primer lugar se introducen y analizan redes de adaptación adicionales que controlan el rendimiento del desfasador. Los puertos en los que se encuentran las cargas ajustables son adaptados a impedancias complejas que ofrecen relaciones de compromiso entre control de fase y pérdidas. Debido al requisito de reducir el tamaño del circuito, el acoplador híbrido y las redes de adaptación se combinan en una sola estructura, permitiendo adaptar a distintas impedancias complejas con distintos coeficientes de acoplamiento a la par que se reducen la longitud y anchura de las líneas de transmisión que la componen. Se exploran los límites y ventajas de dicha estructura. Así pues, este nuevo acoplador híbrido transformador de impedancia se usa para fabricar un desfasador optimizado. Finalmente se introducen distintas técnicas para igualar las pérdidas de inserción más allá de lo que era posible en el punto de partida.

El capítulo 3 se centra en la realización de un array reflector ajustable siguiendo el método de onda guiada. Primero se diseña y mide un reflector fijo, teniendo en especial consideración el efecto de los ángulos de incidencia de la onda proveniente de la antena alimentadora, que no son típicamente tenidos en cuenta y pueden afectar drásticamente al comportamiento de la antena. El desfasador basado en reflexión del capítulo 2 es evaluado de nuevo en una topología que se ajusta al reflector más adecuadamente, convirtiéndose en una red de un solo puerto que proporciona mejor agilidad de fase, menores pérdidas de inserción y un tamaño de circuito reducido respecto a las alternativas, ofreciendo a su vez una mayor igualación de pérdidas añadiendo una única resistencia en paralelo. La celda unidad es optimizada para la inclusión del desfasador y se fabrica un prototipo capaz de realizar barrido de haz.

El capítulo 4 trata la problemática del diseño de una lente de array reconfigurable. Puesto que usar tecnología microstrip, como en los capítulos anteriores, resulta en una estructura más complicada, se propone el uso de guía de onda integrada en sustrato, estableciendo un breve análisis del estado del arte de la tecnología y explorando la manera más conveniente de implementar el método de onda guiada. Se propone y fabrica un novedoso desfasador, evitando el uso de acopladores híbridos que ocuparían demasiado espacio, y reemplazando el típico desfasador basado en reflexión por ranuras inclinadas cargadas con impedancias ajustables, resultando en un desfasador de bajo coste considerablemente miniaturizado. Se propone el diseño de la lente de array, logrando barrido de haz en simulación y fabricando un prototipo que sirve como prueba de viabilidad.

Por último, el capítulo 5 resume las conclusiones finales extraídas de cada capítulo, así como las contribuciones más importantes y originales que pueden encontrarse en cada uno de ellos. Se proponen múltiples líneas de investigación para continuar el trabajo presentado en la tesis, que van desde los pasos más lógicos e inmediatos derivados de las limitaciones encontradas hasta propuestas a largo plazo basadas en tecnologías en desarrollo.

# Conclusiones

Esta tesis se ha dedicado al estudio de antenas de tipo reflector y lente reconfigurable, particularmente aquéllas que utilizan el método de onda guiada, que permiten realizar un análisis modular, optimizando por separado el elemento radiante y el desfasador. Los desfasadores continuos ofrecen la mayor reconfigurabilidad, pero están especialmente limitados en agilidad de fase, pérdidas de inserción y tamaño de circuito. Se postula superar esas limitaciones ofreciendo más control de su rendimiento.

En un desfasador basado en reflexión (*Reflection-Type Phase Shifter*, RTPS), una sola carga ajustable no proporciona un rango de control de fase de 360°, y tiene que ser aumentado a través de soluciones que no ofrecen control de rendimiento o requieren de circuitos monolíticos costosos. Se ha presentado una solución alternativa con el añadido de redes de adaptación pasivas, que pueden realizarse con stubs y lineas de transmisión. Es posible modificar el rendimiento del desfasador adaptando las cargas ajustables a impedancias complejas, obteniendo distintas parejas de rango de control de fase y pérdidas de inserción. Se realizó un modelo del diodo varactor comercial Aeroflex MGV-125-258-0805-2 a 9 GHz para analizar el efecto que tendría toda posible red de adaptación en él. Se observó que los puntos de adaptación que proporcionan la mayor agilidad de fase siempre se corresponden con las mayores pérdidas de inserción. Aún así, hay impedancias de adaptación que ofrecen buenas relaciones de compromiso entre fase y pérdidas. También se observó una correlación entre baja variación de pérdidas de inserción y linealidad de fase. Partiendo del rango de fase inicial de 55° que se puede obtener del varactor, se logró un rango de fase de 160° sin afectar significativamente a las pérdidas de inserción. Se puede obtener un mayor incremento a 210° con una variación de pérdidas de inserción por debajo de 3 dB. Esta solución presenta, no obstante, el inconveniente de sufrir un incremento del tamaño de circuito: se necesita no solo un acoplador híbrido, sino también la implementación de redes de adaptación de impedancia. Para evitarlo, la adaptación de impedancia debería realizarse dentro de la estructura del acoplador híbrido.

Los acopladores híbridos de 90° con adaptación de impedancias están restringidos a impedancias reales y están severamente limitados por la viabilidad de la impedancia requerida por sus líneas de transmisión. Esta tesis establece que añadiendo a cada puerto líneas de impedancia y longitud arbitraria, es posible incrementar el rango de impedancias a las que se puede adaptar. Un análisis par-impar de la estructura define los valores de impedancia y longitud de cada una de las líneas de transmisión que conforman la estructura para obtener la adaptación de impedancia deseada en cada puerto, con distintos coefi-

cientes de acoplamiento. De todas formas, es imposible adaptar impedancias imaginarias, y a mayor componente imaginario en una impedancia compleja, mayor será el rango de impedancias que será necesario para implementar el acoplador híbrido transformador.

Se constituye un proceso de diseño optimizando las impedancias de las líneas de transmisión adicionales y alcanzando el resto de valores a partir de las ecuaciones obtenidas del análisis par-impar. Dicho proceso fue usado para diseñar y fabricar acopladores híbridos en tecnología microstrip a 2 GHz con impedancia de referencia de $50\,\Omega$. Uno de los prototipos está adaptado a $450\,\Omega$, que es una impedancia real a la que no se podría haber realizado adaptación sin esta nueva topología debido a los anchos de línea tan pequeños que serían necesarios. Se fabricó otro prototipo con adaptación a $70 - 200j\,\Omega$, obteniendo buena concordancia entre medidas y simulaciones. Se puede obtener una mayor optimización del acoplador híbrido si los puertos correspondientes a la impedancia de referencia no están perfectamente adaptado, y en su lugar están adaptados a una impedancia compleja que produzca baja reflexión. De esta manera se puede reducir la longitud de las líneas de transmisión correspondientes a esos puertos. Se fabricó de nuevo otro prototipo con adaptación a $70 - 200j\,\Omega$, pero en esa ocasión con las mejoras en el tamaño del circuito debido a la adaptación a la impedancia compleja $50 - 20j\,\Omega$ en los puertos correspondientes a la impedancia de referencia, aunque las medidas se referencien igualmente a $50\,\Omega$. Los resultados muestran que no se produce un empeoramiento respecto al acoplador híbrido anterior, alcanzando una mejora en el tamaño del circuito –una reducción del área del 25 %– sin desventajas.

Por tanto, un acoplador híbrido con transformación de impedancia compleja puede ser usado como RTPS cuando la impedancia de adaptación elegida corresponda con el rendimiento de desfase deseado, de acuerdo con el análisis de la carga ajustable. Adaptando un acoplador híbrido a $30 - 57j\,\Omega$, se fabricó un desfasador a 9 GHz con el diodo varactor comercial Aeroflex MGV-125-25-0805-2 y el sustrato Arlon 25N, de permitividad eléctrica $\epsilon_r = 3{,}38$, logrando un rango de desfase de 180,3° con unas pérdidas de inserción de 3.3 a 5.5 dB, y con un tamaño de circuito un 60 % menor del que se habría realizado con un acoplador híbrido normal con redes de adaptación de impedancia en cada puerto para el mismo rendimiento. La agilidad de fase está por encima de 150° en un ancho de banda del 10 %, mientras que la variación de pérdidas de inserción permanece por debajo de 3 dB en un ancho de banda del 20 %.

Se pueden obtener mejores relaciones de compromiso entre agilidad de fase y variación de las pérdidas de inserción si dichas pérdidas fueran igualadas. Las soluciones encontradas en la literatura requieren el uso de inductancias concentradas, cuyos parásitos de empaquetado pueden producir problemas al optimizar el desfasador. La función de las inductancias puede lograrse ajustando debidamente la longitud de las líneas de transmisión en el acoplador híbrido transformador correspondiente a los puertos en los que se colocan las cargas ajustables, asegurando que su longitud eléctrica produzca un cambio en la impedancia del varactor de forma que su parte imaginaria pase por un valor de 0 en algún punto de polarización cercano al punto central. De esta manera, la carga ajustable es vista como una estructura compuesta por la línea de transmisión y el varactor, y así el resto

del acoplador híbrido puede ser estudiado como un acoplador híbrido de adaptación de impedancia real. Por tanto, se obtienen nuevas ecuaciones que relacionan el rendimiento del desfasador con la impedancia de adaptación real del acoplador híbrido y la impedancia transformada de la carga ajustable. Se observa pues, que las pérdidas de inserción pueden ser igualadas colocando una resistencia en paralelo que incrementa la impedancia real de la carga transformada para determinadas tensiones de polarización. Esto es, las pérdidas de inserción aumentan, pero sufren menor variación. Con una resistencia ideal, la variación de pérdidas a 9 GHz se reduce a 0.3 dB manteniendo la agilidad de fase de 180°. Se fabricó un prototipo obteniendo dicho rango de fase, pero con pérdidas de inserción de 4.4 a 5.6 dB (variación de 1.2 dB), con un incremento en la variación debido a los parásitos de empaquetado de la resistencia empleada. El circuito está adaptado con pérdidas de retorno por encima de 10 dB en un ancho de banda del 9,1 %, y presenta variación de pérdidas de inserción por debajo de 1.5 dB junto a una agilidad de fase superior a 150° en un ancho de banda del 9,8 %.

Esta tesis propone un método alternativo para igualar las pérdidas consiste en diseñar acopladores híbridos transformadores de impedancia no equilibrados; esto es, con coeficientes de acoplamiento distintos de 1. En esos casos habrá reflexión por desadaptación, consecuencia de que las cargas ajustables no se corresponden con la impedancia de adaptación y la señal reflejada no se cancela a la entrada. Esta característica aparentemente perjudicial puede utilizarse para igualar las pérdidas de inserción conectando desfasadores en cascada. Mientras que el rango de fase se duplica, la variación de pérdidas de inserción experimenta un aumento menor. Aún así, solo se observó una posible reducción de la variación de pérdidas de 0.5 dB para un rango de fase de 320° si se quisiera mantener una adaptación con pérdidas de retorno superiores a 10 dB. Si no fuera necesario tener buena adaptación, la variación podría haber sido reducida a 1.35 dB, en lugar de la variación de 2.5 dB que se obtendría con acopladores híbridos equilibrados.

En definitiva, se ha realizado una amplia optimización del RTPS para su uso en arrays reconfigurables, controlando su rendimiento con adaptación de impedancia compleja, reduciendo el tamaño del circuito mediante el diseño de un acoplador híbrido que puede adaptar distintas impedancias complejas con diferentes coeficientes de acoplamiento, e igualando las pérdidas de inserción añadiendo resistencias en paralelo o conectando en cascada desfasadores con distintos niveles de acoplamiento. La implementación del método de onda guiada requiere, no obstante, la consideración de otros aspectos.

En un array reflector de onda guiada, el principal requisito es que la onda que se propaga por el espacio libre emitida por la antena alimentadora sea convertida en una onda guiada, y no reflejada directamente por el elemento radiante. La condición de periodicidad de la celda unidad debe ser tenida en cuenta. Se realizó una optimización de los parámetros geométricos de la celda unidad de forma que tanto el modo cuasi-TEM de la línea microstrip como la combinación de modos de Floquet que se correspondan con el modo co-polar estén optimizados y transfiriéndose con bajas pérdidas de inserción. La definición de los modos de Floquet depende del ángulo de incidencia –el ángulo formado entre el vector de propagación de la onda emitida por la antena alimentadora y la posición del

elemento del array, en $\theta$ y $\varphi$– pero pueden estar siempre expresados en modos polarizados en $x$ e $y$, lo cual facilita el análisis. Se optimizó una celda unidad a incidencia normal, y posteriormente la longitud de los stubs de cada celda fue optimizado individualmente para realizar conformado de haz en broadside y a 45° en acimut mediante un array reflector fijo de $4 \times 4$ elementos. Se fabricó un prototipo que, mediante la sustitución de la capa correspondiente a los stubs, radia dos haces distintos. Hay buena concordancia entre medidas y simulaciones, incluso cuando se compara con el diagrama de radiación esperado de un array con síntesis de fase ideal, probando que el análisis de la celda unidad fue realizado correctamente.

Puesto que la onda guiada en el array reflector tiene que ser llevada de vuelta al elemento radiante, el desfasador tiene que ser usado como red de un solo puerto, en la que la entrada es también la salida. Esto es, que gracias a que uno de los puertos es dejado en circuito abierto, la señal se refleja de vuelta al puerto de entrada desfasada y con pérdidas de inserción. Sin embargo, el análisis realizado anteriormente suponía el uso del desfasador como red de dos puertos. La restricción de adaptación anterior que afectaba al desfasador cuando el acoplador no estaba equilibrado puede ser ignorada, ya que la señal se reflejará en cualquier caso. Por tanto, se puede efectuar una mayor optimización del rendimiento, logrando la agilidad de fase de dos desfasadores en cascada con variaciones de pérdidas de inserción por debajo de 1 dB con un solo desfasador, demostrando ser una topología más eficiente. Además, se puede colocar una sola resistencia en el puerto de entrada/salida para igualar las pérdidas de inserción. Aunque esto no produzca menores variaciones de pérdidas, sí mejora el rango de acopladores híbridos transformadores que se pueden utilizar para obtener una determinada agilidad de fase junto a bajas pérdidas de inserción, que a su vez resulta en optimizaciones más rápidas y más grados de libertad en el diseño. Se fabricó un desfasador a 9 GHz en el sustrato Arlon 25N, obteniendo un rango de fase de 320° con pérdidas de inserción de 3.4 a 5.2 dB, que se reduce a una variación de 1 dB si se coloca una resistencia paralela. La agilidad de fase es superior de 300° y la variación de pérdidas inferior a 4 dB en un ancho de banda del 12,33 %, que es mayor que el del típico array reflector. El tamaño de circuito es lo suficientemente pequeño como para utilizar una separación entre elementos de $0{,}7\lambda$, que podría haber sido reducido aún más si se hubiera empleado un sustrato con mayor permitividad eléctrica.

Esta topología es, por otro lado, sensible a cambios en la impedancia del puerto. Unos pequeños cambios en la impedancia que podrían considerarse que mantienen una buena adaptación desembocan en grandes variaciones de fase (por encima de 100°) y de pérdidas de inserción. Ya que la celda unidad fue optimizada solo al ángulo de incidencia normal, resulta preocupante que la adaptación se vea comprometida a otros ángulos de incidencia, produciendo comportamientos del desfasador distintos para cada elemento del array. Se realizó una nueva optimización de la celda unidad para asegurar adaptación excelente a cada ángulo de incidencia del reflector $4 \times 4$ previamente diseñado. Si no se hubiera podido alcanzar buena adaptación para todos los ángulos, se podrían haber empleado diferentes celdas unidades, dividiendo el array en sub-arrays. El reflector fijo no presentó este problema puesto que cada celda fue ajustada individualmente para obtener el

desfase requerido a cada ángulo de incidencia, lo cual no es posible al utilizar el desfasador continuo, ya que su diseño es único. Con la celda nuevamente optimizada, se realizaron simulaciones utilizando las medidas del desfasador, logrando una diferencia de desfase entre celdas menor de 30°, y una variación de pérdidas inferior a 2.5 dB.

Se fabricó y medió en una cámara anecoica un array reflector reconfigurable de $4 \times 4$ elementos con lineas de polarización separadas para cada elemento. Cada línea de polarización es controlada por la placa de evaluación de un convertidor digital a analógico, que a su vez es dirigida por un microcontrolador Arduino. Se aplicaron tensiones para realizar escaneo de haz en acimut y elevación, logrando barrido de haz de $-10°$ a $30°$ en acimut y de $-20°$ a $20°$ en elevación. El rango de escaneo está limitado por el pequeño tamaño del reflector, dado que la ganancia disminuye a medida que el haz principal se aleja del ángulo de reflexión especular. Aun así, la reconfigurabilidad está suficientemente demostrada. La topología de RTPS de un solo puerto tiene un rendimiento excelente y remarca lo importante que es tener en cuenta los distintos ángulos de referencia al diseñar el array reflector.

Las lentes de array requieren de dos superficies radiantes opuestas, que una estructura tipo guía de onda tiene que comunicar realizando corrección de fase. La tecnología microstrip necesitaría antenas de parche adicionales –que incrementarían la separación entre elementos ya que el tamaño de circuito tendría que aumentar para dejar espacio a un parche en la misma capa que el desfasador– o un cambio del plano de referencia de 90°, que aumenta el grosor de la lente, produce pérdidas de inserción, incrementa la complejidad de fabricación y resulta en una estructura más frágil. En su lugar, se propone el uso de guía de onda integrada en sustrato (*Substrate Integrated Waveguide*, SIW). El acoplamiento de la SIW a la antena de parche puede realizarse cortocircuitando un extremo de la SIW con agujeros metalizados, y grabando una ranura longitudinal o transversal, dependiendo de la dirección de polarización deseada. Se observó que colocando la ranura transversal justo al lado del cortocircuito no presenta efectos adversos, radiando como una antena de parche típica, y optimizando el tamaño del circuito reduciendo el espacio longitudinal. Como las ranuras y las antenas de parche pueden colocarse en cualquier lado (correspondiente a las láminas de conductor eléctrico) de la SIW indistintamente, sería posible recibir la onda emitida por la antena alimentadora en un lado, acoplarla a la SIW y transmitirla a través de la antena de parche ubicada en el extremo opuesto tras realizar la corrección de fase.

Una traslación directa de tecnología microstrip a SIW del desfasador no es aconsejable. Los acopladores híbridos SIW necesitan mucho espacio debido a la necesidad de incorporar distintas guías de onda, que son más anchas que la típica línea microstrip. Además, no hay un método equivalente de control del rendimiento de la carga ajustable que esté al mismo nivel. Se propone una nueva estructura en su lugar, aprovechando las características únicas de la tecnología SIW. Colocando dos ranuras inclinadas de determinada longitud, anchura y separación, con condensadores interdigitados para conseguir más control de su impedancia, el acoplador híbrido es reemplazado por una estructura mucho más pequeña. Las cargas ajustables se colocan en el centro de las ranuras inclinadas, y la estructura al completo actúa como un desfasador basado en reflexión: el modo $TE_{10}$ se divide en un modo

cuasi-$TE_{20}$ en el que los campos electromagnéticos están desfasados 90°. Cuando el valor de los parámetros geométricos está asignado correctamente, el análisis de los parámetros de dispersión (parámetros-S) con puertos concentrados colocados en el lugar en el que irían las cargas ajustables, resulta en una matriz de parámetros-S equivalente a la de un acoplador híbrido transformador de impedancia. Por tanto, cuando se carga con las impedancias ajustables se comporta de la misma manera que el RTPS: los campos reflejados por las ranuras de vuelta al puerto de entrada se cancelan al tener una diferencia de fase de 180°, y los campos reflejados adelante son sumados al estar en fase, recomponiendo el modo $TE_{10}$ con un desfase y pérdidas de inserción dependientes de la carga ajustable y la impedancia de adaptación en las ranuras.

Debido a la novedad de la estructura, se desarrolló primero un prototipo usando condensadores fijos. Se obtuvieron distintos desfases soldando condensadores de distintas capacidades en las ranuras, con el prototipo mostrando concordancia entre medidas y simulaciones. Se diseñó y fabricó otro prototipo usando como carga ajustable el varactor Aeroflex MGV-125-25-0805-2. Para aislar la tensión de polarización continua, se grabaron ranuras adicionales, dejando una superficie aislada entre las ranuras inclinadas. Estas ranuras adicionales se cubren con condensadores de bloqueo de corriente continua, para no afectar al rendimiento del desfasador. Se suelda un cable a la superficie aislada para aplicar la tensión de polarización, que puede servir también como red de polarización al tener alta impedancia a la frecuencia de trabajo, evitando posibles interferencias. El prototipo, realizado en el sustrato Arlon 25N, proporciona a 9 GHz una agilidad de fase de 180°, con pérdidas de inserción de 4.15 a 7.15 dB (variación de 3 dB). Presenta una media de pérdidas de retorno por encima de 10 dB, con una agilidad de fase de 150° y variación de pérdidas de inserción por debajo de 5 dB para un ancho de banda del 7 %. La variación de pérdidas es mayor y el ancho de banda menor a lo esperado por las simulaciones, y ligeramente peor comparado con los RTPS anteriores en tecnología microstrip. Se atribuye a la falta de exactitud en el soldado manual de los varactores, puesto que requiere precisión para soldar los componentes en el centro de las ranuras, y el pequeño espacio existente entre las ranuras lo hace más difícil. En cualquier caso, el desfasador mide de largo solo 5.73 mm, que equivale una longitud de 0.116 veces la longitud de onda en la guía. Un desfasador SIW compuesto por un acoplador híbrido habría requerido al menos una longitud de 1.2 veces dicha longitud de onda, además de incrementar la anchura debido a la incorporación de otra SIW paralela. A pesar de las pequeñas deficiencias en pérdidas de inserción, la reducción del tamaño, especialmente comparada con las alternativas, resulta destacable. Aunque no se haya obtenido un rango de control de fase completo de 360°, resulta fácil conectar en cascada otra instancia del desfasador gracias a su pequeña longitud, siendo posible colocarlo en la otra capa de conductor eléctrico si así fuera deseado. No obstante, la proximidad a un parche radiante debe ser considerada. Si las ranuras inclinadas están demasiado próximas a dicho parche, el rendimiento del desfasador se resentiría, especialmente en lo concerniente a pérdidas de inserción. Se observó que una distancia de 3 mm es suficiente para lograr un rendimiento cercano al óptimo. También es importante considerar que el desfasador no se ve afectado por el parche en ningún caso si está localizado en la

lámina opuesta.

La adaptación de la onda guiada en la lente de array puede ser simulada de la misma manera que en el reflector, usando el análisis de modos de Floquet en HFSS, con el único cambio consistente en adaptar el modo co-polar al modo $TE_{10}$ de la SIW en lugar de al modo cuasi-TEM de la línea microstrip. Además, la celda unidad de la lente de array se muestra menos afectada por la desadaptación resultante de distintos ángulos de incidencia. Incluso una celda unidad optimizada solo para incidencia normal sufre poca variación de desfase y pérdidas de inserción a distintos ángulos de incidencia. Unido al hecho de que la antena alimentadora en la lente de array se encuentra centrada en prácticamente todos los casos, y por tanto el rango de ángulos de incidencia se mantiene al mínimo, es más fácil optimizar el método de onda guiada para una lente que para un reflector. La principal restricción de la celda unidad es la separación que debe ser mantenida entre las ranuras del desfasador y los parches radiantes. Sin embargo, esta condición también favorece el uso de dos desfasadores conectados en cascada en láminas conductoras opuestas sin afectar a la separación entre elementos.

El mayor problema al simular la lente de array basada en tecnología SIW en HFSS es la potencia de computación requerida. Simular un desfasador SIW ya requiere mucho tiempo de procesamiento debido al mallado de los agujeros metalizados y las ranuras inclinadas, y se ve agravado cuando la estructura se repite periódicamente, resultando también en una simulación menos precisa. Por tanto, se simuló una lente de array de tan solo $2 \times 2$ elementos, con un plano de masa infinito para bloquear completamente la onda de la antena alimentadora y así eliminarla del diagrama de radiación resultante. Se obtuvo un barrido de haz de $-10°$ a $10°$ tanto en acimut como en elevación. Debido a las dificultades de fabricación, se construyó un pequeño prototipo de $2 \times 2$ elementos. Puesto que hay poca eficiencia de desbordamiento, el campo radiado por la antena alimentadora contamina las medidas, por lo que el barrido de haz no puede realizarse. No obstante, se observó que aplicando las tensiones correspondientes a un haz que apunte a $\theta = -45°$, el haz medido puede ser corregido para apuntar a broadside, mostrando reconfigurabilidad. Aunque los resultados obtenidos de la antena SIW y del desfasador SIW son satisfactorios, la reconfigurabilidad de la lente no está lo suficientemente validada experimentalmente, y es necesario realizar más tareas a tal efecto. Aun así, el trabajo presentado es significativo al constituir la primera propuesta de una lente de array en tecnología SIW.

# Abstract

Reconfigurable antennas, capable of conforming different radiation patterns, are used on many radio frequency applications. From among these antennas, reconfigurable reflectarrays and array lenses are interesting due to the lack of distribution networks, which save costs and manufacturing complexity. Furthermore, the guided-wave approach to those arrays allows to perform a modular design: the radiating elements and the phase shifter are optimized independently. For the best reconfigurability capabilities, the phase shifter should be continuous, offering full phase control range, low insertion losses and loss variation, while keeping a small circuit footprint for reducing the array element spacing.

Reflection-type phase shifters (RTPS) using varactors as tunable loads offer good characteristics but need improvements, as traditional implementations are costly, incur in increase of circuit size or require lumped components whose parasitics deteriorate performance. To overcome that, this thesis introduces the complex impedance transforming hybrid coupler, capable of fulfilling the role of a hybrid coupler of arbitrary coupling coefficient while matching two different complex impedances in each pair of isolated ports. The choice of the matching impedance defines the performance of the phase shifter, allowing to select trade-offs between phase control range and insertion losses, while maintaining a compact circuit footprint. This structure is employed to manufacture a phase shifter prototype at 9 GHz, obtaining a phase agility of 180° that triples that of the basic topology with the same varactor while keeping insertion loss variation below 2.2 dB. A further reduction of the insertion loss ripple to 1.2 dB is achieved employing parallel resistors, which would have been further reduced to 0.3 dB if not for their packaging parasitics.

A reflectarray cell is typically designed at normal incidence, but it was shown that the matching deteriorates as the incidence angle of the impinging plane wave increases, potentially affecting the phase shifter performance. It is, then, necessary to take the incidence angles into account to achieve proper matching for each element of the array. It was also observed that employing the RTPS as a one port network fits a reflectarray better, and achieves additional improvements in phase agility and insertion loss, surpassing those of cascaded phase shifters. A prototype was manufactured and measured at 9 GHz obtaining a 320° phase control range with an insertion loss from 3.4 to 5.2 dB, whose variation can be further reduced to 1 dB by a single parallel resistors without affecting the phase agility. With this means, a $4 \times 4$ elements reconfigurable reflectarray was fabricated, obtaining beam steering from $-10°$ to 30° in azimuth and from $-20°$ to 20° in elevation.

In the array lens, communicating the input and output layers in the guided-wave

approach requires extra layers, more complex structures or increased element spacing. This thesis proposes instead to link them through a substrate integrated waveguide (SIW), making it the first array lens based on that technology. A novel SIW phase shifter is also posited, based on loaded tilted slots that replaces the SIW reflection-type phase shifters found in the literature, obtaining equivalent performance within a fraction of its size (with a potential reduction of 90% in length, and 50% in width). The measured prototype bestows at 9 GHz 180° phase agility with insertion losses from 4.2 to 7.1 dB. The phase shifter is simulated in conjunction with the proposed array lens, realizing beam steering. A $2 \times 2$ elements array lens prototype was manufactured as proof of concept, achieving a small beam correction in broadside.

# Contents

**Title page** ..... **i**

**Acknowledgments** ..... **iii**

**Resumen** ..... **v**

**Conclusiones** ..... **ix**

**Abstract** ..... **xvii**

**Contents** ..... **xix**

**1 Introduction** ..... **1**
1.1 Motivation ..... 1
1.2 Background ..... 2
1.2.1 Reflectarrays ..... 2
1.2.1.1 Tunable scatterer approach ..... 3
1.2.1.2 Guided-wave approach ..... 4
1.2.2 Array lenses ..... 5
1.2.2.1 Tunable scatterer approach ..... 6
1.2.2.2 Guided-wave approach ..... 6
1.2.3 Phase shifters ..... 6
1.3 Thesis goals ..... 9
1.4 Thesis outline ..... 9

**2 Analysis and optimization of coupler based phase shifters** ..... **11**
2.1 Introduction ..... 11
2.2 Reflection-type phase shifter with impedance matching ..... 12
2.2.1 Original topology ..... 12
2.2.2 Addition of impedance matching networks ..... 13
2.2.3 Parametric analysis ..... 15
2.3 Complex impedance transforming hybrid coupler ..... 17
2.3.1 Analysis ..... 17
2.3.2 Design procedure ..... 20
2.3.3 Impedance matching limitations ..... 21

2.3.3.1 Real impedances . . . 22
2.3.3.2 Imaginary impedances . . . 22
2.3.3.3 Complex impedances . . . 23
2.3.4 Measurements . . . 23
2.3.4.1 Complex impedance transformer . . . 24
2.3.4.2 Real impedance transformer . . . 25
2.3.4.3 Reduced complex impedance transformer . . . 27
2.4 RTPS with complex impedance transforming hybrid couplers . . . 28
2.4.1 Effects of the matching on a phase shifter . . . 28
2.4.2 Methods for equalizing the insertion loss . . . 33
2.4.2.1 Lossy structure . . . 33
2.4.2.2 Cascading phase shifters . . . 39
2.5 Conclusions . . . 42

**3 Tunable reflectarray . . . 45**
3.1 Introduction . . . 45
3.2 Fixed guided wave approach . . . 46
3.2.1 Structure . . . 46
3.2.2 Unit cell matching . . . 46
3.2.2.1 Periodicity simulation . . . 46
3.2.2.2 Incidence angles . . . 49
3.2.3 Phase shift for beam steering . . . 52
3.2.4 Measurements . . . 53
3.3 Phase shifter element . . . 56
3.3.1 One-port RTPS . . . 57
3.3.2 Equalizing resistance . . . 58
3.3.3 Measurements . . . 59
3.4 Tunable reflectarray cell . . . 62
3.4.1 Reflecting RTPS evaluation . . . 62
3.4.2 Tunable reflectarray measurements . . . 65
3.5 Conclusions . . . 66

**4 Tunable array lens . . . 71**
4.1 Introduction . . . 71
4.2 Substrate integrated waveguide . . . 73
4.2.1 Operation principle . . . 73
4.2.2 Coupling to patch antennas . . . 74
4.2.2.1 Longitudinal slot . . . 74
4.2.2.2 Transverse slot . . . 75
4.2.3 Hybrid couplers and RTPS . . . 76
4.3 Phase shifter element . . . 77
4.3.1 Impedance transforming hybrid coupler equivalence . . . 77
4.3.2 Loaded tilted slots design . . . 78

4.3.3 Measurements . . . 80
4.3.3.1 Fixed capacitors design . . . 80
4.3.3.2 Varactor-tuned design . . . 82
4.4 Tunable array lens cell . . . 85
4.4.1 Fixed cell analysis . . . 85
4.4.2 Phase shifter integration . . . 87
4.4.3 Unit cell design . . . 89
4.4.4 Prototype . . . 90
4.5 Conclusions . . . 92

**5 Conclusions and future research lines . . . 97**
5.1 Final conclusions . . . 97
5.2 Future lines of work . . . 103
5.3 List of publications related to this work . . . 104
5.3.1 International journals . . . 104
5.3.2 International conferences . . . 105
5.4 Other publications . . . 105
5.5 Projects related to this work . . . 105

**References . . . 107**

CHAPTER 1

# Introduction

## 1.1. Motivation

Reconfigurable antennas are devices capable of conforming different radiation patterns, be it by switching between several fixed configurations or by performing adaptive beamforming. Their use is of importance in many wireless and sensing applications including mobile communications, satellite communications, radars and terrestrial links. Traditional aperture antennas, such as reflectors and lenses, can be used to that effect, but require mechanical mobility for beam scanning, and beamshaping is out of the question unless sophisticated feeding systems are employed. Contrastingly, phased array antennas permit electrical tunability by feeding each element of an antenna array with a different phase, performing real time beam scanning. However, their implementation is difficult as they require complex distribution networks, or dedicated transceiver modules for each array element resulting in high manufacturing costs. On the other hand, reflectarrays and array lenses are a combination between aperture antennas and antenna arrays, offering the high-gain of aperture antennas with ease of manufacture, low cost and weight, as the arrays consists of printed antennas. Furthermore, the phase synthesis can be performed on each element of the array directly, thus avoiding the complexity of typical phased arrays.

A reflectarray consists of a feeding antenna (typically a horn antenna) and an array of radiating elements. The feed produces a spatial electromagnetic wave that impinges onto the array, with a different path to each radiating element. Then, each element reflects the wave producing a different phase correction. The sum of the reflected waves results in a new radiation pattern. The feeding antenna is usually offset from the center of the array to avoid blocking the reflected radiation pattern.

In an array lens the working principle is similar. The feeding antenna radiates an electromagnetic wave onto an array of printed antennas. However, instead of reflecting back the corrected wave, it is coupled to another layer of radiating elements, which in turn radiate the phase corrected wave onto the opposite side, resulting in a transmitted wave. This way, the feeding antenna cannot block the radiation pattern of the array, and it can be used not only in far-field beamshaping, but also to obtain focal points in the vicinity

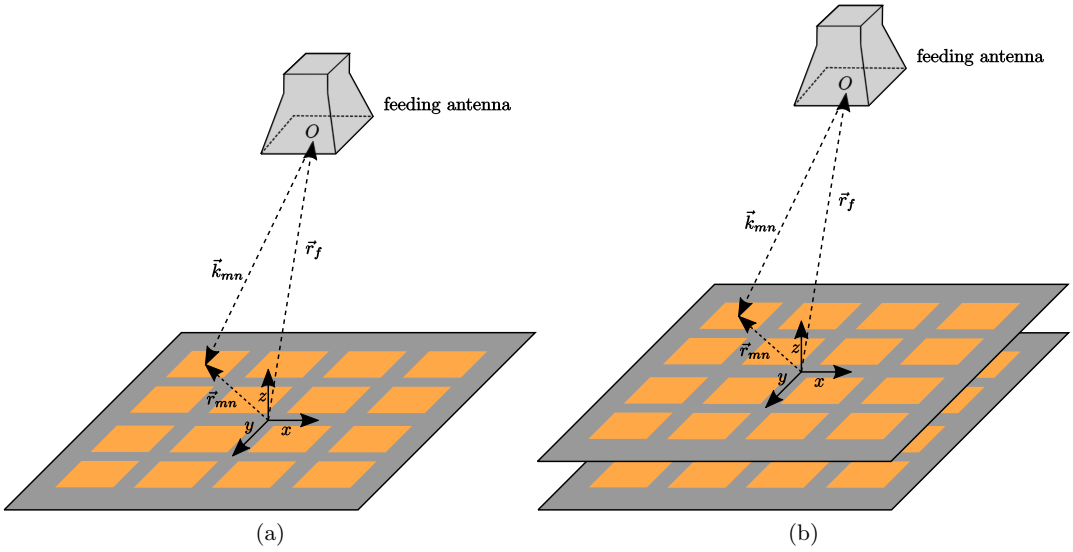


Figure 1.1: (a) Representation of a reflectarray antenna. (b) Representation of an array lens antenna.

of the lens aperture.

In both reflectarrays and array lenses, the beamshaping can be made reconfigurable by adding tunable elements to the arrays. This away, the complex distribution networks of phased arrays are replaced by the antenna feeding the array, enabling the manufacture of low-cost, low-profile reconfigurable antennas which do not require mechanical mobility. This thesis consists in the analysis and optimization of low-cost reconfigurable reflectarray and array lens antennas, offering an insight into the design process, analyzing the major constraints and bestowing new solutions focused on achieving the maximum radiation pattern reconfigurability at a single operating frequency.

## 1.2. Background

This section provides background on reconfigurable reflectarray, array lens antennas and phase shifters. There are many aspects to consider when reviewing the research on those technologies, but only those directly concerning the thesis topic will be considered: beamshaping, reconfiguration techniques and types of phase shifters.

### 1.2.1. Reflectarrays

The reflectarray antennas were first introduced in the 1960s [1], and consisted in a waveguide array terminated in shortcircuit of variable length that re-radiated an incident field. With distinct waveguide lengths, different phase shifts were obtained. By choosing the appropriate phase shifts, beam steering was possible. However, that prototype was bulky and not practical. It was not until the 1990s that the popularization of planar technology such as microstrip would produce a resurgence of the reflectarray [2], achieving low-profile and low-cost antennas, specially when compared to parabolic reflectors.

The reflectarrays can be classified into two types: fixed and reconfigurable. The fixed reflectarrays are the most well-known, they offer great versatility regarding static beamforming and bandwidths superior to 20% [3]. On the other hand, reconfigurable reflectarrays offer the capability of realizing adaptive beamforming and even amplifying the reflected signal. In order to do that, active elements are used that change in real time the phase shift of the different elements of the array.

The reconfigurable reflectarrays can be further classified depending on the nature of the tunable elements they use: discrete or continuous. The discrete reflectarrays use MEMS capacitors or PIN diodes, while the continuous employ varactor diodes, liquid crystals, ferroelectric materials and graphene. However, a more interesting classification can be made regarding how the phase correction of each element is realized: either directly by the resonant of the radiating element (tunable scatterer approach) or by coupling the impinging wave to a waveguide-like structure where the phase shift is realized and then coupled back to the radiating element (guided-wave approach) [4].

#### 1.2.1.1. Tunable scatterer approach

The phase of the reflected wave may be modified by changing the resonant frequency of the radiating element, which can be thought of as changing its electrical length. In [5], a PIN diode is used to activate or deactivate an transmission line that would lengthen the microstrip patch. This solution offers a 1-bit reconfiguration, and so a large a number of elements is needed to increase the reconfigurability. The polarization circuit introduces a resonance that produces disagreement between simulations and measurements. Following the same concept, a $160 \times 160$ reflectarray was manufactured at 60 GHz [6]. Again, due to a polarization resonance, the reflectarray did not behave as expected. One of the major disadvantages of such a big reflectarray is the number of control signals necessary. In order to avoid having a different control line for each diode, a FPGA was used for controlling 160 lines corresponding to diode columns, and other 160 lines corresponding to diode lines, and thus the diodes are properly biased by performing a column and line sweep that takes $10\,\mu s$. Other configuration with PIN diodes can perform a polarization change, as with a unit cell composed of a rectangular patch in one side and three slots loaded with two PIN diodes on the other [7]. Depending on how the slots are placed, the polarization of the reflected wave will be orthogonal or perpendicular to the polarization of the incident wave. It is also possible to use the PIN diodes with a circular polarization feed in a spiraphase configuration [8], consisting of a slot ring resonator and 8 radial stubs, with 8 diodes connected in parallel. When one diode is activated, the rest are deactivated and a resonant circuit is formed, simulating a mechanical rotation of 8 different angles. However, no actual reflectarray was manufactured, as introducing the bias circuitry without incurring in insertion loss is still a challenge. Nevertheless, the tendency in recent years has promoted the displacement of PIN diodes in favor of MEMS capacitors, due to lower consumption, high linearity, low insertion loss and high isolation.

Many of the reflectarray designs using the tunable scatterer method require costly and long simulations, making it difficult to perform optimizations. In [9], a patch loaded

with various MEMS is presented, and an equivalent circuit model is obtained to optimize the cell. Using a full-wave commercial simulator would have made the simulation times intolerable. Nevertheless, the effect of polarization lines remain unaccounted for. In [10] another unit cell consisting on slots loaded with MEMS is proposed, and again a custom simulation method is developed for faster computation times. It is even possible to switch polarizations, at the expense of a 1-bit cell resolution [11]. The use of tertiary MEMS (capacitors with tree states) is also considered for reducing the number of control lines without decreasing the reconfigurability [12], although no reflectarray implementation exists as of yet.

Varactors may also be employed, achieving continuous reconfiguration. In [13], a cell is proposed composed of a patch and a varactor embedded in the substrate, connected both to the patch and to the ground plane. The position of the varactor and the length of the patch are the only variables that can affect the possible phase shift range. In [14], a reflectarray cell is realized by employing two resonant square rings connected by six different varactors. While it requires more varactors than any other structure, the phase agility is over 360° at 5.4 GHz. However, the insertion loss was increased due to not utilising a correct varactor model at the working frequency. The structure in [15] requires only one varactor, which is embedded in a resonant cavity, whose capacity it modifies. Nevertheless, only a beam scanning range of 36° in elevation was obtained despite manufacturing a $6 \times 6$ reflectarray.

The resonant frequency can also be changed by varying the dielectric constant of the substrate. For instance, liquid crystals are able to realize reconfigurable reflectarray at submillimetre bands, thanks to the better radiofrequency behaviour at those frequencies. The liquid crystals are used as substrate, and applying voltage changes the orientation of the crystals, producing different dielectric constants, although taking some time to do so [16]. However, they introduce new complications as a reflectarray based on liquid crystals must be manufactured in differentiated steps: a cavity must be left which will later be filled with the liquid crystals [17]. The cavity is very small, around $100\,\mu m$ and must be stable for all the reflectarray or the unit cell analysis would not be useful. Furthermore, it must be properly sealed to avoid leakage. In [18], a $16 \times 16$ reflectarray is manufactured based on liquid crystals working at 77 GHz with considerable insertion loss, achieving a 280° phase agility. An improvement is presented in [19] by connecting three dipoles through a narrow perpendicular microstrip line, obtaining a 500° phase shift range. In [20], a unit cell is proposed for use in X-band. As an alternative to liquid crystals, ferroelectric materials [21, 22] and fluidic networks [23] might be employed. The first technology has not yet matured and produces high insertion loss, and the second requires the control of liquid flow, resulting in slow reconfigurability.

#### 1.2.1.2. Guided-wave approach

Instead of modifying the resonant frequency of the radiating element, it is possible to couple the incident wave to a waveguide-like structure, where the phase shift is produced and then re-radiated back. This technique was first used in fixed antennas, and was later expanded by incorporating reconfigurable phase shifters. In this approach, the unit cells

are easier to optimize, as the radiating elements and phase shifters can be optimized separately, permitting a modular design procedure. PIN diodes, MEMS capacitors and varactor diodes are the preferred reconfigurable elements for this approach.

The line selection with PIN diodes can be employed as well in the guided-wave approach. Instead of changing the resonant length of the scatterer, a slot in the ground plane couples the incident wave onto a stub, whose length can be changed via the PIN diode interconnecting it, and may be shared by two array elements for reducing complexity [24]. In this approach, it is also possible to reduce complexity by arranging the cells into subarrays without reducing the performance of the antenna [25]. MEMs can be used in the same way [26], but the structure requires a large number of elements due to the cell only having a 1-bit reconfiguration. A monolithic reflectarray at 26 GHz was fabricated in [27]. The insertion losses in both cases are bigger than what is possible with MEMs in the tunable scatterer approach. It is attributed to all the power of the incident wave going through the waveguide-like structure where the MEMs are situated, whereas in the previous case they were only subject to low induced currents [4].

The most notable tunable reflectarrays in guided-wave approach are based on varactors, since they are not limited by cell resolution. In [28], a patch antenna is coupled to a 3 dB stripline coupler loaded reactively with a varactor and a shortcircuited stub. A 360° phase agility is achieved at 2 GHz, although drastically decreases at higher frequencies. A change in polarization from the incident to reflected wave can be produced if the slot through which the phase corrected wave is re-radiated is perpendicular to the slot through which it was coupled at first. Following this concept, a transmission phase shifter based on four varactors and an amplifier was designed [29], acomplishing a 360° phase shift range with insertion losses up to 6 dB. A $8 \times 6$ reflectarray was manufactured obtaining a 11.3 dB gain. A varactor embedded in substrate as in [15] is used in a guided-wave approach in [30], where the embedded varactor acts as a reflective load at the end of a transmission line. However, it is not as well suited as the only way to control the phase shifting performance is by changing the transmission line length, and a 320° phase shift range is correlated with an increase in insertion loss of 6 dB.

While this approach eases the design of the radiating element, it requires to put more attention into the phase shifter, as it is the piece that will determine the overall reconfiguration capability of the antenna. It is necessary, then, to carefully evaluate what phase shifter topology would be the best to implement.

### 1.2.2. Array lenses

Array lenses, or transmitarrays, were originally realized by controlling the delay of an electromagnetic wave through a discrete structure [31]. They did not gather much traction until planar technologies became available, using microstrip elements to couple waves to delay lines connecting the input and output radiating elements. At first, transmission lines of different lengths were used for beamshaping [32], but any two port networks integrable between two radiating elements would work (as in a guided-wave approach). Nevertheless, two layers of resonant scatterers that couple the incident wave producing

the required phase shift can also be employed [33]. Introducing tunable elements to the two port networks or to the resonant scatterers result in reconfigurable array lenses. Thus, they can be classified in the same way as the reconfigurable reflectarrays.

#### 1.2.2.1. Tunable scatterer approach

In a reflectarray, the incident wave has to be reflected, which is guaranteed with the presence of a ground plane. Furthermore, the scatterer interacts twice with the incident wave, meaning that a single-pole resonator can easily produce a 360° phase shift. In the array lens the wave is not reflected and the resonators introduce a single pole response, reducing the phase agility [4]. Therefore, different resonators must be employed for multi-pole responses that would increase the phase shift range [34], as single-pole array lenses achieve low phase agilities [35]. In [36], a multilayer structure is used in which the patches on both input and output sides are loaded with varactors, and an extra resonance is added thorugh a varactor-loaded slot in another layer, but still not achieving a full phase control range. Increasing the distance between resonators can achieve a better phase range, but it produces spurious radiation, besides increasing the thickness of the lens [37]. Hence, it is difficult to obtain good reconfigurability in array lenses with tunable scatterers.

#### 1.2.2.2. Guided-wave approach

In this approach, the reconfigurability is left to the waveguide-like element connecting the input and output layers. Although it would seem that this should facilitate the design, and a 360° phase shifter could be easily incorporated, there are only a small number of examples of this technique. To facilitate the integration of the phase shifter, a 3D structure can be employed, though it increases the thickness and manufacturing cost [38]. Other designs employ a multi-layer structure by stacking radiating elements to facilitate the coupling to the waveguide-like structure using varactor diodes [37, 39] or MEMS capacitors [40]. An optimal guided-wave design should facilitate the coupling between the input, the phase shifter and output layers without adding extra manufacturing complexity and extra layers.

### 1.2.3. Phase shifters

It has been established that the adjustable phase shifter is the most important element in the guided-wave approach. Hence, it is important to review the types of phase shifters available, and focus on the topology that offers the best characteristics.

Generally speaking, a phase shifter is a device that allows to change the state of a signal through a phase variation. They can be classified into discrete and continuous. The discrete phase shifters have a finite number of states, while the continuous phase shifters are able to provide a virtually unlimited number of states. Nevertheless, they are more difficult to characterize, requiring more complex control signals due to the use of analog voltages.

The key parameters to consider in a continuous phase shifter are: [41]

- Phase control range: also called phase agility, the space of possible phase shifts bestowed by the phase shifter. A full phase control would necessitate a 360° range. More range is still welcome, as it can offer more flexibility when employing the phase shifter, and it can even correct quantification errors.

- Phase resolution: with an analog control, any phase could theoretically be obtained. A linear response of phase versus voltage would be favorable for minimizing the required resolution in digital to analog converters.

- Insertion loss: passive structures produce losses, which should be kept to a minimum. Active structures can bestow gain and thus avoid insertion loss, but they require power consumption.

- Insertion loss variation: the insertion losses may present a big variation or ripple depending on the polarization voltage, and should be avoided in phased arrays for not deteriorating the radiation pattern.

- Bandwidth: operating frequencies of the phase shifter. A larger bandwidth allows the phase shifter to be used in more applications.

- Group delay: it can produce distortion in wide bandwidth signals if the group delay is not constant at the operating frequencies.

- Power management capacity: the employment of phase shifters in large signals is limited to the 1 dB compression point.

- Power consumption: the use of active elements implies power consumption. It should be a capital aspect to consider in battery-powered antennas.

- Circuit footprint: the smaller the circuit size, the easier it is to integrate, facilitating small element spacing in phased arrays.

- Noise: active devices introduce noise. This should be considered in some applications, such as phased array receptors in which the phase shifters are directly connected to the antennas.

- System stability: for a phase shifter to function properly, it must remain stable. To analyze stability one must consider every possible state. This analysis is of the utmost importance when the phase shifters have a feedback loop, such as one produced by coupling.

Due to this numerous limitations, some trade-offs must be established. The most determinant requirements for phased array implementation must be prioritized. Those would be the phase control range, insertion loss and its variation, circuit footprint and finally, bandwidth.

The most commong topologies among phase shifters are: [41]

- Vector modulators: they divide the signal in several branches, in a way such as every branch has a different phase shift, with an amplitude changing through a variable amplifier or attenuator. For achieving a full phase control range of 360°, four paths are needed, with a relative offset of 90°. In any given moment, only two paths are chosen, and their gain or attenuation is modified for achieving the desired phase shift. The implementation of variable gain amplifiers required considerable power consumption and circuit footprint. On the other hand, while variable attenuators do not require power, they produce big insertion loss. This phase shifters require 4 control signals, 2 for the amplifiers and other 2 for the commuters.

- Switched-based phase shifters: they are based on the choice of different phase paths. They are typically realized through delay lines or filter, between which they commute. It is, then a discrete phase shifter with limited reconfigurability. Furthermore, its circuit footprint gets big if many elements are introduced for obtaining a high phase resolution.

- Distributed phase shifters: the phase can be modified through fixed transmission lines loaded with a tunable reactive load, obtaining a bandwidth relatively wide. However, with just one loaded transmission line it is not possible to obtain a 360° phase range, and it is necessary to cascade more lines, increasing the circuit size.

- Reflection-type phase shifter: There are two ways of implementing this type of phase shifters: either with circulators or with couplers. Both are based on the same principle, the input signal is reflected by a tunable reactive load which modifies its phase, and the signal gets through in a different port. Nevertheless, the circulator topology requires amplifiers for obtaining an acceptable phase range, also producing high noise levels. On the other hand, the reflection-type phase shifters based on couplers can do the same thing by adding passive elements to the reactive load, maintaining zero power consumption and low noise level. Only one control signal is needed for biasing the loads.

For low consumption power, acceptable phase control range and low size, the reflection-type phase shifter with couplers offer the best characteristics. Thus, that topology should be more extensively studied.

Traditionally, varactores are used as reactive loads [42]. However, the use of just a bare varactor as reactive load does not bestow a good phase control range. One typical solution comprises adding several parallel varactors [43], [44]. In [45], a monolithic phase shifter was designed using MESFET transistors as varactors, putting them in parallel and introducing an extra resonance through a resonant LC circuit, obtaining a 360° phase agility at 5.6 GHz, but with high losses, from 3.4 to 9.4, resulting in a very big ripple. Following the same principle, another monolithic phase shifter with CMOS transistors is manufactured in [46], with the transistors also acting as amplifiers. A very variable gain from 7 to $-13$ dB is obtained, with a power consumption of 5.4 mW. In [50], the use of LC networks as reactive loads is proposed, which turns the reflection-type phase shifter into a discrete one. However, it offers the advantage of an increased bandwidth.

In conclusion, the biggest difficulties when designing a reflection-type phase shifter lie in obtaining the full phase control range while maintaining low insertion loss (and low loss variation), while keeping a small circuit footprint.

## 1.3. Thesis goals

The goal of this thesis is, after reviewing the state of the art on reconfigurable reflectarrays an array lenses, to develop low-cost working prototypes of reconfigurable reflectarray and array lens antennas employing continuous phase shifters. As a function example, they will be employed for realizing beam steering in X-band.

A modular perspective following the guided-wave approach was preferred for easier optimization, and thus the first step consists of realizing the phase shifter most suitable for being implemented in the arrays. The design goals are full range phase agility of 360° for maximum tunability, low insertion loss and loss ripple to diminish its effect on the radiation pattern, and small circuit size to reduce the array element spacing, maintaining the low cost and low complexity focus. The reflection-type phase shifters offer good qualities, but they are constrained by the performance of the tunable load. The improvements found in the literature require significantly increasing the circuit size, or adding lumped components whose packaging parasitics negatively impact the performance of the circuit at X-band. A deconstruction of the reflection-type phase shifter, focusing on the hybrid coupler and the requirements of the tunable load for maximum performance should lead to new topologies that offer better solutions.

With the phase shifter unit established, the following goal is utilizing it for developing the tunable arrays. Since the reflectarray is the most studied antenna of the two, it should be easier to realize the implementation. Based on a fixed reflectarray topology, a study should establish the best way of inserting the phase shifter without having to make drastic changes to it. Considering that the phase shifter can be used as a one port network might lead to considerations that were not accounted for before. A design process has to be established and then validated with a tunable reflectarray prototype.

The number of tunable array lenses found in the literature are not as extensive, and thus developing one may require the employment of technologies that were not previously used in that context. With the objective of reducing the number of layers, the manufacturing complexity and the element spacing, a new unit cell proposal has to be made, whilst still using the guided-wave approach for being able to implement later improvements of the phase shifter. A prototype should be designed for experimental validation.

Finally, conclusions must be derived from the development of the tunable arrays, establishing the advantages and disadvantages found in their design process and results.

## 1.4. Thesis outline

This thesis has been organized in five chapters, starting with this introductory chapter, that describes the motivation of the thesis topic, establishes the goals to be met, and provides background on the technologies on which the present work is built.

Chapter 2 delves into the reflection-type phase shifters, which possess qualities appropriate for realizing phased arrays, due to low cost and zero power consumption. At first, additional matching networks are introduced and analyzed for controlling the performance of the phase shifter. They match the ports where the tunable loads are located to a complex impedance which offers the desired trade-off between phase agility and insertion loss. Due to the requirement of reducing the circuit footprint, the hybrid coupler and the matching networks are fused into a new single structure, allowing matching to different complex impedances and having distinct coupling coefficients while reducing the transmission lines width and length. The limits and advantages of this structure are explored. Afterwards, this new impedance transforming hybrid coupler is used to manufacture an optimized phase shifter. Finally, different techniques are introduced for equalizing the insertion losses beyond what was possible at the starting point.

Chapter 3 focuses on the realization of a tunable reflectarray following the guided-wave approach. A fixed reflectarray is first designed and measured, taking into consideration the effect of the angles of incidence from the impinging wave, which are not typically accounted for and can drastically affect the performance. The reflection-type phase shifter from Chapter 2 is re-evaluated in a topology that would fit the reflectarray best, becoming a one port structure which yields better phase agility, lower insertion loss and smaller footprint than the alternatives, while still offering further loss equalization by adding a single parallel resistor. The unit cell is optimized for the phase shifter inclusion and a working prototype is manufactured, capable of performing beam steering.

Chapter 4 tackles the problematic of the reconfigurable array lens design. Since using microstrip technology, as in the previous chapters, results in a more complicated structure, the use of substrate integrated waveguide is proposed, making a brief review of the technology and exploring the most convenient way of implementing the guided-wave approach. A novel phase shifter is proposed and manufactured, avoiding the use of hybrid couplers that would take up too much space, and instead replacing the typical reflection-type phase shifter with tilted slots loaded with the tunable impedances, resulting in a considerably miniaturized low-cost phase shifter. The design of an array lens is proposed, achieving beam steering in simulation results and manufacturing a prototype that serves as a proof of realizability.

Lastly, Chapter 5 summarizes the final conclusions extracted from each chapter, as well as the most important and original contributions that can be found in each of them. Then, several lines of research for continuing the thesis work are proposed, ranging from immediate and logical steps derived from the limitations of the work to longer-term proposals based on developing technologies.

CHAPTER 2

# Analysis and optimization of coupler based phase shifters

## 2.1. Introduction

In the modular approach of designing reconfigurable antennas, choosing and optimizing the right phase shifter can be considered the most important and challenging task. As discussed in the previous chapter, there are many types of phase shifters, both discrete and continuous. While reconfigurable antennas using discrete phase shifters are more common in the literature, they are limited by the number of tunable elements in the cell. If only one is used, the design is simple, but a large number of elements in the array are required to achieve high reconfiguration capabilities. On the other hand, if more tunable elements are introduced, the biasing and control circuitry gets more complex due to the independent bias needed for each element of the unit cell and the number of states that needs to be considered.

Continuous phase shifters offer the possibility of achieving a full phase control range with a single tunable element (that is, with every element in the cell sharing bias). Since the phase shift is dependent on the DC bias voltage, the number of states are limited only by the discretization of the control circuit. Using digital to analog converters (DACs) with high number of bits can offer phase precision lower than 1°, the precision being given by the phase control range divided by 2 to the power of the number of bits. This way, the reconfigurability of the antenna is high even when using a low number of elements, permitting a reduction of costs and size. There are, nevertheless, obstacles in achieving a good enough implementation of the phase shifter. First of all, it needs to be small so it can fit the unit cell and reduce the element spacing of the array. Secondly, it has to achieve a full phase control range for maximum reconfigurability. Thirdly, it requires small insertion loss and loss ripple in order to reap the maximum benefits from phase synthesis. And lastly, low cost and small power consumption, to favor its applicability. Due to the typical limited bandwidth of both array lenses and reflectarrays, the bandwidth of the phase shifter will not be taken into consideration.

Taking a look back at the different phase shifters presented in Chapter 1, the varactor-based reflection-type phase shifter seems to comply with most of the requirements. Traditionally, to increase the phase control range it requires the inclusion of a $\lambda/4$ parallel transmission line loaded with another tunable load [42] or the inclusion of LC networks [47,51]. Unfortunately, these techniques produce an enlargement of the circuit size, and an increase of the insertion loss and loss ripple, severely impacting the performance of the circuit.

This chapter breaks down the principle of operation of a reflection-type phase shifter and presents an analysis of the topology when implementing matching networks to optimize the tunable load. Then, a new 4-ports network based on hybrid couplers is presented, allowing to minimize the chip size enlargement while skirting implementation issues, and providing the groundwork for optimizing the loss ripple. It also introduces the main tunable element in the Thesis, the varactor diode Aeroflex MGV-125-25-0805-2, with a tunable voltage range of 0 to 20 V.

## 2.2. Analysis of the reflection-type phase shifter with impedance matching

### 2.2.1. Original topology

The original topology of the reflection-type phase shifters consists in a 3 dB 90° hybrid coupler with tunable loads at the end of its two coupled ports. The analysis of this circuit is well-known [52].

The scattering parameters of the ideal hybrid coupler, with isolation between ports 1 and 2, and between ports 3 and 4, are

$$[S_{hybrid}] = \begin{bmatrix} 0 & 0 & 1/\sqrt{2} & -j/\sqrt{2} \\ 0 & 0 & -j/\sqrt{2} & 1/\sqrt{2} \\ 1/\sqrt{2} & -j/\sqrt{2} & 0 & 0 \\ -j/\sqrt{2} & 1/\sqrt{2} & 0 & 0 \end{bmatrix}. \tag{2.1}$$

Given a tunable load of impedance $Z_L$, and in respect of the reference impedance $Z_0$, its reflection coefficient is

$$\Gamma = \frac{Z_L - Z_0}{Z_L + Z_0}. \tag{2.2}$$

Placing this impedance in ports 3 and 4 of Eq. (2.1), the S-matrix of the resulting two-ports network is

$$[S_{rtps}] = \begin{bmatrix} 0 & -j\Gamma \\ -j\Gamma & 0 \end{bmatrix}. \tag{2.3}$$

The signal gets canceled out in the input and its transmitted to the output with the same value as the reflection coefficient of the load. In the ideal case, it is offset by $j$,

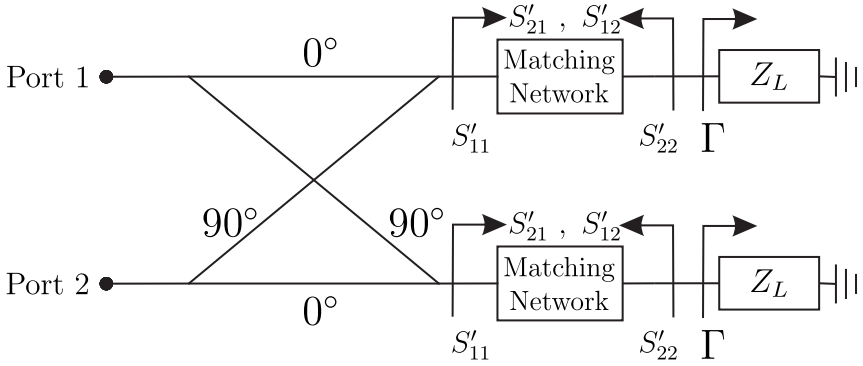


Figure 2.1: Topology of reflection-type phase shifter with impedance matching networks.

but in reality it would also be offset by the phase of the $S_{31}$ parameter of the hybrid coupler, here considered 0. It is concluded that in this topology the behavior of the phase shifter is solely defined by Γ. The goal, then, is to change the value of Γ. There are two ways to tackle this problem. One is changing the impedance of the tunable load through additional impedances, such as LC networks, and the other is changing the impedance it is referred to through an impedance matching network. Since monolithic microwave integrated circuits (MMIC) would tremendously rise fabrication costs, packaged inductors and capacitors ought to be used. It would then be necessary to take into account the packaging parasitics. The resulting impedances will differ from those necessary to achieve the impedance for the best phase shift range and insertion loss. Passive matching networks with transmission lines and stubs are a better choice, due to no increase in manufacturing costs, flexibility in design, and reliability.

### 2.2.2. Addition of impedance matching networks

The topology with the impedance matching is shown in Fig. 2.1. Two identical two-port matching networks are added next to the tunable loads. Their S-parameters matrix is:

$$\left[S'\right] = \begin{bmatrix} S'_{11} & S'_{21} \\ S'_{21} & S'_{22} \end{bmatrix}. \tag{2.4}$$

Considering an ideal hybrid coupler, the combination of coupler and matching networks is defined by

$$[S_{total}] = \begin{bmatrix} 0 & -j\,S'_{11} & \frac{S'_{21}}{\sqrt{2}} & \frac{-j\,S'_{21}}{\sqrt{2}} \\ -j\,S'_{11} & 0 & \frac{-j\,S'_{21}}{\sqrt{2}} & \frac{S'_{21}}{\sqrt{2}} \\ \frac{S'_{21}}{\sqrt{2}} & \frac{-j\,S'_{21}}{\sqrt{2}} & S'_{22} & 0 \\ \frac{-j\,S'_{21}}{\sqrt{2}} & \frac{S'_{21}}{\sqrt{2}} & 0 & S'_{22} \end{bmatrix}. \tag{2.5}$$

As in the case before, the signal gets canceled out at the input. Nevertheless, there is

a new expression for the transmission coefficient of the phase shifter:

$$S_{21} = -j \left( S'_{11} + \frac{(S'_{21})^2 \, \Gamma}{1 - S'_{22} \, \Gamma} \right). \tag{2.6}$$

The phase shifting is now related to the tunable load and the parameters of the matching network. In order to simplify the analysis, the network can be considered passive and lossless, establishing the following relations between its parameters:

$$|S'_{21}| = \sqrt{1 - |S'_{11}|^2} = \sqrt{1 - |S'_{22}|^2}. \tag{2.7}$$

In addition, considering arbitrary phases $\alpha$ and $\phi$ for $S'_{21}$ and $S'_{22}$ such that $S'_{21} = |S'_{21}| \, e^{j\alpha}$ and $S'_{22} = |S'_{22}| \, e^{j\phi}$, another relation is obtained:

$$S'_{11} = -|S'_{22}| \, e^{j(-\phi + 2\alpha)}. \tag{2.8}$$

Applying Eq. (2.7) and (2.8) to Eq. (2.6):

$$S_{21} = -j \, e^{j(2\,\alpha)} \, \frac{\Gamma - {S'_{22}}^*}{1 - S'_{22} \, \Gamma}. \tag{2.9}$$

And thus the phase shifter is defined by $\Gamma$ and $S'_{22}$. To further advance the analysis, the reflection coefficients are split into real and imaginary parts, so that $\Gamma = a + b\,j$ and $S'_{22} = c + d\,j$. Then, the magnitude of the transmission coefficient of the phase shifter is

$$|S_{21}| = \sqrt{\frac{(a-c)^2 + (b+d)^2}{(1 + b \cdot d - a \cdot c)^2 + (a \cdot d + b \cdot c)^2}}, \tag{2.10}$$

and its phase

$$\angle S_{21} = -\pi/2 + 2\,\alpha + \arctan\left(\frac{b+d}{a-c}\right) - \arctan\left(\frac{-a \cdot d - b \cdot c}{1 + b \cdot d - a \cdot c}\right). \tag{2.11}$$

The phase $\alpha$ is arbitrary and just offsets the phase as in the case of a non-ideal hybrid coupler. For maximum phase agility, the values of arctan as seen in (2.11) should be next to zero for values of $\Gamma$ at approximately the center biasing point of the tunable load. As such, there are two solutions: $b = -d$ and $a\,d = -b\,c$. However, when $b = -d$, insertion losses are increased due to a zero in the numerator of (2.10), making it an undesirable condition.

In summary, for achieving high phase agility and maintaining low insertion losses, it is found that $S'_{22}$ should meet

$$\frac{\mathrm{Re}(S'_{22})}{\mathrm{Im}(S'_{22})} = -\frac{\mathrm{Re}(\Gamma)}{\mathrm{Im}(\Gamma)} \tag{2.12}$$

while avoiding zeros in the numerator of (2.10) by complying with

$$\mathrm{Im}(\Gamma) \neq -\mathrm{Im}(S'_{22}), \tag{2.13}$$

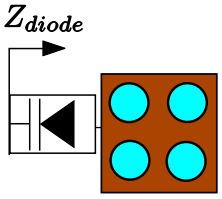


Figure 2.2: Schematic the circuit used to obtained the varactor model as a tunable load.

and

$$\mathrm{Re}(\Gamma) \neq \mathrm{Re}(S'_{22}). \tag{2.14}$$

As demonstrated, the performance of the phase shifter is controlled and can be optimized with the value of $S'_{22}$. Given that $\Gamma$ is immutable for a given tunable load, $S'_{22}$ should be adjusted for each load and for the desired phase control range and insertion loss. The effect is akin to changing the impedance $Z_L$ through the addition of inductors and capacitors, but with the added flexibility of realizing the matching network as the designer would see fit, either with stubs, lumped elements or quarter-wave transformers. In this way, a zero-cost improvement of the reflection-type phase shifter is realized, avoiding the inclusion of additional tunable loads, capacitors or inductors.

### 2.2.3. Parametric analysis

Since $S'_{22}$ is the reflection coefficient of a passive network, its module can never be more than 1. With a limited set of values, it is easy to sweep different real and imaginary parts and observe how it affects the phase shift range (difference between maximum and minimum phase shift) and insertion loss ripple (difference between maximum and minimum insertion loss).

To prove this, a S-parameters model was realized of the packaged diode varactor Aeroflex MGV-125-25-0805-2 at 9 GHz, which will be used as the primary tunable load in next analyses, simulations and prototype measurements. Since it will be used as a reflection load, shorted to ground, the varactor model was made with one end of the diode connected to a ground plane access through metalized via-holes as depicted in Fig. 2.2, to account for the via-holes parasitics. The varactor impedances obtained from the model, for key bias voltages, are shown in Table 2.1. Those are the tunable load impedances that will be used for optimizations and simulations.

With a reliable varactor model and Eq. (2.10), (2.11), the $S'_{22}$ real and imaginary parts are then swept and displayed in Fig. 2.3. There is a certain subset of values that, despite granting the highest phase agility, produces the highest losses. Those would be the values that meet Eq. (2.12) but do not meet Eq. (2.13) or (2.14). There are, though, other values that while not bestowing the highest phase agility, do not produce such a perturbation in the losses. Those would be the ones satisfying all the conditions. Still, there is some leeway to decide which exact trade-off is obtained between phase agility and insertion loss ripple.

| | | | | | |
|---|---|---|---|---|---|
| **Bias voltage (V)** | 0 | 1 | 2 | 3 | 4 |
| **Diode impedance (Ω)** | 10.801 +117.43j | 10.455 +114.93j | 11.077 +112.01j | 10.692 +107.59j | 9.9831 +102.74j |
| **Bias voltage (V)** | 5 | 6 | 7 | 8 | 9 |
| **Diode impedance (Ω)** | 9.0297 +98.0475j | 8.4471 +93.5596j | 8.0258 +88.8338j | 7.4886 +84.2391j | 7.0464 +79.977j |
| **Bias voltage (V)** | 10 | 11 | 12 | 13 | 14 |
| **Diode impedance (Ω)** | 6.7134 +75.2902j | 6.2306 +71.6176j | 5.8879 +67.4918j | 5.5499 +63.5442j | 5.2445 +60.0115j |
| **Bias voltage (V)** | 15 | 16 | 17 | 18 | 19 |
| **Diode impedance (Ω)** | 4.9406 +56.4806j | 4.6636 +53.0238j | 3.6747 +49.8399j | 3.4174 +46.8247j | 3.1992 +43.9899j |
| **Bias voltage (V)** | 20 | | | | |
| **Diode impedance (Ω)** | 3.0492 +41.3381j | | | | |

Table 2.1: Aeroflex MGV-125-25-0805-2 varactor impedance for different bias voltages.

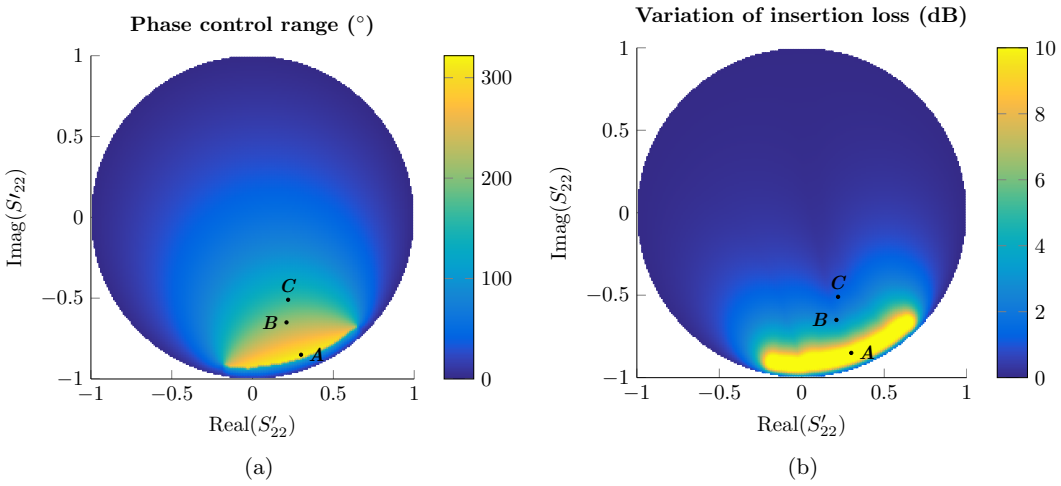


(a) (b)

Figure 2.3: Effects of various matching networks at 9 GHz for varactor Aeroflex MGV-125-25-0805-2. (a) Phase control range. (b) Insertion loss variation due to different matching points.

Some of the possible solutions are labeled in Fig. 2.3, with exact values of phase range and insertion loss ripple displayed in Table 2.2. Point A would correspond to a matching point with high phase range and loss/ripple, while B and C maintain good loss conditions while still achieving a significant increase in phase agility. For reference, the phase shift and loss produced at each bias voltage for each matching point are shown in Fig. 2.4. It also remarks how important it is to properly match the tunable load. From a measly 55° phase range, it can be more than tripled without significantly affecting the loss ripple. A bigger phase increase also produces a bigger loss ripple, getting to a point where it increases exponentially. It is also worth noting that phase linearity correlates with low insertion loss. Although non-linearity can be accounted for in the control circuitry, good

| | $S'_{22}$ | Phase range | Insertion loss variation |
|---|---|---|---|
| ***A*** | $0.9_{\angle 289.44°}$ | 312.5° | 18 dB |
| ***B*** | $0.68_{\angle 287.9°}$ | 210.7° | 2.65 dB |
| ***C*** | $0.55_{\angle 293.33°}$ | 160.3° | 1.39 dB |
| – | 0 | 54.88° | 0.21 dB |

Table 2.2: Comparison of matching points

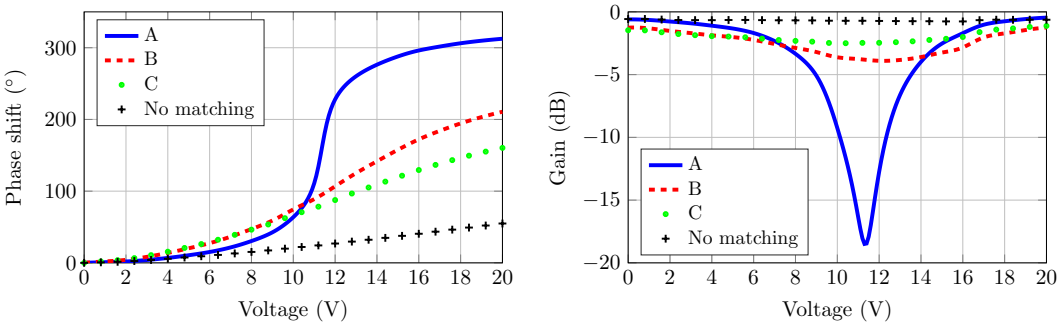


(a) (b)

Figure 2.4: Comparison between different matching points for a packaged varactor. (a) Phase shift. (b) Gain.

linearity is a boon to have, simplifying the choice of bias voltage.

The main drawback of this topology is the chip size. Not only a 90° hybrid coupler is required, which would already occupy an area of $\lambda/4 \times \lambda/4$, but it is also necessary to include two impedance matching networks, which in some scenarios may take up even the same space, doubling the area. It is then imperative to reduce the size of the impedance matching network, and that would be possible by implementing them in the hybrid coupler.

## 2.3. Complex impedance transforming hybrid coupler

### 2.3.1. Analysis

To improve on the previous topology, a hybrid coupler matched to a different impedance in two of its ports is needed. While there is existing work for impedance transforming hybrid couplers, it only refers to matching real impedances, and its use is limited by the feasibility of the line widths which can be used to obtain the matching impedances [53]. That is, it would not be possible to match an impedance so high that its equivalent line width is too small for the fabrication process. Other researches focus instead on achieving circuit miniaturization and bandwidth plus isolation enhancement through different techniques, including left-handed transmission lines [54], via-holes [55,56], air-gaps [57], stubs [49,58], coupled [59,60] and $\pi$ shaped lines [61].

In order to avoid the impedance limitation, and to achieve the complex impedance matching, the topology shown in Fig. 2.5 is proposed. Two ports will be matched to the

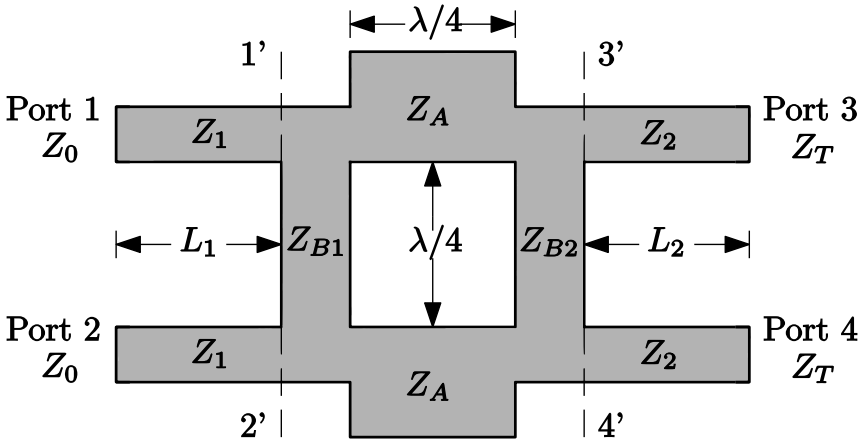


Figure 2.5: Diagram of the proposed hybrid coupler. Port locations of the original topology are marked with an apostrophe.

reference impedance $Z_0$, and the other two to a complex impedance $Z_T$. Two transmission lines of arbitrary impedance, $Z_1$ and $Z_2$, and arbitrary electrical length, $L_1$ and $L_2$, are added to each port, while keeping lines of 90° elsewhere. The additional lines will transform the branch impedances, $Z_{B1}$ and $Z_{B2}$, to $Z_0$ and $Z_T$ respectively.

Due to symmetry, passive and lossless conditions, the following relations between the scattering parameters are assumed:

$$|S_{11}|^2 + |S_{21}|^2 + |S_{31}|^2 + |S_{41}|^2 = 1 \tag{2.15}$$

$$|S_{33}|^2 + |S_{43}|^2 + |S_{31}|^2 + |S_{41}|^2 = 1 \tag{2.16}$$

where $S_{33} = \dfrac{{Z_T}^* - Z_0}{{Z_T}^* + Z_0}$. Also, $S_{33}$ would be analogous to the reflection coefficient parameter of the matching network $S'_{22}$ that was discussed in the previous section, since it is the reflection coefficient at the ports where the tunable loads would be located. $Z_T$, the matching impedance, is the design parameter that will be used to optimize the phase range and insertion loss of the phase shifter.

Considering that the coupling coefficient $k$ does not necessarily need to be 1, it is found that the relation between direct and coupled transmission coefficient is $|S_{31}| = k \cdot |S_{41}|$. Ports 1 and 2 have to be matched to the impedance reference, so $S_{11} = 0$, which also results in isolation between ports 3 and 4, $S_{43} = 0$. Applying these two conditions to Eq. (2.15) and (2.16), the following relations are obtained

$$|S_{21}| = |S_{33}| \tag{2.17}$$

$$|S_{41}| = \sqrt{\frac{1 - |S_{33}|^2}{1 + k^2}} \tag{2.18}$$

When every port is referenced to $Z_0$, there is no isolation between ports 1 and 2. The

magnitude of the full S-parameters matrix is as it follows:

$$[|S|] = \begin{bmatrix} 0 & |S_{33}| & k\cdot\sqrt{\frac{1-|S_{33}|^2}{1+k^2}} & \sqrt{\frac{1-|S_{33}|^2}{1+k^2}} \\ |S_{33}| & 0 & \sqrt{\frac{1-|S_{33}|^2}{1+k^2}} & k\cdot\sqrt{\frac{1-|S_{33}|^2}{1+k^2}} \\ k\cdot\sqrt{\frac{1-|S_{33}|^2}{1+k^2}} & \sqrt{\frac{1-|S_{33}|^2}{1+k^2}} & |S_{33}| & 0 \\ \sqrt{\frac{1-|S_{33}|^2}{1+k^2}} & k\cdot\sqrt{\frac{1-|S_{33}|^2}{1+k^2}} & 0 & |S_{33}| \end{bmatrix} \tag{2.19}$$

Every parameter other than $S_{11}$ and $S_{43}$ is related to $S_{33}$ and $k$. When ports 3 and 4 are renormalized to $Z_T$, the S-matrix ends up being that of a typical hybrid coupler:

$$[|S|] = \begin{bmatrix} 0 & 0 & \frac{k}{\sqrt{1+k^2}} & \frac{1}{\sqrt{1+k^2}} \\ 0 & 0 & \frac{1}{\sqrt{1+k^2}} & \frac{k}{\sqrt{1+k^2}} \\ \frac{k}{\sqrt{1+k^2}} & \frac{1}{\sqrt{1+k^2}} & 0 & 0 \\ \frac{1}{\sqrt{1+k^2}} & \frac{k}{\sqrt{1+k^2}} & 0 & 0 \end{bmatrix} \tag{2.20}$$

Obtaining these S-Parameters, plus a phase difference of 90° between $S_{31}$ and $S_{41}$ is the goal of the proposed hybrid (if this phase difference is not maintained, the reflection coefficient in ports 1 and 2 would not be 0 when a reflection load is placed in ports 3 and 4). To obtain the needed impedances and line lengths relationships, and thanks to the symmetry of the circuit, an even-odd analysis can be performed [62]. The resulting equations are unwieldy, but applying conditions from Eq. (2.19) will simplify them.

First of all, if the isolation condition $S_{43} = 0$ is applied to the resulting $Z_{B2}$, it is found that

$$\begin{aligned} Z_{B2} = {Z_A}^2 \frac{{Z_0}^2\,{Z_1}^2\cos(L_1)^2 + Z_0\,{Z_1}^3\sin(2\,L_1)\,j - {Z_1}^4\sin(L_1)^2}{{Z_1}^2\,Z_{B1}(Z_0\cos(L_1) + Z_1\sin(L_1)\,j)^2} + \\ + {Z_A}^2 \frac{{Z_1}^2\,{Z_{B1}}^2\cos(L_1)^2 - {Z_0}^2\,{Z_{B1}}^2\sin(L_1)^2 + Z_0\,Z_1\,{Z_{B1}}^2\sin(2\,L_1)\,j)}{{Z_1}^2\,Z_{B1}(Z_0\cos(L_1) + Z_1\sin(L_1)\,j)^2}. \end{aligned} \tag{2.21}$$

Then, applying the coupling condition, $S_{31} = j\cdot k\,S_{41}$, and the $Z_{B2}$ expression from Eq. (2.21), to $Z_{B1}$:

$$Z_{B1} = k\,Z_1\,\frac{Z_0 + j\,Z_1\,\tan(L_1)}{Z_1 + j\,Z_0\,\tan(L_1)}, \tag{2.22}$$

which, barring the coupling coefficient, resembles a transmission line transforming $Z_0$ to

$Z_{B1}$, made possible by the line of impedance $Z_1$ and electrical length $L_1$. Subsequently, applying the matching condition for ports 3 and 4, $S_{33} = \frac{{Z_T}^* - Z_0}{{Z_T}^* + Z_0}$, and Eq. (2.21), (2.22) to $Z_A$, it is obtained that

$$Z_A = \sqrt{\frac{Z_{B1}\, Z_{B2}}{1+k^2}}. \tag{2.23}$$

Substituting Eq. (2.21) with Eq. (2.22), (2.23),

$$Z_{B2} = k\, Z_2\, \frac{Z_T + j\, Z_2\, \tan(L_2)}{Z_2 + j\, Z_T\, \tan(L_2)}. \tag{2.24}$$

Analogously to $Z_{B1}$, the complex impedance $Z_T$ is transformed to $Z_{B2}$ by the transmission line with $Z_2$ impedance and $L_2$ length. Both $Z_{B1}$ and $Z_{B2}$ are defined by electrical lengths of an unknown value, but in order for the hybrid coupler to be feasible, their impedance must be real, so one condition has to be met: the imaginary parts of Eq. (2.22) and (2.24) must be 0. Thus,

$$L_1 = \arctan\left(\frac{{Z_1}^2 - |Z_0|^2 \pm \sqrt{\left(|Z_0|^2 + {Z_1}^2\right)^2 - \left(2\, Z_1\, \mathrm{Re}\{Z_0\}\right)^2}}{2\, Z_1\, \mathrm{Im}\{Z_0\}}\right) + n \cdot \pi, \tag{2.25}$$

and

$$L_2 = \arctan\left(\frac{{Z_2}^2 - |Z_T|^2 \pm \sqrt{\left(|Z_T|^2 + {Z_2}^2\right)^2 - \left(2\, Z_2\, \mathrm{Re}\{Z_T\}\right)^2}}{2\, Z_2\, \mathrm{Im}\{Z_T\}}\right) + n \cdot \pi, \tag{2.26}$$

where $n = \{0, 1\}$. For each length there are two different, but periodic solutions with period $\pi$. Each one of the two different solutions produces a different solution for $Z_{B1}$ and $Z_{B2}$. Since $Z_A$ depends on both impedances, and there are two solutions for each of them, there will be 4 possible values of $Z_A$, constituting four sets of solutions.

In conclusion, every impedance is well defined by the electric lengths $L_1$ and $L_2$, and the impedances $Z_1$ and $Z_2$. While the electric lengths must meet a specific criteria, $Z_1$ and $Z_2$ are left undefined, and their value must be chosen as to make every impedance feasible in a specific design problem, which will in turn be defined by the desired $Z_0$ and $Z_T$ impedances and the limits of impedance realizability.

### 2.3.2. Design procedure

Since $Z_1$ and $Z_2$ are not defined, the design procedure is not completely straightforward. The goal of the design is matching the hybrid to $Z_0$ in ports 1 and 2, to $Z_T$ in ports 3 and 4, and using a specific coupling coefficient $k$. Every impedance value, starting by $Z_1$ and $Z_2$, though exempting $Z_0$ and $Z_T$, must be realizable in the manufacturing process. It is the fabrication technology that defines what the lowest and highest possible impedances are. $Z_1$ and $Z_2$ must be chosen so that every impedance in the design is within the limits. For that, a random starting value can be assigned until a solution is reached, following the

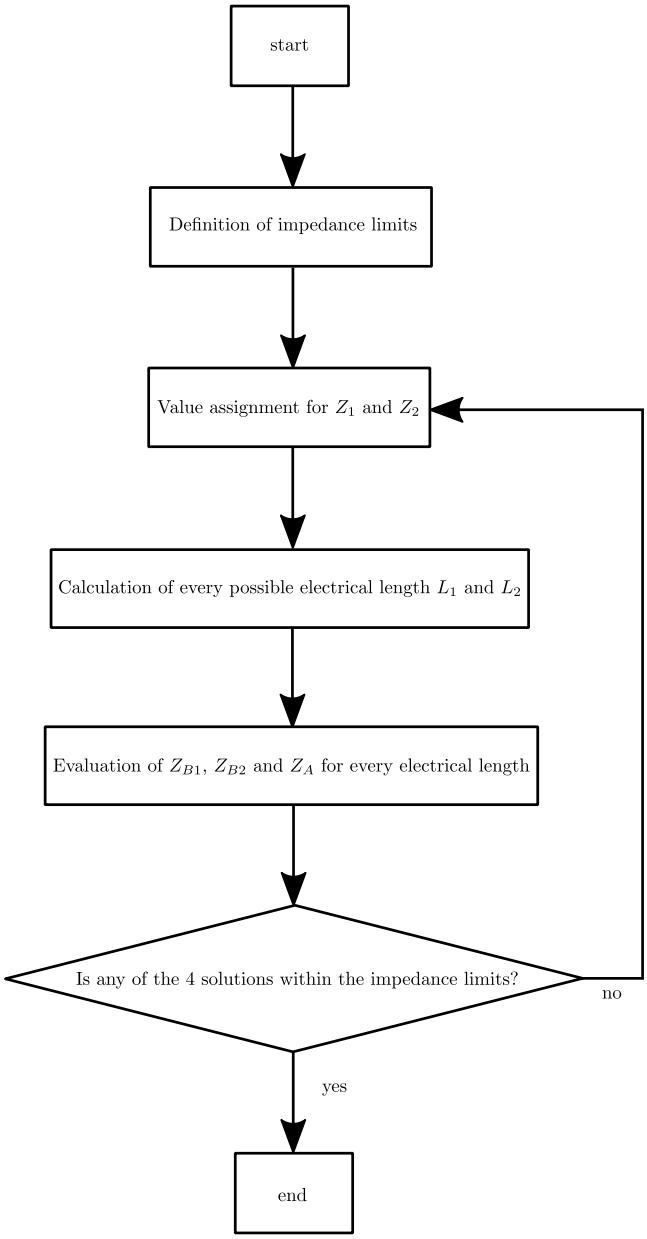


Figure 2.6: Flow chart of the design procedure for a complex impedance transforming hybrid coupler.

flow chart of Fig. 2.6. When a solution is not reached immediately, an in order to achieve faster convergence, an optimization algorithm such as gradient or quasi-Newton should be used to choose the next values of $Z_1$ and $Z_2$.

### 2.3.3. Impedance matching limitations

Different $Z_T$ values would impose their own restrictions in regards to which impedances and lengths must be used. Assuming a $Z_0 = 50\,\Omega$, coupling factor $k = 1$ and fabrication limits with a minimum impedance (due to not wanting a line width that would dramatically increase the circuit size) and a maximum impedance (due to smaller line widths not being

| $Z_T$ | $Z_1$ | $Z_2$ | $Z_{B1}$ | $Z_{B2}$ | $Z_A$ | $L_1$ | $L_2$ |
|---|---|---|---|---|---|---|---|
| 5 Ω | 57.24 Ω | 27.05 Ω | 65.53 Ω | 146.33 Ω | 69.25 Ω | 90 ° | 90 ° |
| 1000 Ω | 89.98 Ω | 149.49 Ω | 161.94 Ω | 22.35 Ω | 42.54 Ω | 90 ° | 90 ° |

Table 2.3: Set of solutions for matching real impedances with minimum impedance of 20 Ω and a maximum impedance of 150 Ω.

| $Z_T$ | $Z_1$ | $Z_2$ | $Z_{B1}$ | $Z_{B2}$ | $Z_A$ | $L_1$ | $L_2$ |
|---|---|---|---|---|---|---|---|
| 1 Ω | 32.91 Ω | 12.32 Ω | 21.66 Ω | 151.79 Ω | 40.55 Ω | 90 ° | 90 ° |
| 3500 Ω | 67.33 Ω | 192.38 Ω | 90.64 Ω | 10.57 Ω | 21.89 Ω | 90 ° | 90 ° |

Table 2.4: Set of solutions for matching real impedances with minimum impedance of 10 Ω and a maximum impedance of 200 Ω.

realizable), it is possible to study the effects of different $Z_T$ impedances on the rest of the parameters of the design.

#### 2.3.3.1. Real impedances

If $Z_T$ is real, then the electrical length $L_2 = 90\,^\circ$. Subsequently,

$$Z_{B2} = k\,\frac{{Z_2}^2}{Z_T} \tag{2.27}$$

For instance, with a minimum impedance of 20 Ω and a maximum impedance of 150 Ω,it would be impossible to achieve solutions for $Z_T$ below 3 Ω or above 1100 Ω. In Table 2.3 it is shown that for $Z_T$ close to those values, the resulting impedances are also close to the limits.

Reducing the lowest impedance limit to 10 Ω and increasing the highest impedance limit to 200 Ω improves the capability of matching to higher and lower impedances, as demonstrated in Table 2.4.

It is concluded that, in the case of real impedances, the higher the ratio $Z_T/Z_0$, the bigger the ratio of maximum to minimum impedance will be needed.

#### 2.3.3.2. Imaginary impedances

In the case of $Z_T$ being an imaginary impedance, there are two possible $L_2$ lengths, resulting in two different $Z_{B2}$ impedances. On one hand:

$$L_2 = \arctan\left(\frac{j\,Z_2}{Z_T}\right), \tag{2.28}$$

$$Z_{B2} = k\,Z_2\,\frac{Z_T - \dfrac{{Z_2}^2}{Z_T}}{Z_2 - Z_2} = \infty. \tag{2.29}$$

On the other:

$$L_2 = \arctan\left(\frac{j\,Z_t}{Z_2}\right), \tag{2.30}$$

$$Z_{B2} = k\,Z_2\,\frac{Z_T - Z_T}{Z_2 - \dfrac{{Z_T}^2}{Z_2}} = 0. \tag{2.31}$$

Neither impedance value is achievable. Consequently, imaginary impedances cannot be matched.

#### 2.3.3.3. Complex impedances

If $Z_T$ is complex, a new restriction is added to the real impedance case. It only applies to the branch-line and transforming impedances of the corresponding port, i.e., $Z_{B2}$ and $Z_2$, but it would also apply to $Z_{B1}$ and $Z_1$ if $Z_0$ were complex. Assuming as before, $Z_0 = 50\,\Omega$ and coupling $k = 1$, matching a complex $Z_T$ while forcing $Z_2 = 100\,\Omega$ yields the results shown in Table 2.5.

The more the $Z_T$ resembles a pure imaginary impedance (that is, the lower the ratio of real to imaginary part), the higher or lower the impedance $Z_{B2}$ will be, depending on which $L_2$ length is chosen. When the imaginary part is several orders of magnitude higher than the real part, the values of $Z_{B2}$ are closer to those in the case of a pure imaginary impedance. In conclusion, the bigger the imaginary part, the more difficult it will be to match.

### 2.3.4. Measurements

To validate the analysis performed in this section, three different complex impedance transforming hybrids were designed, manufactured an measured. In each case, the coupling factor chosen was 1, making they hybrid balanced. At first the hybrids parameters were

| $\boldsymbol{Z_T}$ | $\boldsymbol{L_{2_1}}$ | $\boldsymbol{Z_{B2_1}}$ | $\boldsymbol{L_{2_2}}$ | $\boldsymbol{Z_{B2_2}}$ |
|---|---|---|---|---|
| $70 - 20j\,\Omega$ | $20.2°$ | $65.2\,\Omega$ | $290.2°$ | $153.37\,\Omega$ |
| $70 - 200j\,\Omega$ | $65.55°$ | $12.96\,\Omega$ | $335.55°$ | $771.32\,\Omega$ |
| $70 - 2000j\,\Omega$ | $87.14°$ | $0.17\,\Omega$ | $357.14°$ | $57356\,\Omega$ |

Table 2.5: Effects of the imaginary part for matching complex impedances on the possible values of a branch-line impedance. Extra numerical suffixes indicate the two possible solutions for each case.

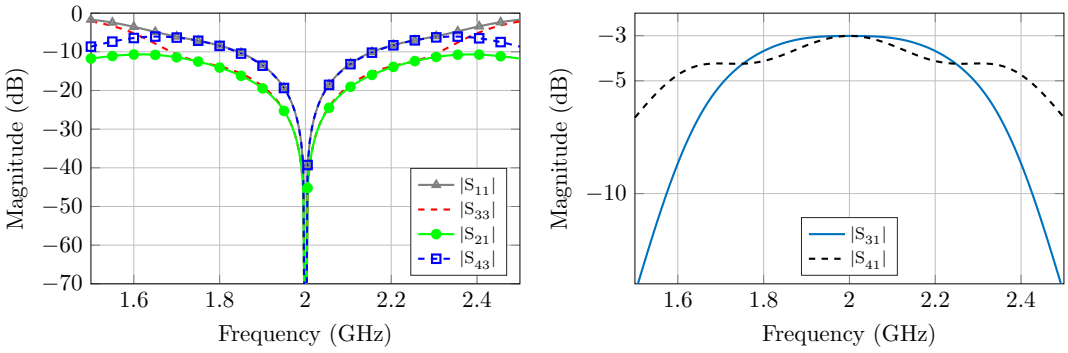


Figure 2.7: Simulation with ideal transmission lines of the complex impedance transformer. (a) Reflection. (b) Transmission in direct and coupled ports.

| | $Z_1$ | $Z_2$ | $Z_{B1}$ | $Z_{B2}$ | $Z_A$ | $L_1$ | $L_2$ |
|---|---|---|---|---|---|---|---|
| **Initial** | 78.4 Ω | 127.4 Ω | 123.1 Ω | 19 Ω | 34.2 Ω | 90° | 59.7° |
| **Final** | 78.5 Ω | 128.2 Ω | 123 Ω | 19 Ω | 34.2 Ω | 90° | 56° |

Table 2.6: Initial and final values for impedances and lengths of the complex hybrid coupler.

calculated using Eq. (2.22) to (2.26) and the design procedure of Fig. 2.6. Then, they were designed at 2 GHz in microstrip technology and optimized through a full-wave simulator in order to account for the effects of discontinuities and T-junctions. The substrate used is a 30 mil thick Arlon 25N with dielectric constant $\epsilon_r = 3.38$ and loss tangent of 0.0025.

The reference impedance chosen $Z_0$ is 50 Ω, to match that of the network analyzer used to perform the measurements. To understand the measurements more easily, the ports 3 and 4 were later renormalized to $Z_T$, that way making the resulting S-parameters resemble those of Eq. (2.20). Since these prototypes were designed just to prove the aforementioned analysis, the picked $Z_T$ values were not chosen to optimize a phase shifter, but to demonstrate the applicability and improvements over existing works.

#### 2.3.4.1. Complex impedance transformer

This prototype was designed to match a complex impedance $Z_T = 70 - 200j\,\Omega$. The initial parameters were obtained through the presented equations (matching and isolation shown in Fig. 2.7), and then they were optimized for microstrip lines through a full-wave simulator. Shown in Table 2.6, there is almost no change in the values.

The manufactured hybrid is shown in Fig. 2.8. It covers an area of $66.1 \times 33.9$ mm$^2$. 50 Ω lines were added at each port to perform TRL calibration. Its S-parameters are depicted in Fig. 2.9. Due to its symmetry and reciprocity, only the relevant $S$ parameters are shown. There is a very good agreement between simulations and measurements, and also with the ideal transmission lines simulation from Fig. 2.7. The hybrid presents return

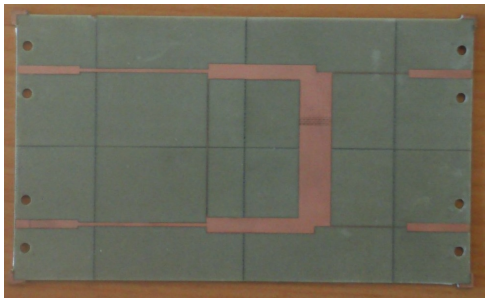

Figure 2.8: Picture of the complex impedance transformer prototype.

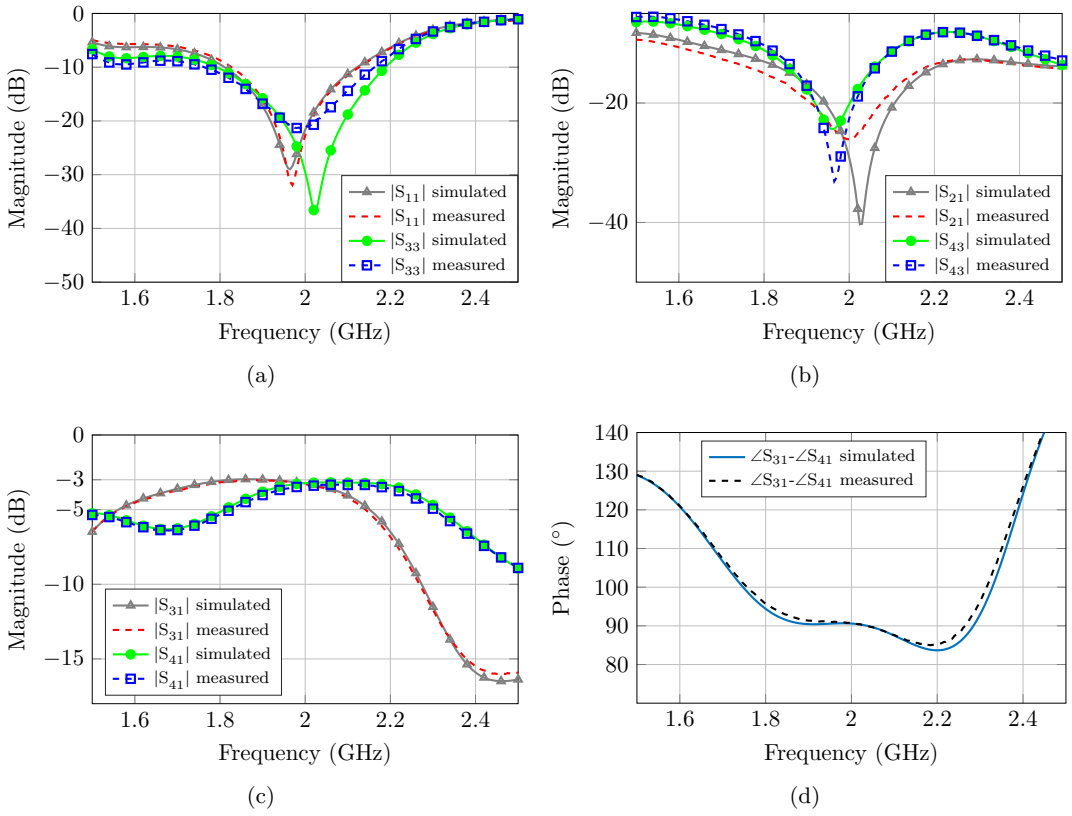


Figure 2.9: Simulation and measurements of the complex impedance transformer prototype. (a) Reflection. (b) Transmission in isolated ports. (c) Transmission in direct and coupled ports. (d) Phase difference between transmission coefficients.

loss and isolation between adjacent ports above 20 dB at 2 GHz. The return loss above 10 dB at ports 1 and 2 is the most limiting factor in bandwidth, resulting in a roughly 14.75% bandwidth centered on 2 GHz, yielding an amplitude balance of $3.85 \pm 0.85$ dB and a phase balance of $90.12° \pm 3.64°$.

#### 2.3.4.2. Real impedance transformer

Without the additional lines introduced in the hybrid, $Z_{B2} = \frac{Z_T}{k}$, meaning that if the impedance $Z_T$ is not realizable, so is the hybrid. With the technology available to the author of this Thesis, it is impossible to achieve a microstrip line with a line width lower

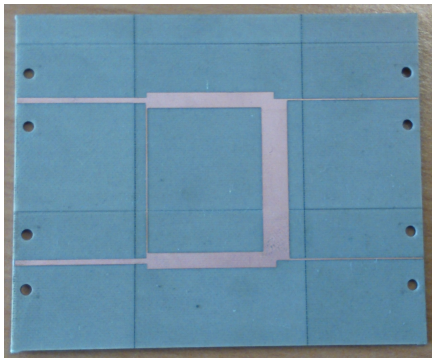

Figure 2.10: Picture of the real impedance transformer prototype.

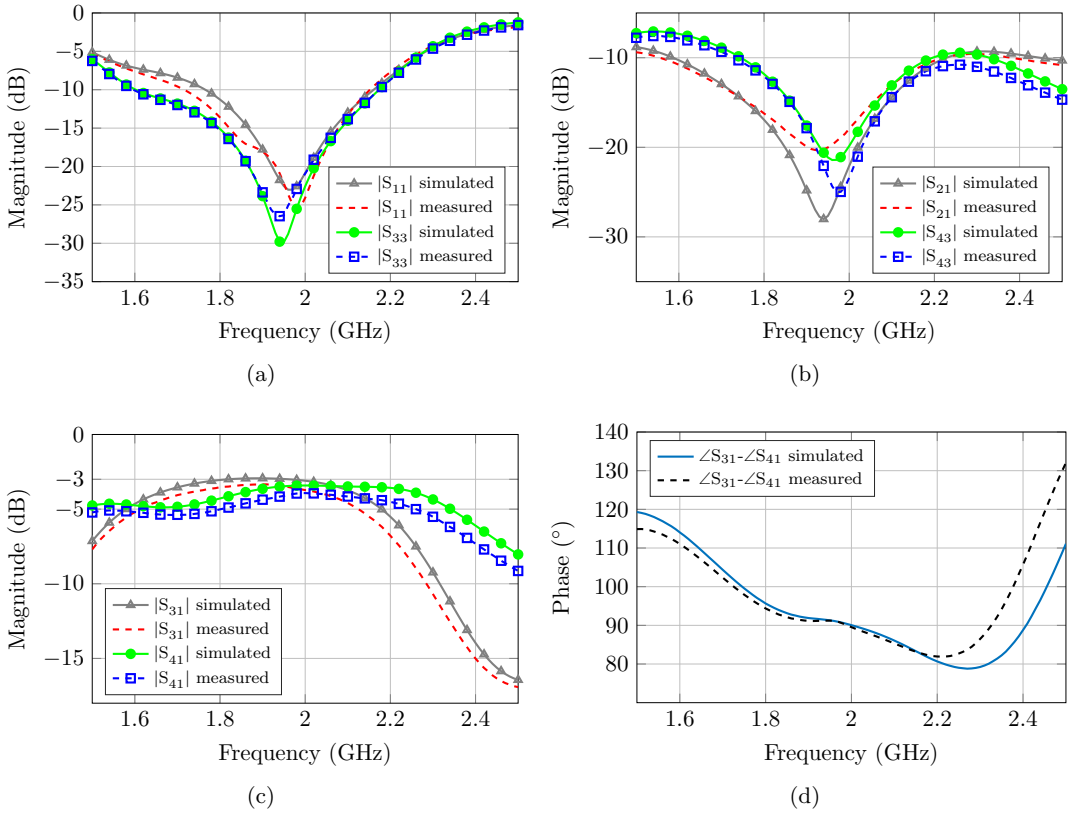


Figure 2.11: Simulation and measurements of the real impedance transformer prototype. (a) Reflection. (b) Transmission in isolated ports. (c) Transmission in direct and coupled ports. (d) Phase difference between transmission coefficients.

than 0.2 mm. For instance, a 450 Ω line would need a width as small as 31 nm, which is 4 orders of magnitude below the lower limit. Nevertheless, the proposed topology overcomes this limitation in fabrication, and to show it, a real impedance transforming hybrid with $Z_T = 450\,\Omega$ was designed and manufactured.

As in the case of the complex impedance transformer, the initial parameters were calculated using the equations obtained from the even-odd analysis, and then optimized with a full-wave simulator, obtaining the final impedances $Z_1 = 64.3\,\Omega$, $Z_{B1} = 132.43\,\Omega$,

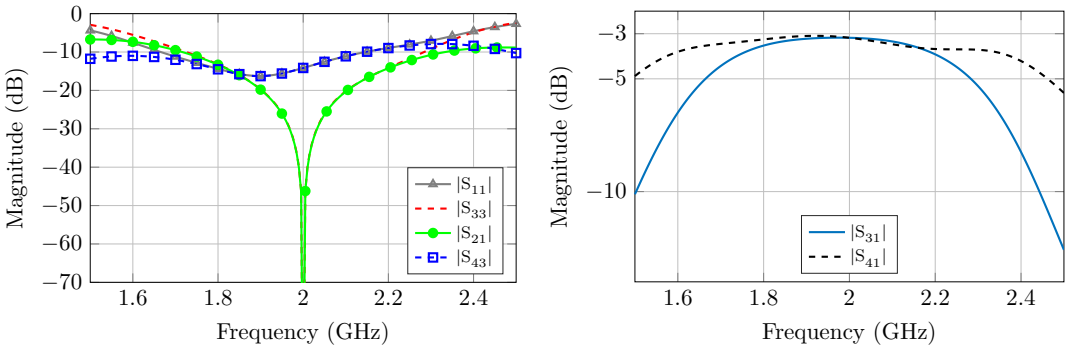


Figure 2.12: Simulation with ideal transmission lines of the reduced complex impedance transformer. (a) Reflection. (b) Transmission in direct and coupled ports..

$Z_A = 35.7\,\Omega$, $Z_{B2} = 25\,\Omega$ and $Z_2 = 90.36\,\Omega$, with every line measuring 90°.

The prototype, shown in Fig. 2.10, covers an area of $71 \times 31.5$ mm$^2$. Observing the $S$ parameters shown in Fig. 2.11, the circuit presents matching above 20 dB and isolation between ports above 15 dB at 2 GHz. The matching at ports 1 and 2 is the most limiting factor in bandwidth, resulting in a roughly 21% bandwidth centered on 2 GHz, yielding an amplitude balance of $4.35 \pm 1$ dB and a phase balance of $92.16° \pm 8.8°$. Although the amplitude balance is higher than in other couplers, it is due to the high $Z_T$ to $Z_0$ ratio. Nonetheless, the behaviour can be considered similar to that of a typical, non-transforming hybrid coupler.

#### 2.3.4.3. Reduced complex impedance transformer

The idea of impedance transforming hybrids was spurred from the necessity of reducing the reflection-type phase shifter comprised of a hybrid coupler and impedance transforming networks. Still, since $Z_0$ is always a real impedance, the electrical length of $L_1$ keeps being 90°. At first glance it could appear that this length must be kept unchanged, but that would only be the case if absolute perfect matching was necessary, which in practice will never be achieved. A good enough matching is one that yields return loss above 10 dB. Thus, the hybrid could be matched to a different impedance whose reflection coefficient respect $Z_0$ is below −10 dB. One way to go about it is choosing an impedance with the same real part as $Z_0$, but adding a small imaginary part. That way the length $L_1$ could be drastically reduced.

In this case, the hybrid was designed to be matched to a complex impedance $Z_0 = 50 - 20j\,\Omega$, which should yield a return loss for a $50\,\Omega$ port of 14 dB. The $Z_T$ impedance is again $70 - 200j\,\Omega$, in order for the hybrid to be compared with the previously measured complex impedance one, and to ascertain how this change affects the performance. With ports 1 and 2 still referenced to $50\,\Omega$, the simulation with ideal transmission lines, with values obtained from Eq. (2.23) to (2.26) and depicted in Fig. 2.12, shows similar results to those of the other hybrid, but with the matching not achieving quite the same values (maximum return loss around 15 dB instead of 25 dB).

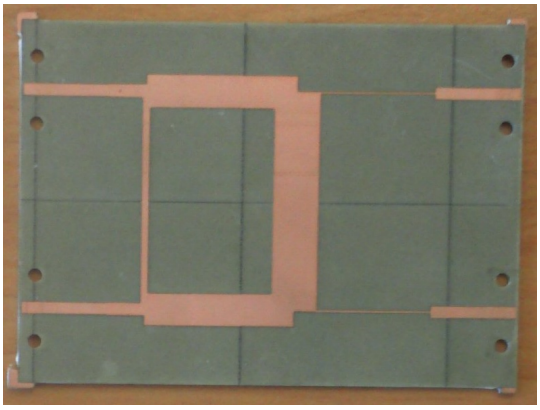

Figure 2.13: Picture of the reduced complex impedance transformer prototype.

The impedance and line length values were again optimized through HFSS, obtaining values similar to the initial ones, as shown in Table 2.7. The measured circuit, shown in Fig. 2.13, covers an area of $46.8 \times 35.9$ mm$^2$, taking up just 75% of the area occupied by the previously designed complex impedance hybrid transformer. Again, $50\,\Omega$ lines were added for TRL calibration.

There is still good agreement between measured and simulated S-parameters, plotted in Fig. 2.14. While the return loss in ports 1 and 2 is now below 20 dB, it is worth noting that the bandwidth has increased to 22.5%. The amplitude balance is $4 \pm 0.9$ dB and the phase balance is $93.22° \pm 6.74°$. While slightly worse than before, this is due to the extended bandwidth.

All in all, the circuit size was reduced with no significant disadvantage. This length reduction could also have been applied in the real impedance case, and since the two port impedances, $Z_0$ and $Z_T$, were real, both line lengths $L_1$ and $L_2$ could have been made smaller, resulting in an even more notable circuit size trimming.

## 2.4. Reflection-type phase shifter with complex impedance transforming hybrid couplers

### 2.4.1. Effects of the matching on a phase shifter

Having obtained a 4-ports network which acts as a 90° hybrid coupler with impedance matching networks, all that remains is using it as a reflection-type phase shifter. The

| | $Z_1$ | $Z_2$ | $Z_{B1}$ | $Z_{B2}$ | $Z_A$ | $L_1$ | $L_2$ |
|---|---|---|---|---|---|---|---|
| **Initial** | $38\,\Omega$ | $127\,\Omega$ | $64.5\,\Omega$ | $19\,\Omega$ | $24.7\,\Omega$ | $23.1°$ | $59.7°$ |
| **Final** | $47.5\,\Omega$ | $118.1\,\Omega$ | $64.6\,\Omega$ | $19\,\Omega$ | $24.7\,\Omega$ | $18.8°$ | $60°$ |

Table 2.7: Initial and final values for impedances and lengths of the reduced complex impedance transformer.

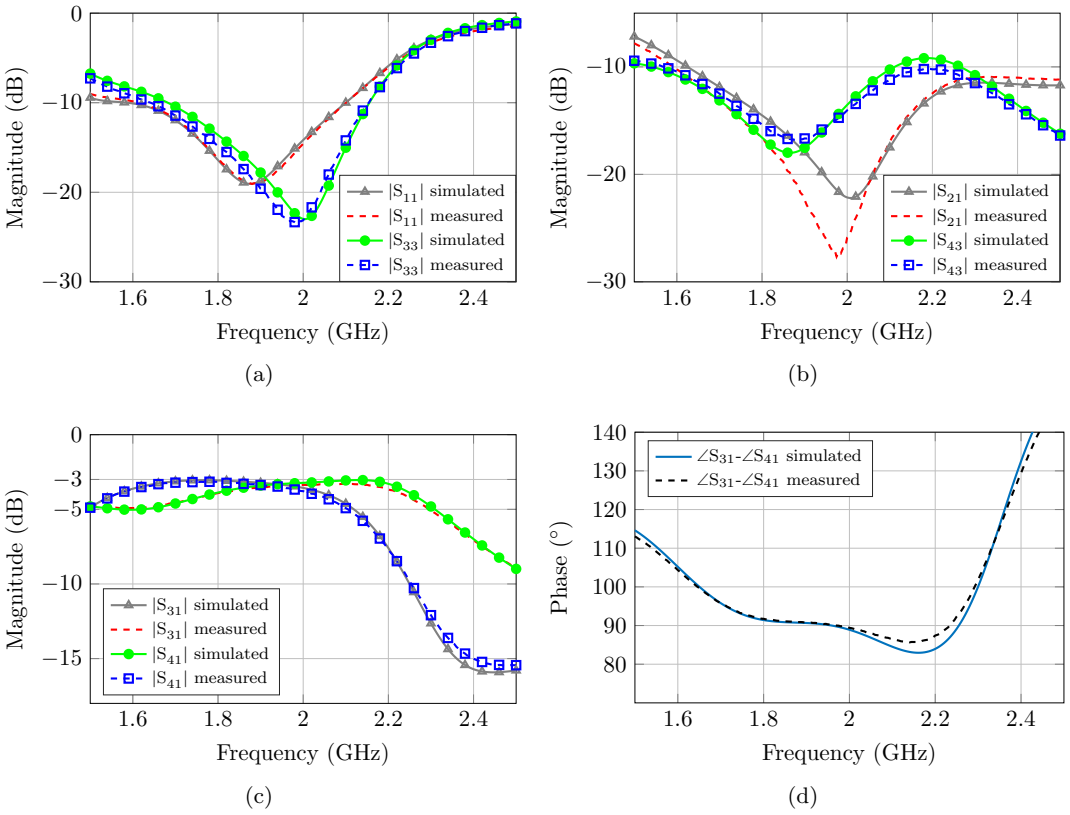


Figure 2.14: Simulation and measurements of the reduced complex impedance transformer prototype. (a) Reflection. (b) Transmission in isolated ports. (c) Transmission in direct and coupled ports. (d) Phase difference between transmission coefficients.

scattering parameters from the topology in Fig. 2.1 can be referred to those from the impedance transforming hybrid coupler from Fig. 2.5. Before, the reflection coefficient $S'_{22}$ of the impedance matching networks was shown to be the one that must be defined for a desired phase shifter performance. Now, with the impedance transforming hybrid couplers, it is the matching impedance $Z_T$, or the analogous reflection coefficient $S_{33}$, which will control the phase range and insertion loss/ripple. Furthermore, the arbitrary phase of the $S'_{21}$ parameter is now the phase of the direct transmission coefficient $S_{31}$ of the hybrid coupler. That phase is dependent on the electrical lengths $L_1$ and $L_2$, the impedance discontinuities and T-junctions. The phase shifter transmission coefficient from Eq. (2.9) can now be expressed with the new nomenclature:

$$S_{21ps} = -j\, e^{j(2\angle S_{31})}\, \frac{\Gamma - {S_{33}}^*}{1 - S_{33}\,\Gamma}. \tag{2.32}$$

The phase shifter behaves exactly as before, so a new parameter analysis for choosing the best matching point is not needed. Designing the coupler is as simple as obtaining $Z_T$ from

$$Z_T = Z_0\, \frac{1 + {S_{33}}^*}{1 - {S_{33}}^*}, \tag{2.33}$$

| $W_1$ | $L_1$ | $W_2$ | $L_2$ | $W_3$ | $L_3$ | $W_4$ | $L_4$ | $W_5$ |
|---|---|---|---|---|---|---|---|---|
| 0.44 | 4.1 | 0.85 | 4.18 | 4.68 | 0.96 | 0.89 | 7.02 | 0.28 |

Table 2.8: Geometry values of the reflection-type phase shifter based on a complex impedance transforming hybrid coupler. All measures are in mm.

and following the established design procedure.

Due to effects from discontinuities and T-junctions, which are exacerbated at higher frequencies, the S-parameters obtained from the full-wave simulation vary slightly depending on what impedance it is renormalized to. While in ports 1 and 2 there will always be a $Z_0$ impedance, tunable impedances will be located in ports 3 and 4. That means that if the circuit was optimized for $Z_T$, it would be found that when using other impedances, the matching or isolation would be lower than expected, and that the coupling or phase difference between $S_{31}$ and $S_{41}$ has changed, to the detriment of the phase shifting performance.

Therefore, in order to achieve the best results, the optimization process must consider every impedance value of the tunable load. The most sure way of conducting it consists in obtaining the 4-ports S-parameters matrix from the full-wave simulator, and evaluating, for each impedance value of the tunable load, the phase shift and insertion loss of the transmission parameter from Eq. 2.32, ensuring the desired phase range and insertion loss variation. It is also capital to make sure that the matching is within acceptable levels, which depends mostly on the coupling factor $k$ being one, allowing the sum of the signals reflected by the tunable loads to be canceled out at the input port. The flow chart of this procedure is depicted in Fig. 2.15.

To prove the validity of this approach, a new phase shifter using a complex impedance transforming hybrid will be designed. Using once more the varactor Aeroflex MGV-125-25-0805-2 as tunable load at 9 GHz, the reflection coefficient $S_{33} = 0.17 - 0.59j$ is chosen so as to obtain an expected 183.5° phase range and a 1.9 dB insertion loss variation. The initial parameters calculated from Eq. (2.22) to (2.26) will be optimized again through a full-wave simulator, using microstrip technology on the substrate Arlon 25 N, of 30 mil thickness, $\epsilon_r = 3.38$ and loss tangent of 0.0025. From now on and for reproducibility purposes, the geometry parameters of reflection-type phase shifter based on transforming hybrid couplers will be defined based on those from Fig. 2.16.

A prototype was designed and manufactured, shown in Fig. 2.17 with measures from Table 2.8. An open circuit radial stub was added in the middle of one of the branch-lines to isolate the DC bias circuitry while keeping symmetry. Also, due to the small size of the circuit, 50 Ω bent lines were adjoined to make space for the connectors. The size of the directional coupler is $10.41 \times 11.7\text{mm}^2$ , which is equivalent to $0.51\lambda_0 \times 0.58\lambda_0$, where $\lambda_0$ is the wavelength in free space. For reference, a phase shifter comprising a compact 3 dB 90° hybrid coupler and matching networks realized through stubs —for same frequency, substrate, and $S_{33}$— would require an area of $0.815\lambda_0 \times 1.03\lambda_0$. In that case, the area reduction is more than 60%.

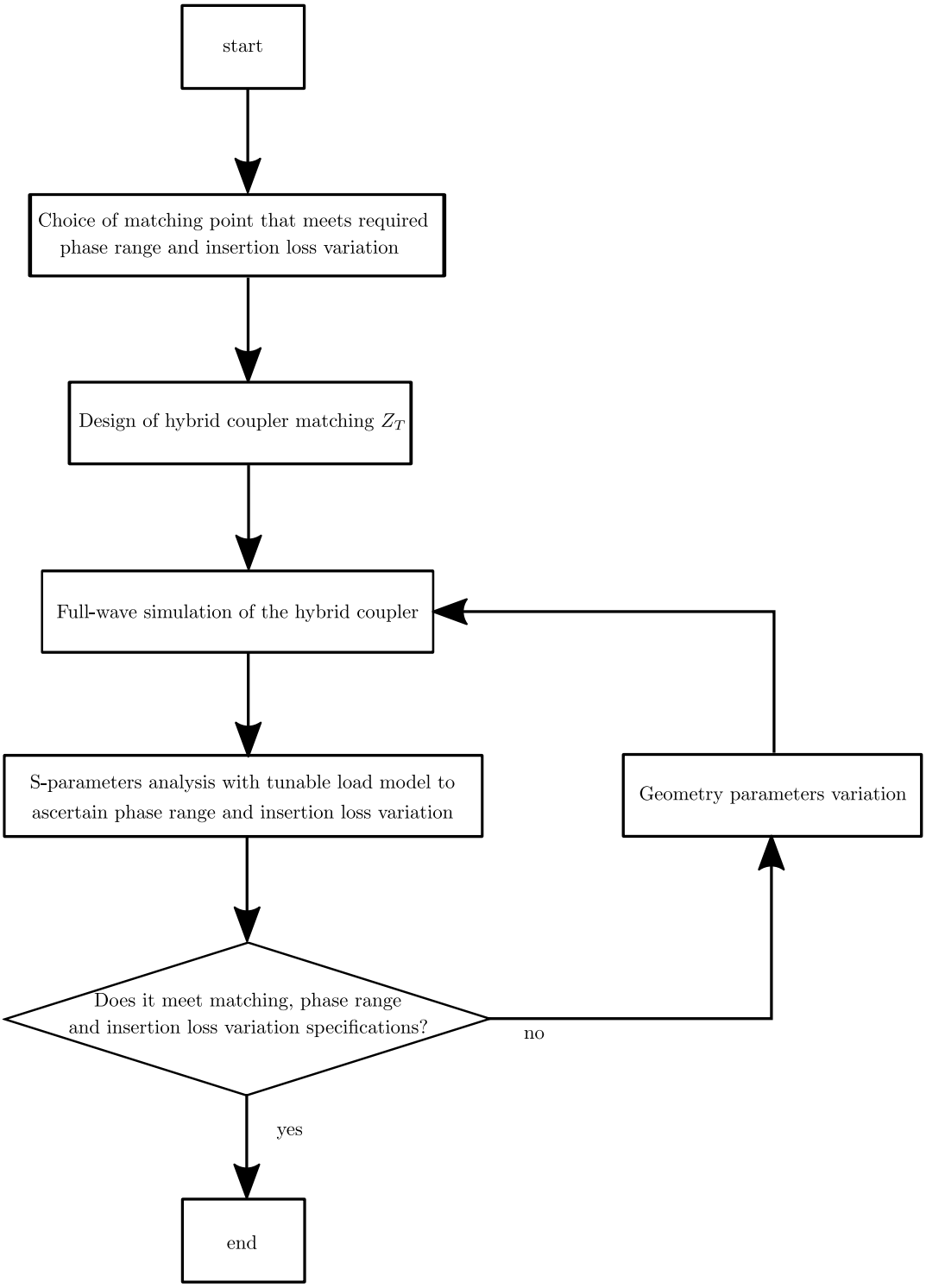


Figure 2.15: Flow chart of the design procedure for a reflection-type phase shifter based on a complex impedance transforming hybrid coupler.

Fig. 2.18 stacks up the full-wave simulation of the prototype against its measurements. The variation in the phase shift is nearly negligible, producing a phase range of 180.3 °. Even so, a noticeable discrepancy is observed in gain. The insertion loss variation has

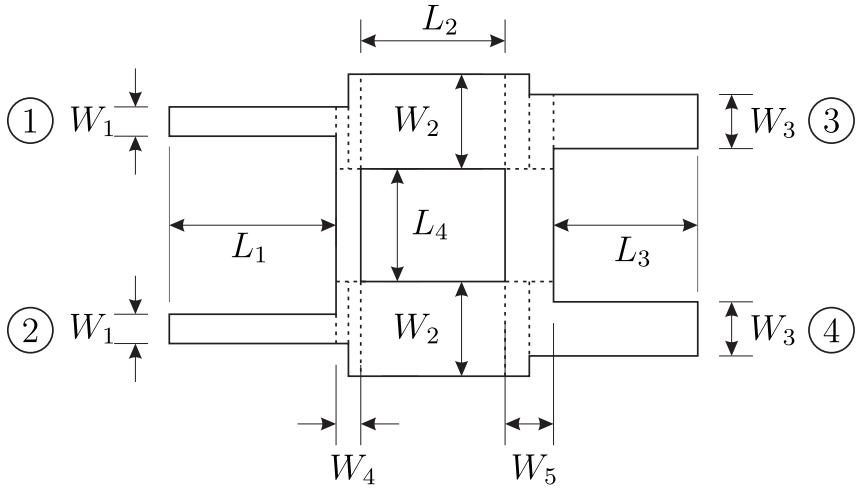


Figure 2.16: Geometry definition of the reflection-type phase shifter based on a complex impedance transforming hybrid coupler. Circled numbers represent the ports nomenclature.

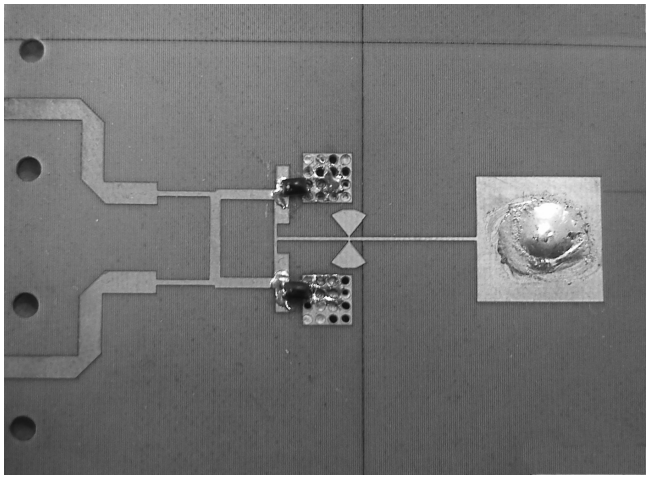

Figure 2.17: Picture of the reflection-type phase shifter based on complex impedance transforming hybrid coupler prototype.

increased, amounting to 2.2 dB. This is occasioned by a difference in impedance from each reflection load, attributed to a tolerance in the variable capacitance usually accounted for by the manufacturers. Applying this phenomena to the full-wave simulations prompts the expected increase of insertion loss and mismatching while maintaining an undifferentiated phase shift.

There are two parameters to consider which frequencies are included in the working bandwidth: phase shift range, and insertion loss variation. Results are shown in Fig. 2.19. The insertion loss variation remains under 3 dB from 8 to 9.85 GHz, proving to be quite stable. The phase shift range is above 150 ° from 8.6 to 9.5 GHz, restraining the bandwidth.

In summary, the switching from regular hybrid with impedance matching networks to reflection-type phase shifters based on complex impedance matching networks is a resounding success. The same phase shifting performance is obtained at a fraction of the

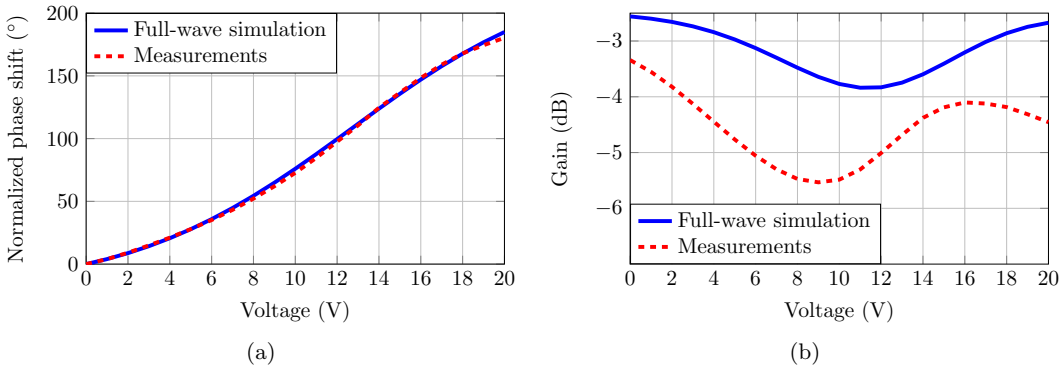


Figure 2.18: Comparison of simulation and measurements for the reflection-type phase shifter based on a complex impedance transforming hybrid coupler prototype. (a) Normalized phase shift. (b) Gain.

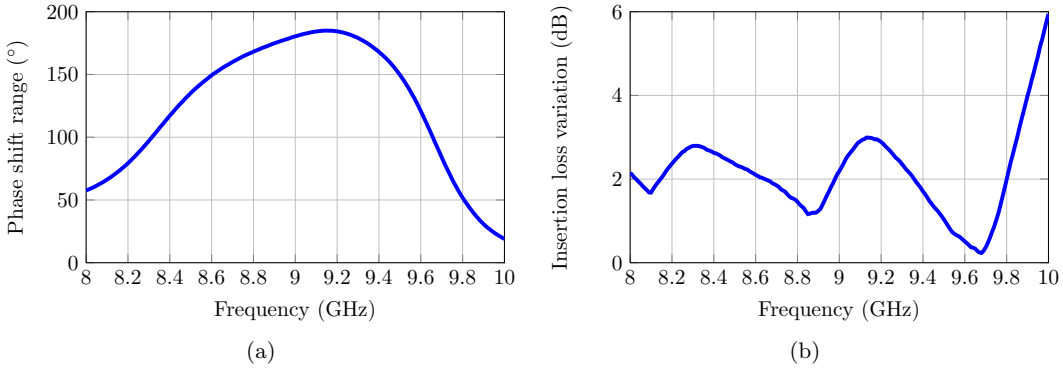


Figure 2.19: Measured bandwidth response of the reflection-type phase shifter based on a complex impedance transforming hybrid coupler prototype. (a) Phase shift range. (b) Insertion loss ripple.

chip size.

### 2.4.2. Methods for equalizing the insertion loss

Since the primary application of the discussed phase shifter is its integration in phased antennas, the insertion loss variation is a very important specification to consider. Since the amplitude changes for each phase, that would produce an increase of the side lobe levels in the radiation pattern of the array. So, in order to achieve the best possible result, it is imperative to equalize the losses as much as possible. Of course, that would come at a cost of either worse matching or an increase of the insertion losses mean but, be that as it may, the trade-off is worth it when those are already at a more than acceptable level.

#### 2.4.2.1. Lossy structure

Up to this point, every structure has been considered lossless. However, lossy structure have their advantages. The use of resistors for equalizing losses has been studied, requiring, however, the use of LC networks [63] or additional tunable loads [64]. The problem arises

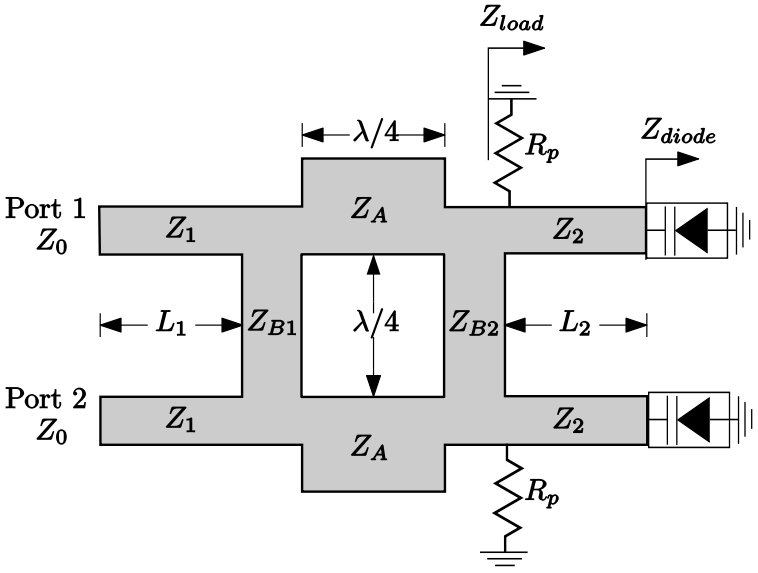


Figure 2.20: Diagram of the proposed phase shifter with parallel resistances.

in determining where to place the resistors in the complex impedance transforming hybrid coupler.

In the literature, resistors are placed in parallel to the varactors after using inductors to ensure that their imaginary impedance goes from capacitive to inductive, extracting the maximum possible phase range. If something of the sorts were done in the hybrid, a resistor could be placed at the point in which the diode impedance undergoes that transformation.

Another take on the analysis of the complex impedance hybrid coupler reveals the location in which a transformation of the varactor impedance occurs that may enable the transition from capacitive to inductive. The topology is shown in Fig. 2.20. Starting from the ports where the tunable load is placed, it can be seen that the line with $Z_2$ impedance and $L_2$ length acts as an impedance transformer, resulting in a new impedance load located at its end (assuming no parallel resistance):

$$Z_{load} = Z_2 \, \frac{Z_{diode} + j \, Z_2 \, \tan(L_2)}{Z_2 + j \, Z_{diode} \, \tan(L_2)}. \tag{2.34}$$

Considering the rest of the circuit as a regular impedance transforming hybrid, $Z_{B2}$ would equal $Z_T$, and since the branch impedance has to be real, so will be $Z_T$, and by extension, $S_{33}$. Applying this condition in Eq. 2.32 it is obtained that the transmission coefficient of the phase shifter follows:

$$S_{21_{ps}} = -j \, e^{2j\angle S_{31}} \, \frac{Z_{load} - Z_{B2}}{Z_{load} + Z_{B2}}. \tag{2.35}$$

Its module is

$$\left|S_{21_{ps}}\right| = \sqrt{\frac{(\mathrm{Re}(Z_{load}) - Z_{B2})^2 + \mathrm{Im}(Z_{load})^2}{(\mathrm{Re}(Z_{load}) + Z_{B2})^2 + \mathrm{Im}(Z_{load})^2}}, \tag{2.36}$$

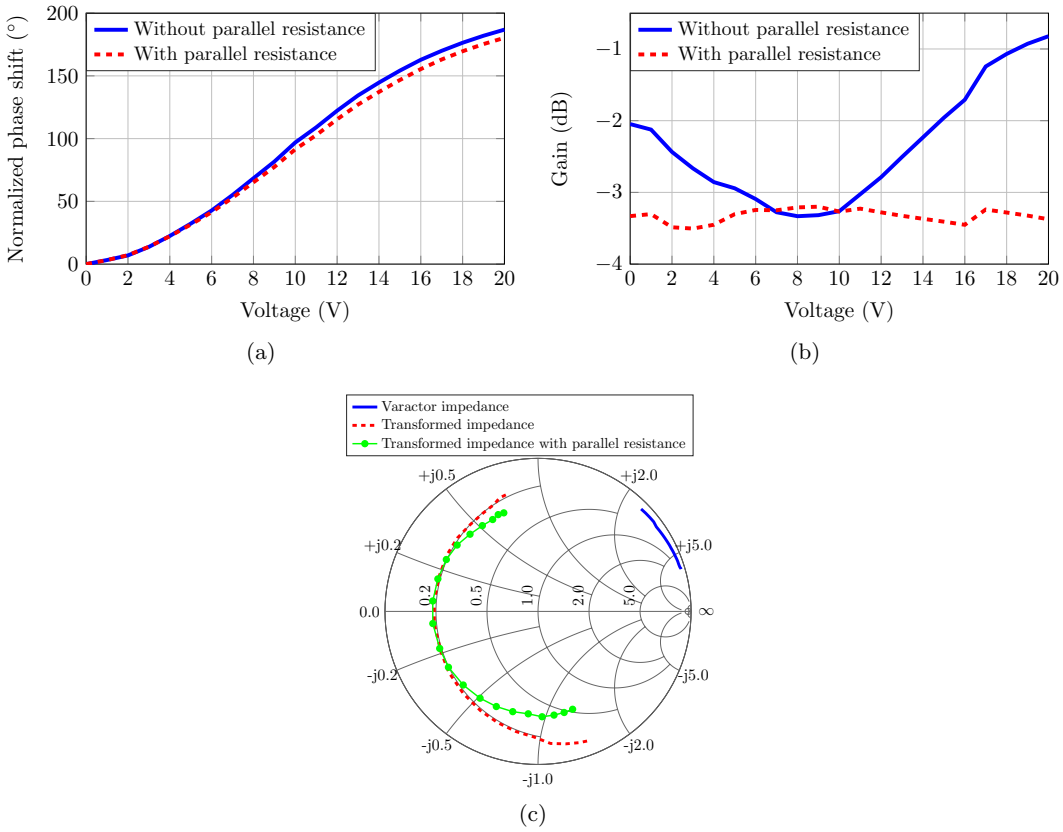


Figure 2.21: Phase shifting response by a transformed diode with and without parallel resistance. (a) Normalized phase shift. (b) Gain. (c) Smith chart representation of Eq. (2.35).

and its phase

$$\angle S_{21\,ps} = -\pi/2 + 2\angle S_{31} + \arctan\left(\frac{\mathrm{Im}(Z_{load})}{\mathrm{Re}(Z_{load}) - Z_{B2}}\right) - \arctan\left(\frac{\mathrm{Im}(Z_{load})}{\mathrm{Re}(Z_{load}) + Z_{B2}}\right). \quad (2.37)$$

From Eq. 2.37, it can be surmised that the imaginary part of the load impedance needs to be 0 at the center biasing port to get the best phase agility. $Z_{B2}$ being close to its real part is a detriment to both the phase –it sends the argument of the arctan to $\infty$– and to its module. The imaginary part being 0 at some point is imperative, and from Eq. 2.36, if $\mathrm{Re}(Z_{load})$ equals $Z_{B2}$, the module of the transmission coefficient would fall down to 0. However, since the real part of the varactor impedance is not big –see Table 2.1– it should not pose a significant problem; but it is, nonetheless, the point at which the biggest loss is produced.

In order to equalize the insertion loss, the transmission coefficient must remain as constant as possible. When the maximum loss is produced, the reactive load impedance is 0. At that biasing point the load impedance is at its lowest, and would barely be affected by a parallel resistance. As the biasing point strays from there, the absolute value of the reactive impedance increases (its sign dependent on the increase or decrease of the bias

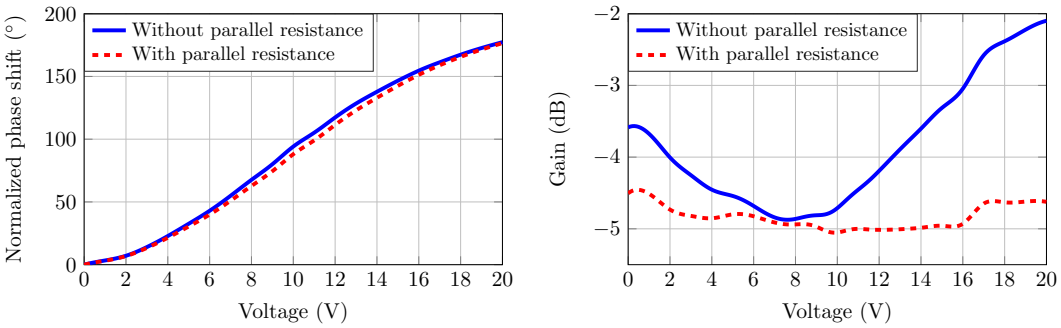


Figure 2.22: Full-wave simulation of the phase shifting response by a transformed diode with and without parallel resistance. (a) Normalized phase shift. (b) Gain.

| **Bias voltage (V)** | 2 | 4 | 6 | 7 | 10 |
|---|---|---|---|---|---|
| **Diode impedance (Ω)** | 3.4257 +11.1447j | 3.4368 +8.0988j | 3.2539 +4.7136j | 3.254 +0.8802j | 3.2983 -3.2699j |
| **Bias voltage (V)** | 12 | 14 | 16 | 18 | 20 |
| **Diode impedance (Ω)** | 3.2409 -7.3475j | 3.2395 -11.7253j | 3.286 -16.3105j | 2.6339 -20.8908j | 2.5961 -25.3451j |

Table 2.9: Impedances of the transformed Aeroflex MGV-125-25-0805-2 diode.

| **Bias voltage (V)** | 2 | 4 | 6 | 7 | 10 |
|---|---|---|---|---|---|
| **Diode impedance (Ω)** | 4.6301 +10.0686j | 4.0111 +7.73759j | 3.3724 +4.3384j | 3.1354 +0.8127j | 3.2859 -3.0114j |
| **Bias voltage (V)** | 12 | 14 | 16 | 18 | 20 |
| **Diode impedance (Ω)** | 3.7091 -6.73401j | 4.6093 -10.6197j | 5.9473 -14.5123j | 7.2027 -18.4040j | 9.1827 -21.7307j |

Table 2.10: Impedances of the transformed Aeroflex MGV-125-25-0805-2 diode with 80 Ω parallel resistance.

voltage) and, since it is at least one order of magnitude higher than the real impedance, it makes the load the more susceptible to an impedance change. That signifies that the real impedance can be increased at the points where the losses are lower. What remains is determining the exact value of the resistance. Too high, and the reactive impedance is masked and no phase shift is achieved. Too low, and the losses remain as before and no equalizing is done. Optimizing it is the solution.

As an example, the diode has been transformed by a line with $Z_2 = 74\,\Omega$ impedance and $L_2 = -48.1416°$ length, resulting in the impedance from Table 2.9. Then, a parallel resistance of $80\,\Omega$ was applied to it, obtaining the impedance values from Table 2.10. With a $Z_{B2} = 17.1251$ and Eq. 2.35, it can be calculated that for the first transformed impedance (Table 2.9), the phase shift is of 186.8° with an insertion loss variation of 2.5 dB. In the case of that impedance with a parallel resistance (Table 2.10), the phase shift is just slightly reduced to 180.3° while the insertion loss ripple is greatly decreased to 0.305 dB. On the other hand, the losses average was increased from 2.36 to 3.32 dB. These

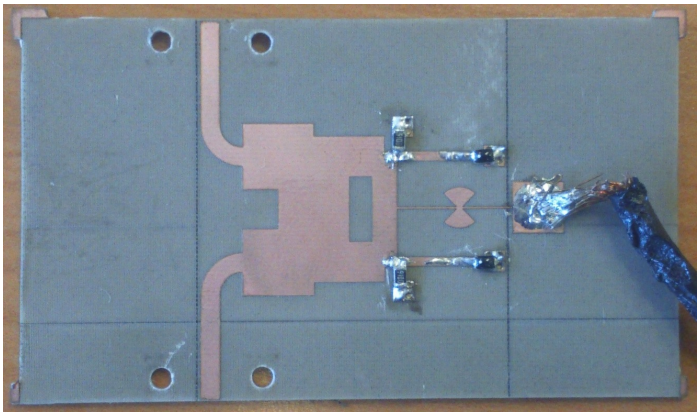

Figure 2.23: Picture of the reflection-type phase shifter based on complex impedance transforming hybrid coupler prototype.

| $W_1$ | $L_1$ | $W_2$ | $L_2$ | $W_3$ | $L_3$ | $W_4$ | $L_4$ | $W_5$ |
|---|---|---|---|---|---|---|---|---|
| 6.8 | 5 | 3.9 | 2.4 | 1.1 | 6.9 | 4.8 | 6.7 | 2.3 |

Table 2.11: Geometry values of the reflection-type phase shifter based on complex impedance transforming hybrid coupler prototype according to Fig. 2.16. All measures in mm.

results are plotted in Fig. 2.21. It is worth mentioning that between the two impedances, the values close to 10 V were the least affected, while the real values close to 0 and 20 V were noticeably increased. There is also a decrease of the value of the reactive impedance in those cases, but as it was proven, their effect on the whole phase agility is very slight.

Following this analysis, a prototype was designed at 9 GHz, using Arlon 25N substrate, of $\epsilon_r = 3.38$, 30 mil thickness and 0.0025 tangent loss. The design procedure was the same as in Fig. 2.15 with the particularity of fixing $L_2$ to the interval of electrical lengths that guarantees the transition of $Z_{load}$ from capacitive to inductive. The results of the optimization are displayed in Fig. 2.22. Disregarding the losses increase due to the substrate, the results are almost identical to those of the ideal transmission lines from Fig. 2.21, and the circuit is always well matched.

A prototype was manufactured, depicted in Fig. 2.23 and with measures from Table 2.11. Two 910 Ω SMD resistors were soldered at the end of the $Z_2$ lines. It was found that at 9 GHz, those particular resistors displayed the most similar behavior to an ideal 80 Ω resistance, even though they still present parasitics. The circuit S-parameters at 9 GHz were measured with and without resistors. They are plotted in Fig. 2.24 and show a good agreement with the S-parameters from the full-wave simulation, but with a loss equalizing not as good, due to the aforementioned resistor parasitics. Still, the phase shifter is well matched at all bias points, and yields 179° with a 1.2 dB loss ripple, improving over the 2.3 dB loss variation that would be achieved without parallel resistances.

The response over a 2 GHz bandwidth is also shown in Fig. 2.24. The return losses are above 10 dB for every biasing voltage from 8.4 to 9.2 GHz, with a phase shift agility

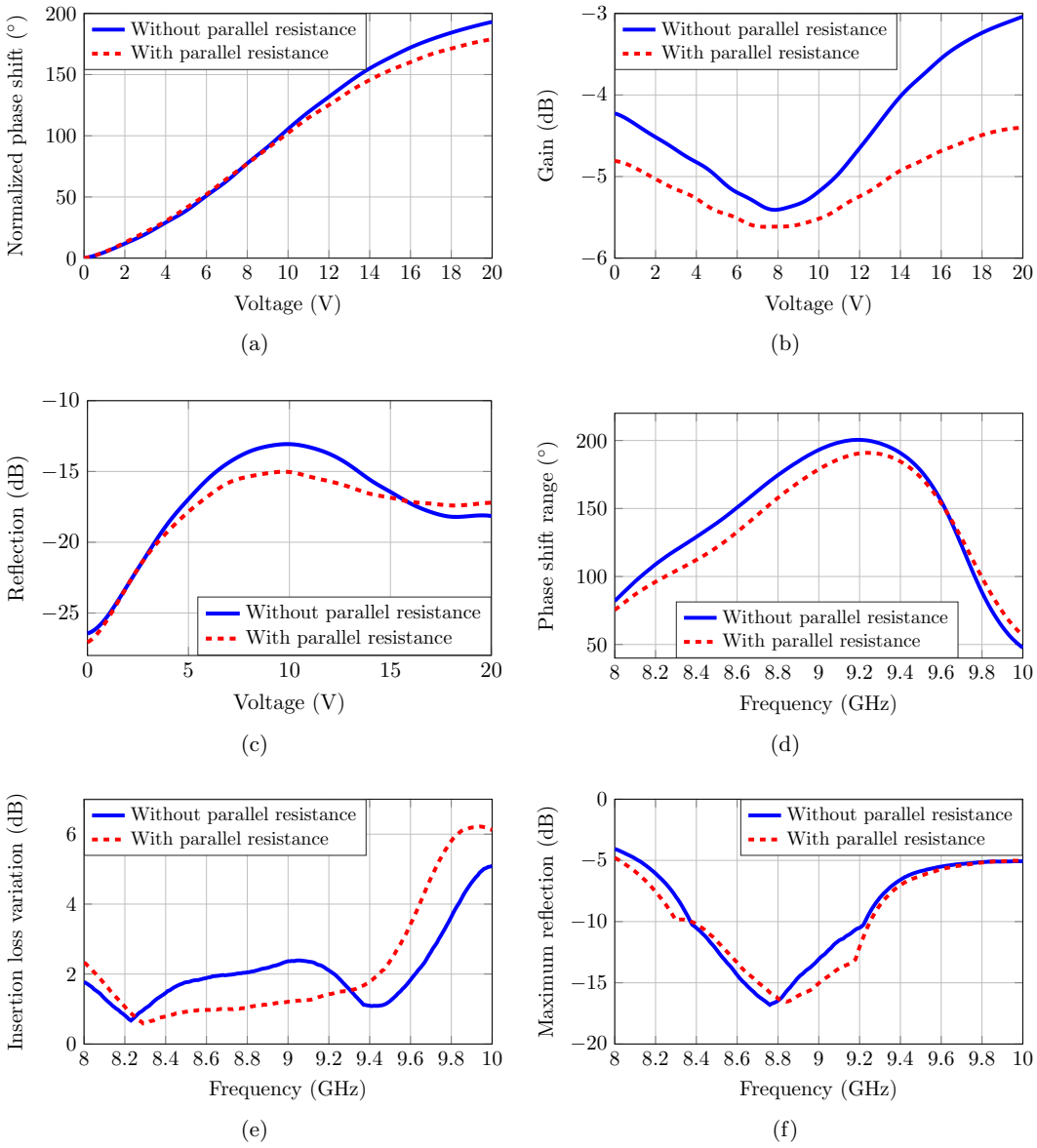


Figure 2.24: Measurements of the reflection-type phase shifter based on complex impedance transforming hybrid coupler prototype. (a) Normalized phase shift. (b) Gain. (c) Matching. (d) Phase shift bandwidth. (e) Insertion loss variation bandwidth. (f) Matching bandwidth.

ranging from 96 to 190°, and an insertion loss ripple below 1.5 dB. The main difference without resistors is that the insertion loss variation is doubled, and the phase agility is slightly bigger.

It is then demonstrated how the insertion loss variation can be equalized with minimal impact to the phase agility, even though the resistor parasitics, which are problematic at X-band due to packaging parasitics, limit how much equalization is possible.

#### 2.4.2.2. Cascading phase shifters

It is usually contemplated that the circuit has to be perfectly matched. However, a minor mismatching can be used to improve the phase shifter performance when cascading it with a duplicate. If an impedance transforming hybrid coupler is designed with a coupling $k$ different than 1, its perfect matching in the $Z_0$ ports can only be assured when the other ports present a $Z_T$ impedance. When every port is reference to $Z_0$, it is found that, for the S-parameters of the hybrid coupler,

$$S_{11} = \frac{|(k^2-1)\,(Z_0 - Z_T)|}{(k^2+1)\,|Z_0 + Z_T^*|}\, e^{j(-\angle S_{33}+2\angle S_{31})}, \tag{2.38}$$

and

$$S_{21} = \frac{2\,|k\,(Z_0\,j - Z_T\,j)|}{(k^2+1)\,|Z_0 + Z_T^*|}\, e^{j(\pi/2-\angle S_{33}+2\angle S_{31})}. \tag{2.39}$$

$S_{43}$ remains 0, and $S_{33}$ is of course still matched to the complex impedance $Z_T$. Due to passive and lossless conditions, it is inferred that

$$S_{41} = \sqrt{\frac{1-|S_{33}|^2}{1+k^2}}\, e^{j(-\pi/2+\angle S_{31})}, \tag{2.40}$$

and due to coupling

$$S_{31} = |S_{41}|\, k\, e^{j\angle S_{31}}. \tag{2.41}$$

Thus, every S-parameter is accounted for. The reflection and transmission coefficients of the reflection-type phase shifter are expressed as

$$S_{11_{ps}} = \frac{1}{k^2+1}\, e^{2j\angle S_{31}} \left( \frac{\rho\,(|S_{33}|^2-1)\,(k^2-1)}{S_{33}\,\rho - 1} + \frac{|S_{33}-1|\,|S_{33}|^2\,|k^2-1|}{|{S_{33}}^*-1|\,S_{33}} \right), \tag{2.42}$$

$$S_{21_{ps}} = \frac{k}{k^2+1}\, 2j\, e^{2j\angle S_{31}} \left( \frac{\rho\,(|S_{33}|^2-1)}{1-S_{33}\,\rho} + \frac{|1-S_{33}|\,|S_{33}|^2}{|1-{S_{33}}^*|\,S_{33}} \right). \tag{2.43}$$

If $k$ does not equal 1, the reflection coefficient is not 0. While the variation and phase range of $S_{21_{ps}}$ are unaffected by it, the loss average increases due to the reflected power, as presented in Fig. 2.25. To a single phase shifter unit, changing the coupling coefficient to something other than 1 is a detriment. However, when it is cascaded to a $Z_0$ transmission line of electrical length $\beta$ and then to another identical phase shifter, the total reflection and transmission coefficients are shown to be

$$S_{11_{cascade}} = S_{11_{ps}} - \frac{S_{11_{ps}}\, S_{21_{ps}}\, e^{(-2j\beta)}}{{S_{11_{ps}}}^2\, e^{(-2j\beta)} - 1}, \tag{2.44}$$

$$S_{21_{cascade}} = -\frac{{S_{21_{ps}}}^2\, e^{(-j\beta)}}{{S_{11_{ps}}}^2\, e^{(-2j\beta)} - 1}, \tag{2.45}$$

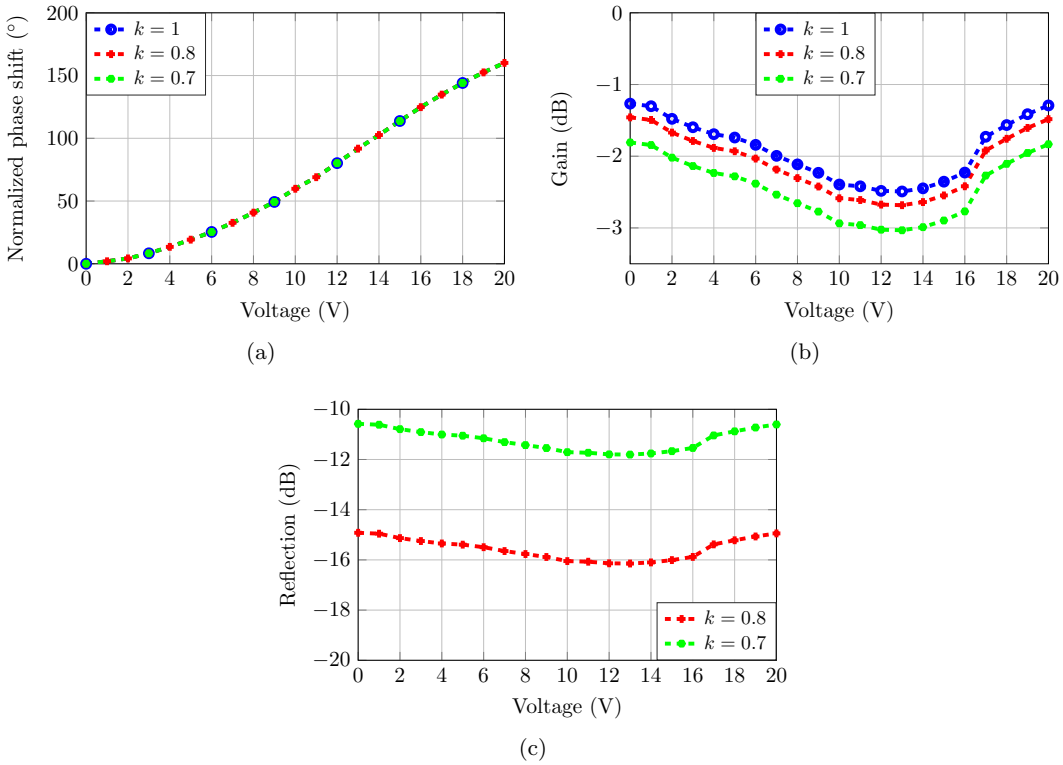


Figure 2.25: Phase shifting response by two cascaded transformed impedance hybrid couplers with $S_{33} = 0.17 - 0.52j$ with different coupling coefficients. Reflection is $-\infty$ dB for $k = 1$. (a) Normalized phase shift. (b) Gain. (c) Reflection.

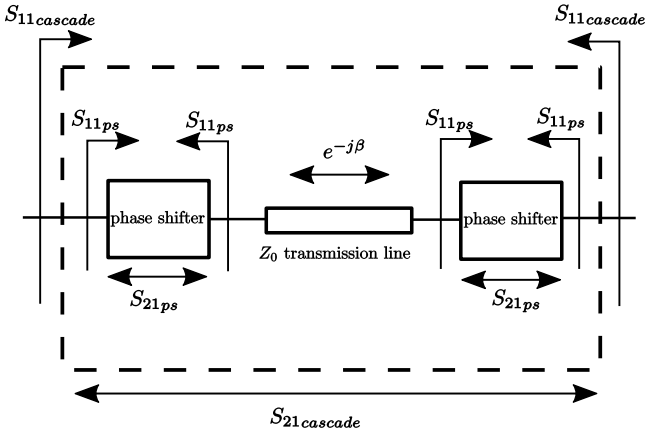


Figure 2.26: Topology of cascaded phase shifters, with intermediate transmission line.

following the topology from Fig. 2.26.

Since $S11_{ps}$ may not be 0, the resulting behavior is defined not only by $S_{33}$ and $\rho$, but also by $k$, $\angle S_{31}$ and $\beta$. Thus, they become design parameters. In a regular ideal hybrid coupler, $\angle S31 = -90°$. Nevertheless, in the impedance transforming hybrid coupler it can be tuned with different values from $L_1$ and $L_2$. $L_2$ is defined by $Z_T$, but if the hybrid is matched to a complex $Z_0$, design freedom is given to $L_1$, allowing further tuning. The design procedure is presented in Fig. 2.28.

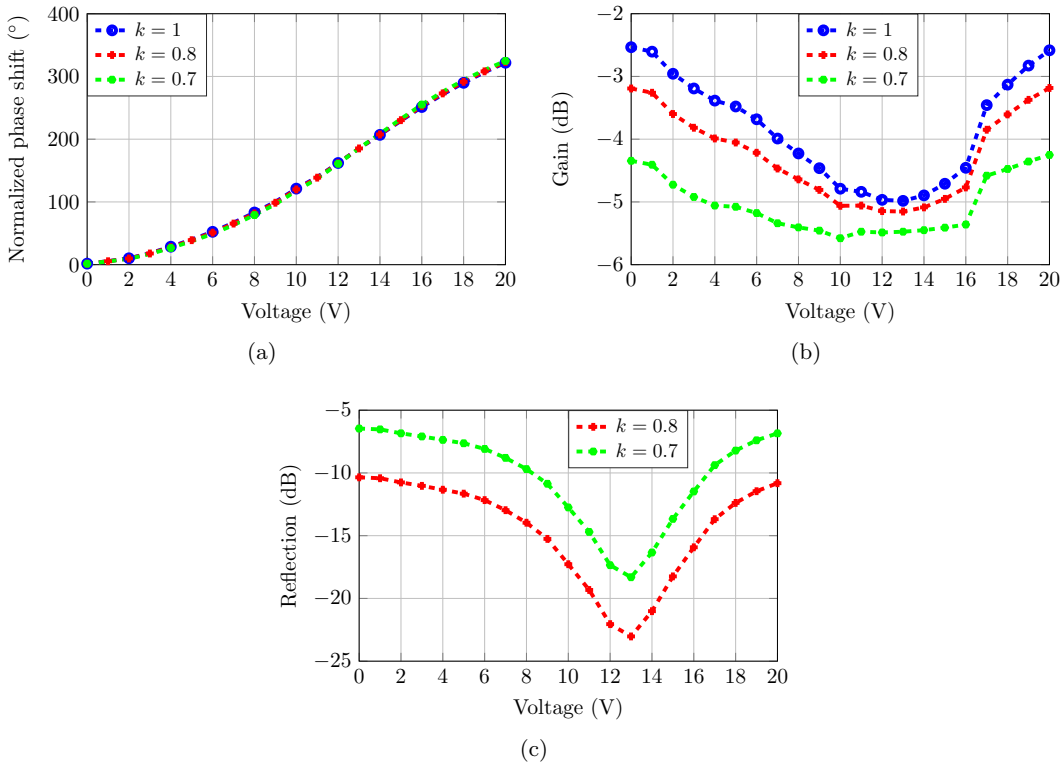


Figure 2.27: Phase shifting response by a transformed impedance hybrid coupler with $S_{33} = 0.17 - 0.52j$ and $\angle S_{31} = 138°$ with different coupling coefficients. Reflection is $-\infty$ dB for $k = 1$. (a) Normalized phase shift. (b) Gain. (c) Reflection.

Presuming that a phase shifter with the varactor from Table 2.1 is designed with $S_{33} = 0.17 - 0.52j$, it yields 160.1° phase agility and 1.25 dB loss ripple. Since it is perfectly matched, cascading it bestows 320.2° phase range and 2.5 dB loss variation. Designing it with $k = 0.8$ and $\angle S_{31} = 138°$ provides the same phase and loss, and with a reflection that gets as high as −14.9 dB. Though it would seem a low reflection, it can still affect the performance when cascaded with another instance of the phase shifter. When connected to an identical phase shifter, it yields 321.4° phase range, 2.02 dB insertion loss ripple and a return losses that do not go below 10.41 dB. A small 0.5 dB reduction of the insertion loss variation is achieved. If matching were not a concern, the improvement could be better by making $k$ stray further from 1. In the same case, if the phase shifters were designed with $k = 0.7$, they would still produce roughly the same phase agility, but with a 1.35 dB insertion loss variation. However, the maximum return loss worsens down to 6.5 dB. The effects of the different couplings are exhibited in Fig. 2.27.

In the end, this method does not work purely for achieving loss equalization because of the mismatching that is produced for significant reduction of insertion loss ripple. Still, it offers a free improvement when two phase shifters needs to be cascaded to achieve a desired phase agility.

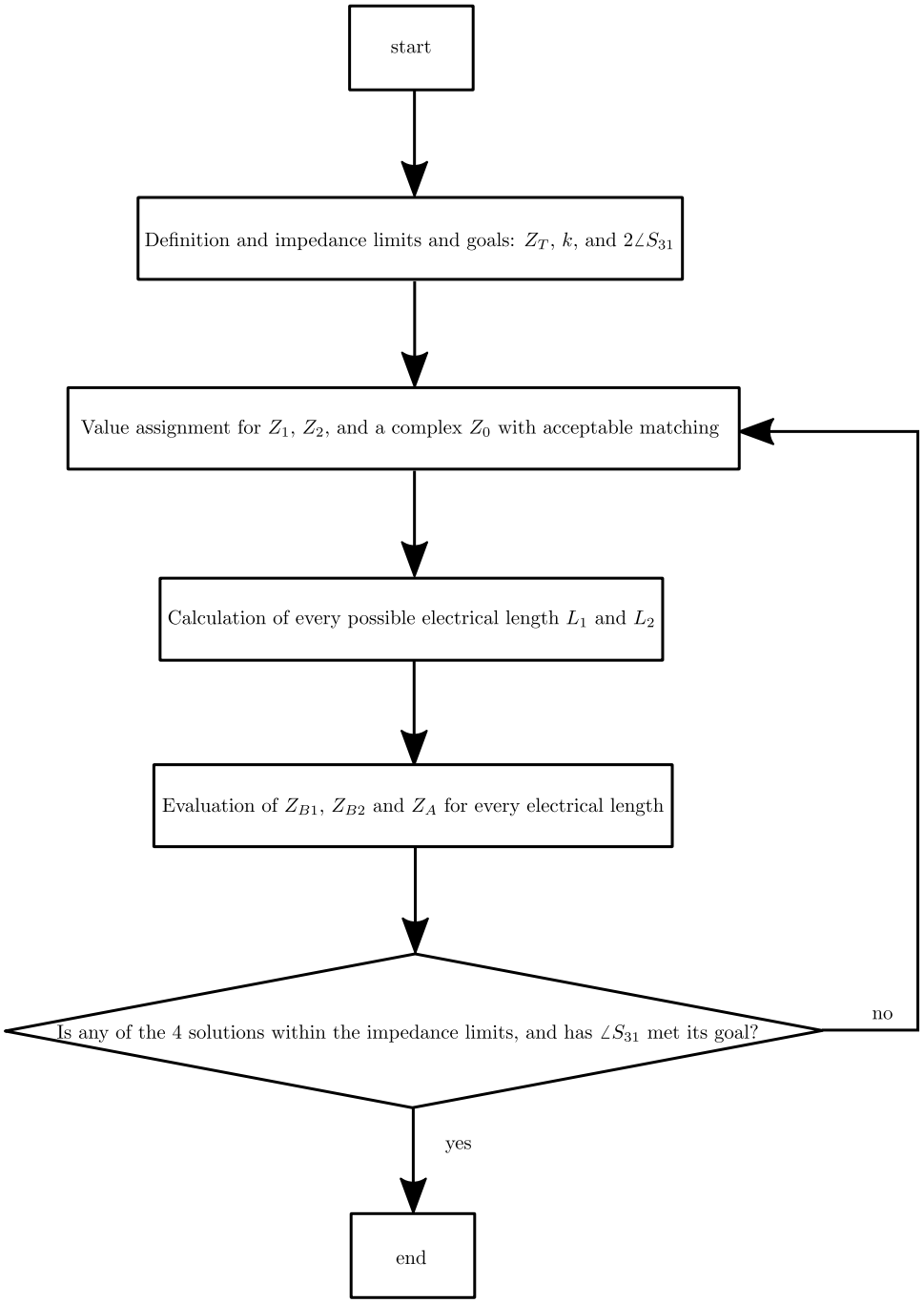


Figure 2.28: Flow chart of the design procedure for a complex impedance transforming hybrid coupler with fixed $2\angle S_{31}$.

## 2.5. Conclusions

In this chapter, an extensive analysis of the reflective-type phase shifter was realized. This type of phase shifters presents interesting characteristics such as zero-power consumption, low cost, and small chip size. Their phase shift is determined by the tunable load, and it can be far from enough. Improving it requires the introduction of LC or impedance

matching networks. These structures do improve the phase shift, but at the expense of an increase of the insertion loss ripple and chip size. The matching points of these network were studied, and choosing it correctly yields a phase agility with reasonable insertion loss trade-off, more than tripling the phase agility of the bare tunable load under study, the varactor diode Aeroflex MGV-125-25-0805-2, whose custom-made model at 9 GHz is utilized in the chapter for every study of phase shifting performance. Even so, introducing matching networks incur a considerable increase in chip size.

To get over the size constraint, the full 4-port analysis of the hybrid coupler and matching network was realized, and a novel equivalent structure was proposed. This structure, called complex impedance transforming hybrid coupler, is capable of fulfilling the role of a hybrid coupler of arbitrary coupling coefficient while matching two different complex impedances in each pair of isolated ports. An even-odd analysis of the circuit –in conjunction with matching, coupling, and isolation conditions– yields expressions that define the values of impedances and electrical lengths. Since there are two undefined impedances, a design procedure was presented to indicate how to tackle the search for a suitable solution. This structure does not only match complex impedances, but it is also capable of matching high values of real impedance avoiding manufacture limitations. Additionally, it was shown how to reduce the transmission line length by compromising theoretical matching without having noticeable mismatching on the final circuit. Three prototypes were manufactured at 2 GHz with excellent agreement between measurements and simulations, proving the validity of the equations and of the design procedure.

The complex impedance transforming hybrid coupler was then used in a reflection-type phase shifter setting. A matching point with good phase agility and low insertion loss ripple was chosen, and then a prototype at 9 GHz was simulated and measured. The measurements show a perfect agreement with simulations in phase agility, and just a slight increase in insertion loss variation, which can be attributed to the tolerance of the varactor capacitance (that is, a small variation of impedance). A phase range of 180.3° with 2.2 dB loss ripple was obtained, with a circuit size 60% smaller than the equivalent normal hybrid coupler with matching networks and still obtaining the same performance. The phase shift range is above 150° from 8.6 to 9.5 GHz, while the insertion loss variation remains under 3 dB from 8 to 9.85 GHz.

While the chip size problem was solved, the insertion loss could still be improved. An alternative study of the complex impedance transforming hybrid coupler was introduced through the view point of the tunable load. By choosing a specific line length that transforms the varactor impedance to another one that transitions from capacitive to inductive (or vice-versa), the hybrid coupler can be seen as a real impedance transformer. That way, new equations were derived that relate the performance of the phase shifter to the transformed impedance and a branch-line impedance from the hybrid coupler. From that expression it was demonstrated how a parallel resistance can equalize the insertion losses by increasing the real impedance of the tunable load at some biasing points. Theoretically, it was shown how the insertion loss ripple could be decreased to 0.3 dB for a 180° phase agility. A prototype was manufactured, achieving the aforementioned phase shift range,

but decreasing the insertion loss variation to only 1.2 dB due to the resistor parasitics. Still, the circuit was shown to have return losses above 10 dB for every biasing voltage from 8.4 to 9.2 GHz, with an insertion loss ripple below 1.5 dB, and a phase agility above 150° from 8.7 to 9.6 GHz.

Another way of equalizing losses was introduced by virtue of designing complex impedance transforming hybrid couplers with coupling coefficients different than 1. When that happens, there is always some mismatching, which worsens the more the coupling coefficient differs from 1. That apparently detrimental behavior can be used to improve the insertion loss when two identical phase shifters are cascaded via a transmission line. It was shown that the phase shift range was doubled, while the insertion loss ripple was not. However, only a 0.5 dB decrease in loss ripple was reported to be achievable for a 320° phase agility if a good overall matching was to be maintained. If matching was not a consideration, a further reduction to 1.35 dB (almost half of what would be obtained with balanced hybrid couplers) is possible. Altogether, it does not offer great equalization with good matching, but it produces a small improvement if two cascaded phase shifters are to be used due to a high phase agility necessity.

In summary, a new impedance transforming hybrid coupler was introduced, heavily optimized towards its utilization in reflection-type phase shifters. Prototypes were manufactured and measured, producing excellent results, and circumventing the chip size limitation which is critical for phased arrays. The insertion losses were equalized through parallel resistors while not affecting the phase agility or the matching. Finally, an improvement of the performance when cascading phase shifters was proposed.

CHAPTER 3

# Guided-wave approach to a tunable reflectarray

## 3.1. Introduction

A reflectarray antenna is a reflector comprised of flat surface array of radiating elements which are illuminated by a feeding antenna. Each element of the array performs a phase correction of the incident wave, resulting in reflected waves which are combined to obtain a specific radiation pattern.

Controlling the resonance of the radiating elements allows to tune the reflected phase. In fixed reflectarrays design, different radiating sizes are used to that effect. For reconfigurability, tunable elements that change the resonance have to be introduced. This method required modelling techniques for analysing the effect of the tunable elements [4], increasing the complexity of the design.

In the guided wave approach, the incident wave is coupled from the radiating element to a transmission line or waveguide, which performs the phase correction through a phase shifter. That way, the radiating and coupling elements can be optimized independently from the transmission lines and phase shifters. Thus, it would be possible to directly introduce already good performing phase shifters into the reflectarray design.

In this chapter, the guided wave approach is used to design a 9 GHz $4 \times 4$ with $0.7\lambda_0$ element spacing fixed reflectarray that produces different beam steering by changing just the layer corresponding to the fixed transmission lines. Thanks to the modular characteristic of the design, the fixed elements can be later replaced by appropriate phase shifters. The element spacing is large enough to guarantee the easy implementation of the phase shifters from Chapter 3, and the low number of elements serves to reduce the numbers of varactors employed, resulting in low manufacture cost.

Later, the analysis of the reflection-type phase shifter from Chapter 2 is resumed to realize a one-port circuit suitable for the reflectarray, ascertaining how much that configuration can improve its performance from what was presented before.

Finally, the design process of the fixed reflectarrays and the optimized varactor-based

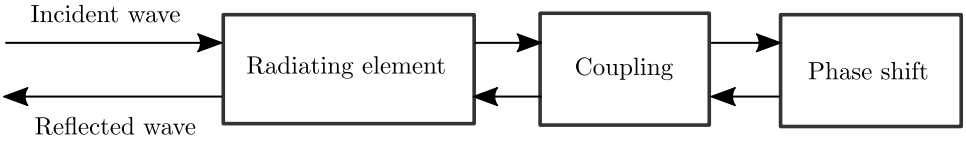


Figure 3.1: Schematic of the unit cell of a guided-wave reflectarray.

phase shifter are combined to realize a $4 \times 4$ beam-forming tunable reflectarray, demonstrating the validity and convenience of the design process.

## 3.2. Fixed guided wave approach

### 3.2.1. Structure

The unit cell is the basic element of the reflectarray. In the guide-wave approach, it consists of a radiating element which is connected to a transmission line. The incident wave impinges on the radiating element, and it is coupled to the transmission line or waveguide where the phase shift is produced. Then, the corrected signal is coupled back to the radiating element, producing the reflected wave, as shown in Fig. 3.1. It is necessary to produce a good matching to the phase shift element, since the incident wave that is not coupled will be reflected without the proper phase correction, producing specular radiation.

A rectangular patch fed by a microstrip transmission line through a slot etched on its ground plane is a well-known antenna structure [65]. Based on that design, if the transmission line is left open-ended it will act as a stub. The incident wave, coupled through a slot etched in the ground plane, propagates through the transmission line, gets reflected at the open circuit end and travels back through the same coupling slot to the patch antenna. A 360° phase agility is achieved by virtue of changing the line length. Even if it results in a length bigger than the unit cell size (due to a necessary spacing between elements), the line can be bent to still achieve the full phase range. A diagram of the configuration is shown in Fig. 3.2.

### 3.2.2. Unit cell matching

#### 3.2.2.1. Periodicity simulation

Since the unit cell is not an isolated antenna, the rest of the elements present in the reflectarray must be taken into consideration. Using Floquet modes, it is possible to realize an analysis of an infinite array [66] using the unit cell. To facilitate this process, the finite element method commercial software Ansys High Frequency Structure Simulator (HFSS) [67] was utilized, which allows to use Floquet ports in periodically planar structures and has been validated experimentally for modeling reflectarrays [68, 69]. The array element is enveloped in a vacuum box of the same measurements as the array plane that acts as a periodicity boundary. A Floquet port is added at the top of the box, representing the plane wave impinging on the radiating element, which is de-embedded to the radiating

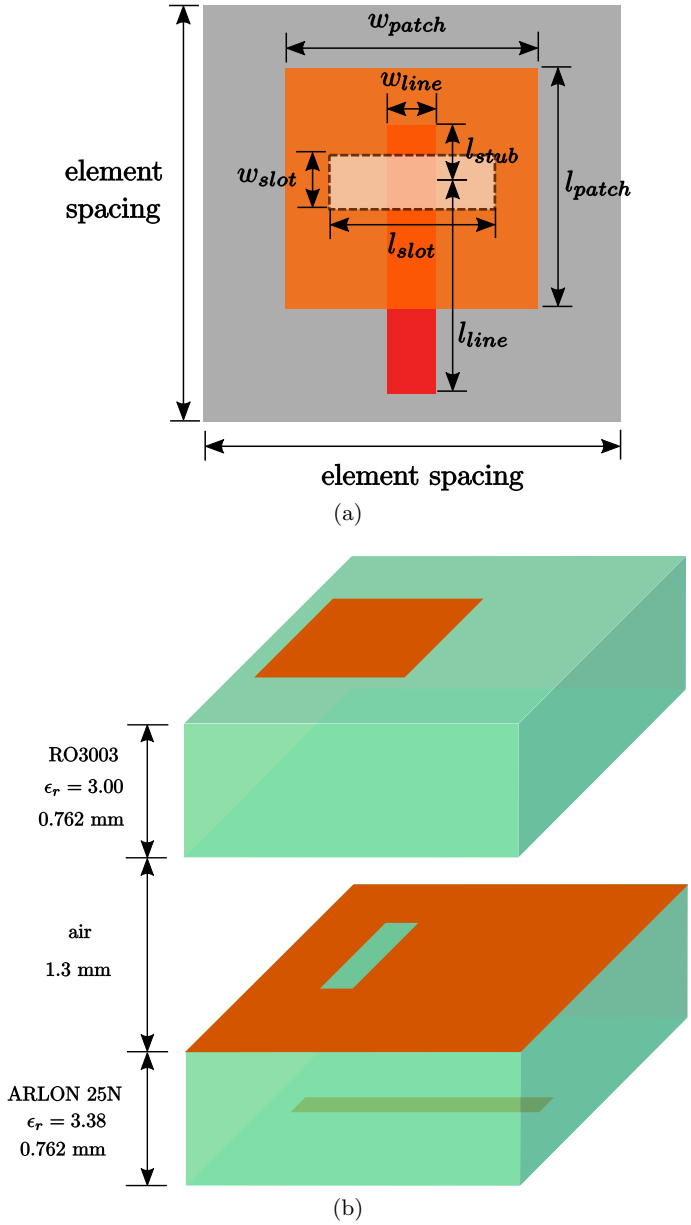


Figure 3.2: Reflectarray cell design with fixed transmission line. (a) Top view. (b) Oblique perspective vertically exaggerated.

element. A lumped microstrip port is added at the end of the transmission line to check matching and transmission.

The Floquet port is set to excite the Floquet modal fields $TE_{00}$ and $TM_{00}$, which are conventional plane waves and correspond for normal incidence, as in the example from Fig. 3.3, to fields of $y$ and $x$ polarization respectively, propagating directly from the feed to the center of the array element.

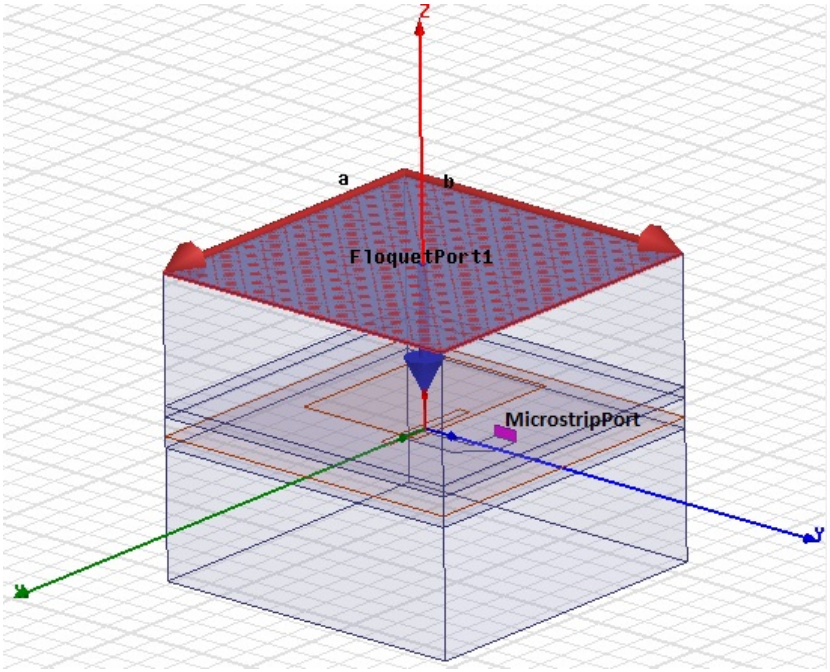


Figure 3.3: Example of a Floquet analysis set-up with HFSS.

Therefore, the problem is reduced to analysing the scattering parameters of a 3-ports network, such as:

$$[S_{cell}] = \begin{bmatrix} S_{\mathrm{TE}_{00},\mathrm{TE}_{00}} & S_{\mathrm{TE}_{00},\mathrm{TM}_{00}} & S_{\mathrm{TE}_{00},\mathrm{mstrip}} \\ S_{\mathrm{TM}_{00},\mathrm{TE}_{00}} & S_{\mathrm{TM}_{00},\mathrm{TM}_{00}} & S_{\mathrm{TM}_{00},\mathrm{mstrip}} \\ S_{\mathrm{mstrip},\mathrm{TE}_{00}} & S_{\mathrm{mstrip},\mathrm{TM}_{00}} & S_{\mathrm{mstrip},\mathrm{mstrip}} \end{bmatrix}, \tag{3.1}$$

where the S-parameters with same suffixes correspond to the reflection coefficients of the different modes, and S-parameters with different suffixes correspond to transmission coefficients between the indicated modes.

In the proposed unit cell, linear polarization is employed, and so, one of the modes is employed as co-polar mode. If matching were perfect, the reflection coefficient of said mode would be 0, and so would be the reflection coefficient at the transmission line, with the transmission between them being 1. The cross-polar field should be completely reflected (no coupling produced), with no transmission to the other mode and the transmission line. In regards to Eq. 3.1, and assuming $TE_{00}$ as the Floquet mode to match, the absolute values of the S-parameters matrix would end as it follows:

| $w_{patch}$ | $l_{patch}$ | $w_{slot}$ | $l_{slot}$ | $w_{line}$ | $l_{stub}$ |
|---|---|---|---|---|---|
| 12.5 | 9.43 | 0.8 | 7.62 | 1.76 | 1.36 |

Table 3.1: Geometry values of the designed reflectarray unit cell. All measures in mm.

$$[|S_{cell}|] = \begin{bmatrix} 0 & 0 & 1 \\ 0 & 1 & 0 \\ 1 & 0 & 0 \end{bmatrix}. \tag{3.2}$$

Taking Eq. 3.2 as a goal, the geometry values of the cell from Fig. 3.2 should be optimized to obtain S-parameters as close as possible.

After ensuring proper matching and transmission, the lumped microstrip port may be removed, and a two-port network is obtained, with just the S-parameters corresponding to $TE_{00}$ and $TM_{00}$, in which the reflected phase of the co-polar mode is corrected by tuning the transmission line length. This way, a unit cell was designed at 9 GHz with an element spacing of $0.7\lambda_0$. The Rogers 3003 substrate of $\epsilon_r = 3$ and thickness of 30 mil was used for the patch antenna, and the Arlon 25N substrate of $\epsilon_r = 3.38$ and thickness of 30 mil was used for the microstrip transmission line, with a separation between substrates of 1.3 mm to improve bandwidth. The geometry parameters are shown in Table 3.1.

#### 3.2.2.2. Incidence angles

In fixed reflectarrays, the phase of the electromagnetic wave reflected by the unit cell is altered by the incidence angle of the impinging wave [70]. Accordingly, the matching could be affected in a similar way.

The matching analysis was realized presuming a normal incidence angle, i.e., the incident wave propagates perpendicularly to the array plane. However, the propagation direction of the incident wave $\vec{k}_i$ changes for each array element, as illustrated in Fig. 3.4. Defining the position vector of the phase center of the feed as $\vec{r}_f = x_f\,\hat{x} + y_f\,\hat{y} + z_f\,\hat{z}$, and the position vector of the $i$ element of the array as $\vec{r}_i = x_i\,\hat{x} + y_i\,\hat{y} + z_f\,\hat{z}$, it is found that the incidence angles in $\theta$ and $\varphi$ of the wave against the array elements plane can be expressed as:

$$\theta_{inc} = \arctan\left(\frac{\sqrt{|x_f - x_i|^2 + |y_f - y_i|^2}}{z_f}\right), \tag{3.3}$$

$$\varphi_{inc} = \arctan\left(\frac{y_i - y_f}{x_i - x_f}\right). \tag{3.4}$$

With this realization, it is possible to simulate more accurately the behavior of the reflectarray by introducing in the Floquet mode analysis the correct incidence angles.

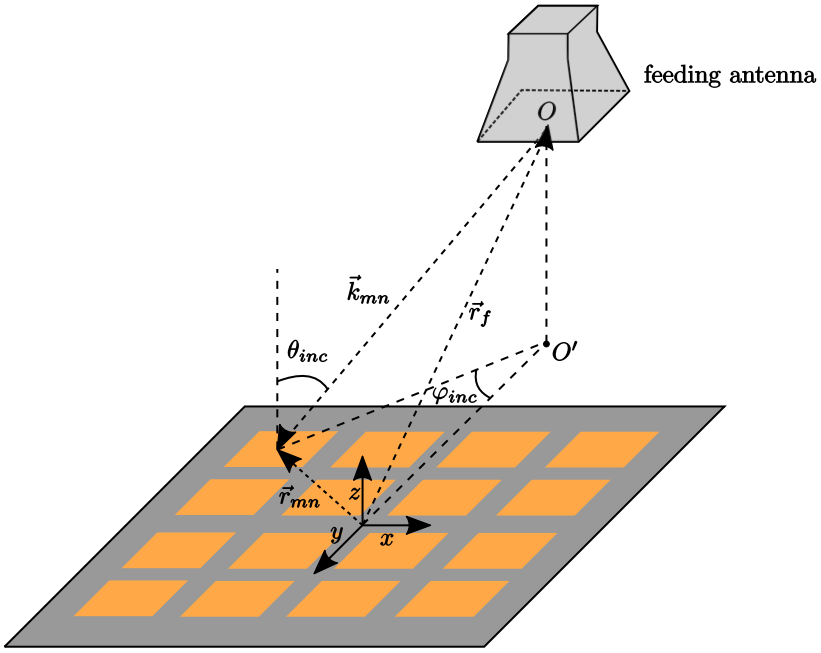


Figure 3.4: Diagram of the incident angles of the illuminated array. $O'$ is the projection of the feed phase center onto the array plane.

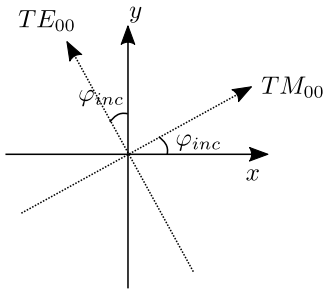


Figure 3.5: Representation of dominant Floquet modes direction for a $\hat{\varphi}$ polarized wave.

Since the field is $\hat{\varphi}$ polarized, the $\theta$ incidence angle does not produce a redefinition of the dominant Floquet modes, while the angle $\varphi_{inc}$ must be considered, due to the equivalences $\widehat{\mathrm{TE}}_{00} = -\sin(\varphi_{inc})\,\hat{x} + \cos(\varphi_{inc})\,\hat{y}$ and $\widehat{\mathrm{TM}}_{00} = \cos(\varphi_{inc})\,\hat{x} + \sin(\varphi_{inc})\,\hat{y}$, visually displayed in Fig. 3.5.

In the interest of expressing the scattering parameters matrix for typical linear polarizations $\hat{x}$ and $\hat{y}$, such as

$$[S_{cell}] = \begin{bmatrix} S_{yy} & S_{yx} & S_{y,\mathrm{mstrip}} \\ S_{xy} & S_{xx} & S_{x,\mathrm{mstrip}} \\ S_{\mathrm{mstrip},y} & S_{\mathrm{mstrip},x} & S_{\mathrm{mstrip,mstrip}} \end{bmatrix}, \tag{3.5}$$

a rotation matrix is applied to the S-parameters from Eq. (3.1). Thus, and simplifying

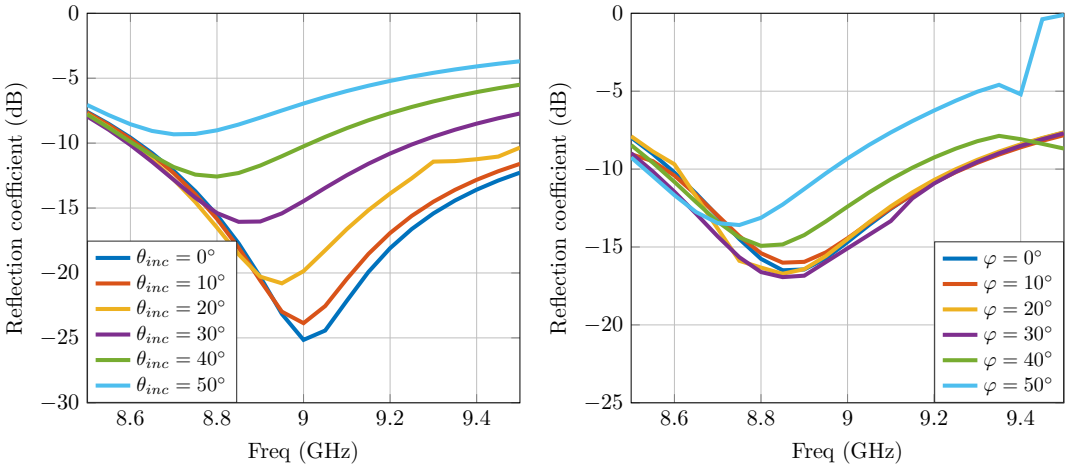


Figure 3.6: Reflection coefficient of the reflectarray cell for different incidence angles. (a) Sweep of $\theta_{inc}$ for $\varphi_{inc} = 0°$. (b) Sweep of $\varphi_{inc}$ for $\theta_{inc} = 30°$.

due to reciprocity ($S_{xy} = S_{yx}$, $S_{\mathrm{TE}_{00},\mathrm{TM}_{00}} = S_{\mathrm{TM}_{00},\mathrm{TE}_{00}}$), it is obtained that

$$S_{\mathrm{mstrip},y} = S_{\mathrm{mstrip},\mathrm{TE}_{00}} \cos(\varphi_{inc}) - S_{\mathrm{mstrip},\mathrm{TM}_{00}} \sin(\varphi_{inc}), \tag{3.6a}$$

$$S_{y,\mathrm{mstrip}} = S_{\mathrm{TE}_{00},\mathrm{mstrip}} \cos(\varphi_{inc}) - S_{\mathrm{TM}_{00},\mathrm{mstrip}} \sin(\varphi_{inc}), \tag{3.6b}$$

$$S_{\mathrm{mstrip},x} = S_{\mathrm{mstrip},\mathrm{TM}_{00}} \cos(\varphi_{inc}) + S_{\mathrm{mstrip},\mathrm{TE}_{00}} \sin(\varphi_{inc}), \tag{3.6c}$$

$$S_{x,\mathrm{mstrip}} = S_{\mathrm{TM}_{00},\mathrm{mstrip}} \cos(\varphi_{inc}) + S_{\mathrm{TE}_{00},\mathrm{mstrip}} \sin(\varphi_{inc}), \tag{3.6d}$$

$$S_{yy} = S_{\mathrm{TE}_{00},\mathrm{TE}_{00}} \cos(\varphi_{inc})^2 + S_{\mathrm{TM}_{00},\mathrm{TM}_{00}} \sin(\varphi_{inc})^2 - 2\, S_{\mathrm{TE}_{00},\mathrm{TM}_{00}} \cos(\varphi_{inc}) \sin(\varphi_{inc}), \tag{3.6e}$$

$$S_{xx} = S_{\mathrm{TM}_{00},\mathrm{TM}_{00}} \cos(\varphi_{inc})^2 + S_{\mathrm{TE}_{00},\mathrm{TE}_{00}} \sin(\varphi_{inc})^2 + 2\, S_{\mathrm{TE}_{00},\mathrm{TM}_{00}} \cos(\varphi_{inc}) \sin(\varphi_{inc}), \tag{3.6f}$$

$$S_{xy} = (S_{\mathrm{TE}_{00},\mathrm{TE00}} - S_{\mathrm{TM}_{00},\mathrm{TM}_{00}}) \cos(\varphi_{inc}) \sin(\varphi_{inc}) + S_{\mathrm{TM}_{00},\mathrm{TE}_{00}} \left(\cos(\varphi_{inc})^2 - \sin(\varphi_{inc})^2\right), \tag{3.6g}$$

while $S_{\mathrm{mstrip},\mathrm{mstrip}}$ remains the same, as it is not dependent on the Floquet modes rotation.

Evaluating the matching for different incidence angles in the unit cell previously designed at normal incidence, it is observed that the matching deteriorates as the incidence angle strays from 0°, both in $\theta$ and $\varphi$. The simulations results are plotted in Fig. 3.6.

For $\theta_{inc}$ above 40° and for $\varphi_{inc}$ above 50°, there is noticeable mismatching, and the bandwidth progessively decreases. It is capital, then, to take into consideration the incidence angles when designing the unit cell. Its parameters may have to change at certain

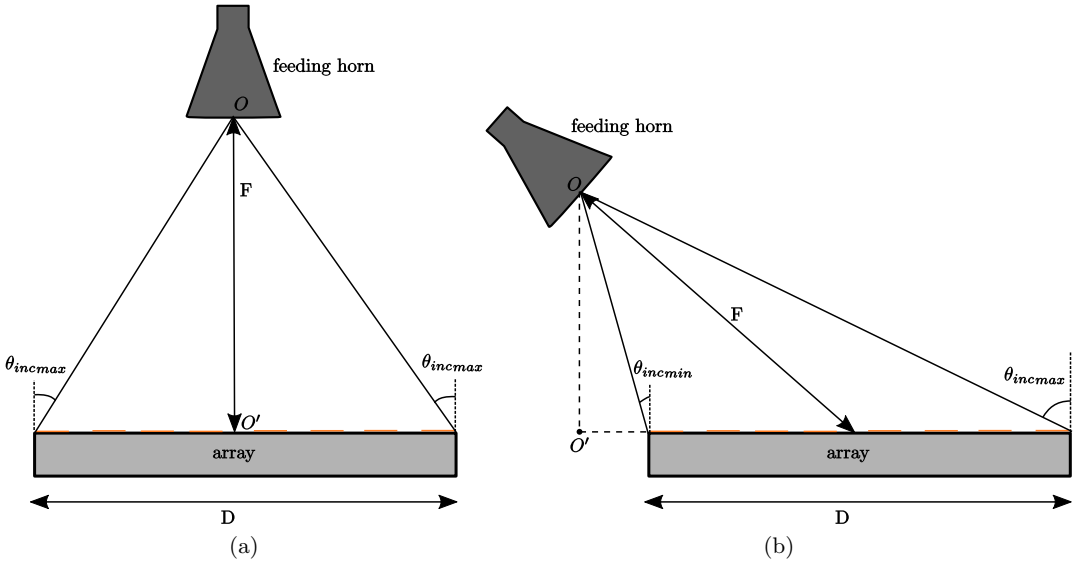


Figure 3.7: Diagrams of two different feeding antenna positions with same focal distance. (a) Centered. (b) Offset.

positions to achieve good matching. This could be specially challenging if there is a big variation in incidence angles, which will be affected by the position of the feeding antenna and the size of the reflectarray.

The feeding antenna of a reflectarray may be centered –pointing perpendicularly at the array– or offset, illuminating the array at an angle and thus avoiding blockage from the feed in broadside radiation. In any case, the smaller the focal distance (F) to array aperture diameter (D) ratio, the smaller range of incidence angles there will be. Nevertheless, this might be at odds with the illumination efficiency (only part of the reflectarray might be illuminated). Furthermore, in the case of an offset feed, it is aggravated: there might be no normal incidence, and the array elements from the furthest edge will receive a plane wave with higher $\theta$ incidence angles. On the other hand, it reduces the variation of the $\varphi$ incidence angle. These occurrences can be intuitively understood with the drawings from Fig. 3.4 and Fig. 3.7.

### 3.2.3. Phase shift for beam steering

From phased array theory, it is well known that to point a beam to a specific direction, $\theta_b$ and $\varphi_b$, the phase distribution on the surface, $\phi_b$, must meet that [66]:

$$\phi_b(x_i, y_i) = -k_0 \left(x_i \cos\left(\varphi_b\right) + y_i \sin\left(\varphi_b\right)\right) \sin\left(\theta_b\right), \tag{3.7}$$

where $k_0$ is the propagation constant in the vacuum and $x_i$ and $y_i$ are the coordinates of the $i$ element of the array. In the reflectarray, the final phase distribution is the sum of the incident phase and the phase shift produced at the element, so that

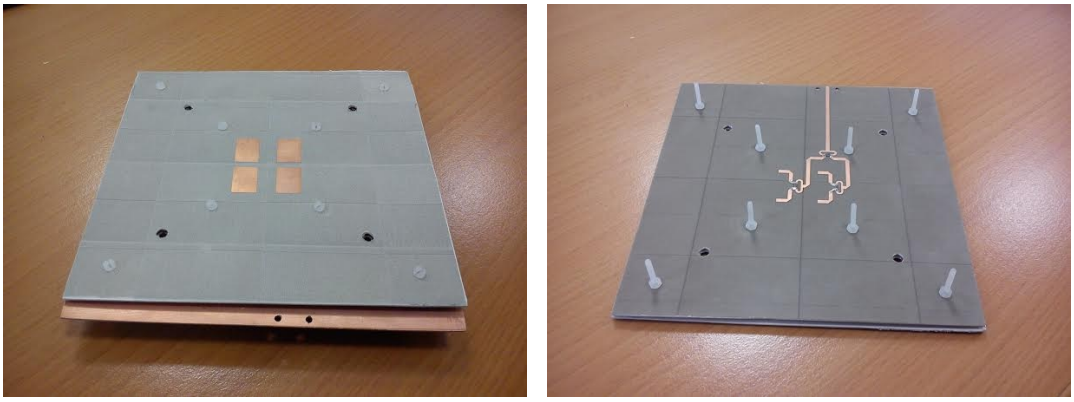

(a) (b)

Figure 3.8: Picture of the $2 \times 2$ elements antenna feed. (a) Radiating elements. (b) Distribution circuit.

$$\phi_b(x_i, y_i) = \phi_{inc}(x_i, y_i) + \phi_{ps}(x_i, y_i), \tag{3.8}$$

where $\phi_{inc}(x_i, y_i)$ is the phase of the incident wave propagating from the feed to the $i$ element of the reflectarray, and $\phi_{ps}(x_i, y_i)$ is the phase correction performed by that element. Isolating the phase shift distribution and applying Eq. (3.7):

$$\phi_{ps} = k_0 \left(d_i - (x_i \cos(\varphi_b) + (y_i \sin(\varphi_b)) \sin(\theta_b) + 2\,\pi\,N, \right. \tag{3.9}$$

where $d_i$ is the distance from the phase center of the feed to the $i$ element, and N = 0,1,2,...

If the reflectarray element is properly matched for every position, the phase shift produced at each element will depend solely on the length of the transmission line. Thus, using Eq. (3.9), the electrical length of the transmission line at each cell is calculated.

To ensure adequate phase control, each individual cell should be simulated using Floquet analysis, and a fine tuning of the line length must be performed.

### 3.2.4. Measurements

Since the purpose of this Thesis is to demonstrate reconfigurability capabilities, and not developing high gain antennas, reflectarrays with small numbers of elements are utilized. Henceforth, there is no attention paid to spill-over or illuminating efficiency, and a simple implementation is preferred. In order to reduce the size of the structure needed to support the reflectarray, a small $2 \times 2$ array antenna is used as feed. Its location has to be far enough to guarantee far-field radiation and low incident angles.

For a $4 \times 4$ reflectarray with $0.7\lambda_0$ element spacing at 9 GHz, it was decided to place the feed in the coordinates $x = -100$ mm, $y = 0$ and $z = 200$ mm, considering the center of the reflectarray surface as origin. In this configuration, the maximum $\theta_{inc}$ is 34.89°, and

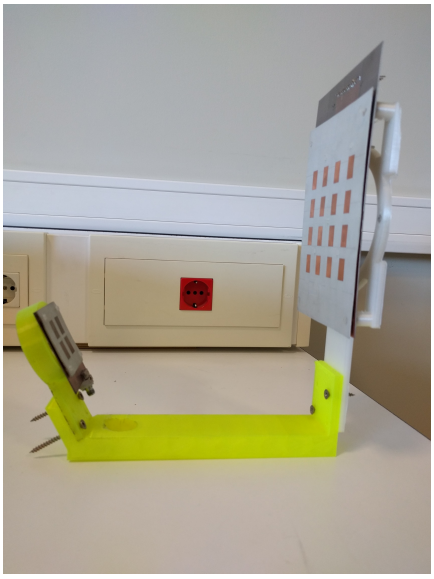

Figure 3.9: Picture of the support for reflectarray antenna and feed.

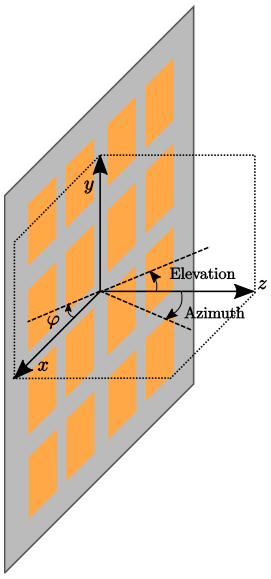


Figure 3.10: Representation of the azimuth and elevation planes and angles.

the maximum $\varphi_{inc}$ is 28.3°. According to Fig. 3.6, decent matching is to be expected. A structure was 3D printed to hold the array and place the feed at the appropriate location, tilting it as to point at the center of the array. The feed was orientated to radiate with the same polarization as the reflectarray.

The array element spacing and number of elements were chosen to facilitate the later implementation of a reconfigurable phase shifter. The element spacing should be big enough to house the circuit according to the chip size of the phase shifters discussed in Chapter 2, and the $4 \times 4$ number of elements allows to keep the number of varactors, and so the manufacture cost, low. As a result, the measurement of the fixed reflectarray will elucidate how such a small reflectarray size affects the radiation pattern.

The measurement set-up of the anechoic chamber available to the author can perform sweeps in the azimuth and elevation planes (corresponding to $xz$ and $yz$ plane respectively, as seen in Fig. 3.10). Given an antenna with $\hat{y}$ polarity, the azimuth plane corresponds to the H-plane, and the elevation one to the E-plane. For simplicity's sake, the beam steering will only be realized to solutions pointing to different $\theta$ angles in one of those planes, equating to $\varphi = 0°$ and $\varphi = 90°$ plane cuts.

Following Eq. (3.9) and through fine tuning with Floquet mode analysis, two reflectarrays were designed: one with a main beam pointing to broadside and the other pointing to $\theta = 45°$, $\varphi = 0°$ (azimuth=45°). Their layouts are shown in Fig. 3.11, maintaining the array geometry except for the length of the transmission lines.

The full reflectarray and feed configuration was simulated using HFSS, and compared to an equivalent ideal phased array of patch antennas with same element spacing and pointing to the same direction. As observed in Fig. 3.12, the main beam is almost exactly the same, and the side lobes –and grating lobe in the 45° reflectarray– are roughly in the same positions, but with an increase of the variation of the secondary lobes level,

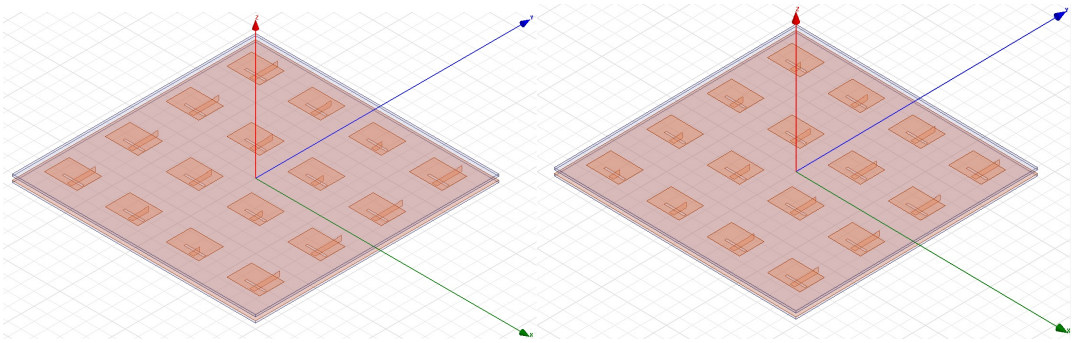

(a) (b)

Figure 3.11: Layouts of the two fixed reflectarrays. (a) Pointing to broadside. (b) Pointing to $\theta = 45°$.

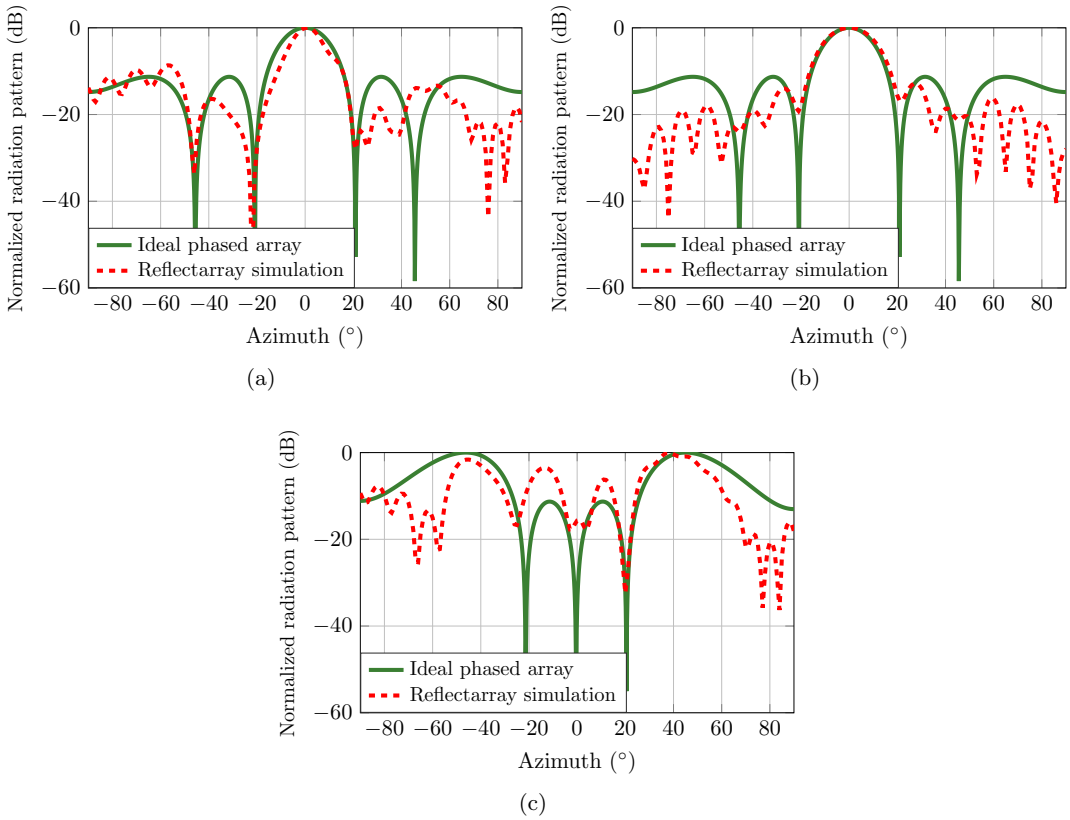


Figure 3.12: Comparison of radiation patterns at 9 GHz comparison between ideal phased arrays and simulated reflectarray configurations. (a) Broadside array H-plane. (b) Broadside array E-plane. (b) 45° array H-plane.

consequence of the diffraction produced by the small antenna aperture and small spill-over efficiency, which is especially noticeable in reflectarrays with small aperture size [71].

The reflectarrays were manufactured, using nylon screws and washers to properly fasten the two layers while keeping a 1.3 mm separation between them. The antennas were measured in an anechoic chamber, bestowing the data from Fig. 3.13. It is observed

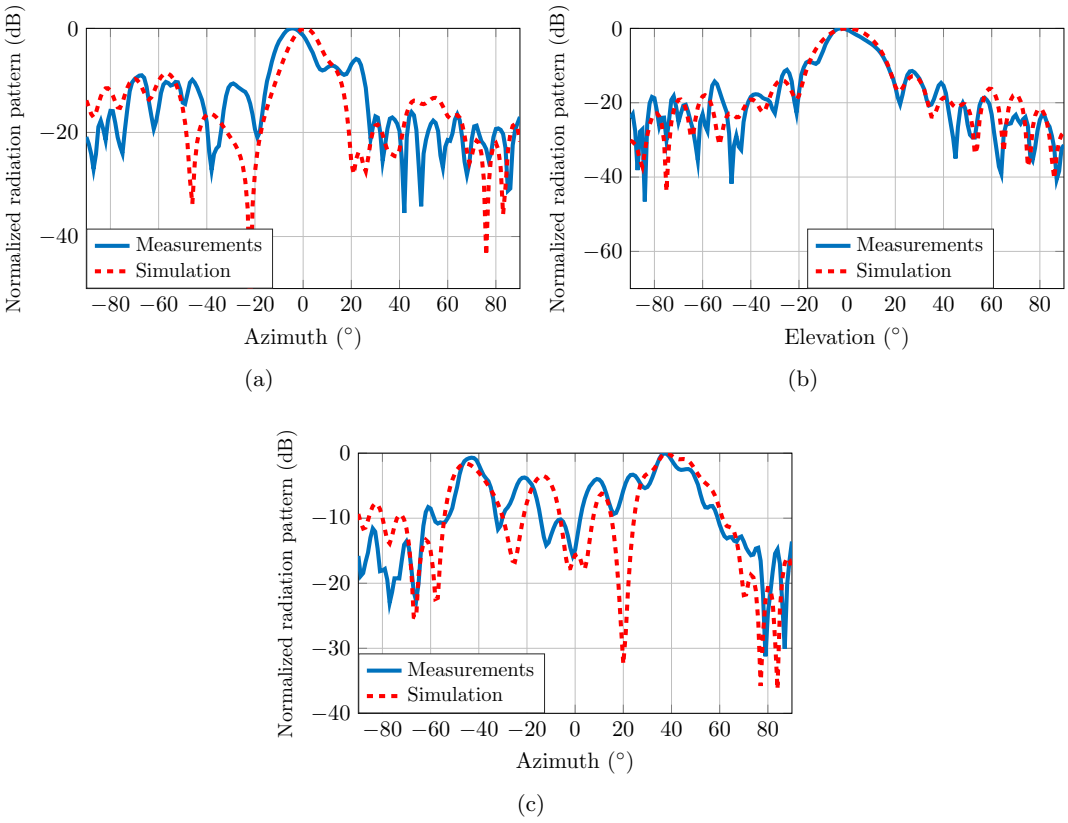


Figure 3.13: Comparison of radiation patterns at 9 GHz between simulated and measured reflectarrays. (a) Broadside array H-plane. (b) Broadside array E-plane. (b) 45° array H-plane.

that the diffraction has had a bigger impact that in simulations, producing variation on the levels of main and side lobes. Still, the similitudes between the simulated and measured fields are evident, and the main beam pointing direction is recognizable. There is also an increase in the specular reflection (around 25°), which can be attributed to the presence of other elements, namely the mechanical metal post to which the reflectarray was screwed. This specular reflection is particularly noticeable in low gain reflectarrays [71]. The measurements could be improved if an absorbent was placed at the edges of the reflectarray, decreasing diffraction and hence, obtaining a radiation pattern closer to that of the ideal phased array. Nevertheless, the experimental results show that the discussed design procedure is valid for manufacturing guided-wave reflectarrays, and the radiated field is marred only by the small array size.

## 3.3. Phase shifter element

The phase shifters discussed in Chapter 2 were two-port networks. In a reflectarray in which the same polarization is re-radiated, the phase shifter becomes a one-port network, such as the open-ended stub of the studied fixed reflectarray. It is necessary to assess how this change affects the reflection-type phase shifter performance.

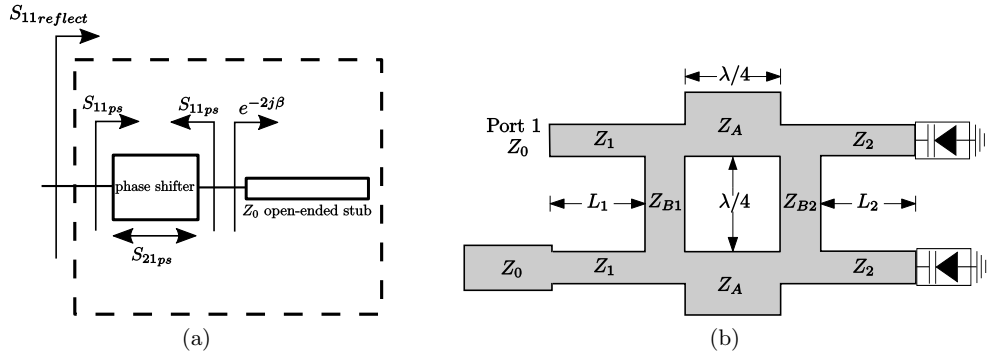


Figure 3.14: (a) Network schematic of reflecting RTPS. (b) Topology of reflecting RTPS.

### 3.3.1. One-port RTPS

It can be assumed that if one of the ports of the RTPS is left open-ended, as in the topology of Fig. 3.14, the signal at the output port is reflected back into the phase shifter, exiting through the input port and therefore acting as two cascaded phase shifters.

By performing a scattering parameters analysis of the cascaded networks as shown in the schematic, the reflection at the port is defined as

$$S_{11reflect} = S_{11ps} + \frac{{S_{21ps}}^2}{e^{2j\beta} - S_{11ps}}, \tag{3.10}$$

where $S_{11ps}$ is the reflection coefficient of a single RTPS from Eq. (2.42), $S_{21ps}$ is the transmission coefficient from Eq. (2.43), and $\beta$ is the electrical length of an open-ended stub that can be used for fine tuning.

Although similar, Eq. (3.10) differs from the phase shift response of two cascaded phase shifters from Eq. (2.45), depending also on its reflection coefficient. Thus, it stands to reason that the phase shifter behavior could be altered, while still depending on the same parameters of the impedance transforming hybrid coupler such as the transforming impedance reflection $S_{33}$, the transmission phase $\angle S_{31}$ and the coupling coefficient $k$. Moreover, the matching restriction which limited the improvement of cascaded phase shifters can now be overcome, since the signal is reflected at the input port anyway. As a result, it could be possible to achieve a greater equalization of insertion loss through omitting the matching restraint in the design process.

The differences in performance can be illustrated with a practical example: Assuming an impedance transforming hybrid coupler with the parameters $S_{33} = 0.15 - 0.57j$, $\angle S_{31} = 47.54°$ and $k = 1.09$, and with the varactor from Table 2.1 as tunable load, a phase shifter is obtained with 174.57° phase agility and 1.72 dB insertion ripple, while maintaining matching with return losses well over 10 dB. If cascaded, the phase agility more than doubles, to 350° and an insertion loss ripple of 3.2 dB, and still keeping good matching.

Since the single RTPS is well matched, it could be supposed that the effect of $S_{11ps}$ in Eq. (3.10) is negligible, producing just twice the phase agility and insertion loss variation. Nevertheless, taking it into account results in a $S_{11reflect}$ that bestows a 324.43° phase agility and 0.97 dB insertion loss variation. Although the phase shift has not doubled, it

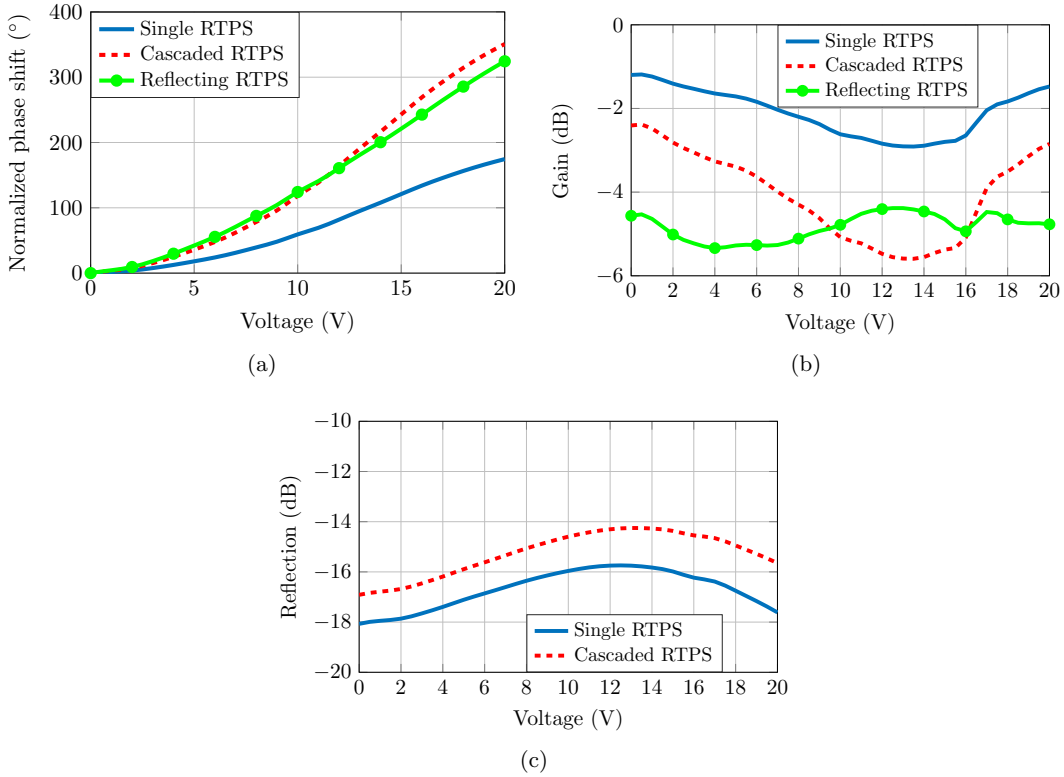


Figure 3.15: Comparison different configurations for the same transforming hybrid coupler. (a) Phase agility. (b) Gain. (c) Reflection in two-ports circuits (matching observation).

offers a better insertion loss equalization for a phase shift range around 320° than what is possible with cascaded phase shifters. Furthermore, the insertion loss ripple is even lower than that from the single RTPS. It is concluded that even when the absolute value of $S_{11_{ps}}$ is low, it can be used to improve the performance of the phase shifter in a reflecting configuration. The comparisons between the three different phase shifters –single, cascaded and reflecting– are plotted in Fig. 3.15.

### 3.3.2. Equalizing resistance

In Chapter 2 it was presented how the use of parallel resistances improves the insertion loss ripple. Such topology could still be employed, but thanks to the reflecting RTPS configuration, another possibility opens up.

The reflecting RTPS is a one-port circuit that reflects a signal after applying a phase correction. As a whole, it acts as a tunable load. Then, its real impedance may be equalized with a parallel resistance. Since a single RTPS configuration already ensures a transition from inductive to capacitive load, there is no need for an impedance transformer and the resistance may be placed directly in parallel to the port of the reflecting RTPS, as indicated in Fig. 3.16.

The reflection coefficient resulting from adding a parallel resistance $R_p$ is

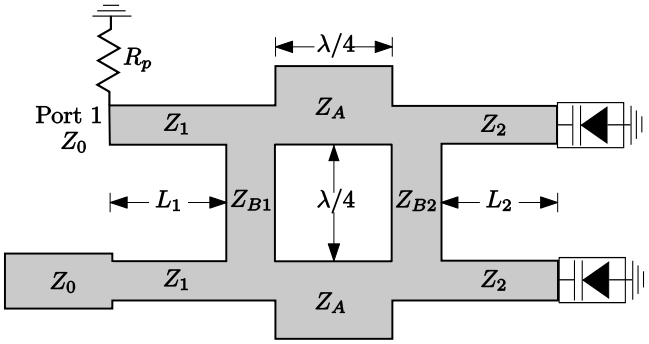


Figure 3.16: Topology of reflecting RTPS with parallel resistance.

$$S_{11reflect||R_p} = \frac{2\,R_p\,S_{11reflect} - S_{11reflect}\,Z_0 - Z_0}{2\,R_p + Z_0 + S_{11reflect}\,Z_0}. \tag{3.11}$$

As before, an example elucidates the benefits of the topology: With a given transforming hybrid coupler of parameters $S_{33} = 0.15 - 0.37j$, $k = 0.65$ and $\angle S_{31} = 46.13°$, a RTPS is obtained with 118.4° phase range and 0.6 dB insertion loss ripple, with return losses just below 9 dB. Cascading it yields a 248.25° phase range, 1.29 dB insertion loss ripple and return losses below 7.7 dB. While the insertion loss variation is decent, the phase agility is low compared to what can be achieved with cascading phase shifters. Still, in a reflecting configuration it produces a big increase in phase agility, up to 331.15°, with 3.48 dB phase ripple. Adding a parallel resistance of 326 Ω, the phase agility suffers a small reduction to 329.26°, whilst the insertion loss ripple is further reduced to 0.98 dB. Fig. 3.17 shows the comparison between the four configurations at each varactor bias voltage.

Still, the phase agility and insertion loss ripple obtained with parallel resistance are similar to the previous example where not resistance was added (Fig. 3.15). The benefit lies instead in design flexibility. For achieving such a phase range and loss variation without resistance, only that solution was found. With parallel resistance, however, different values of $k$ and $R_p$ can be used. It results not only in faster optimization, but in the possibility of designing hybrid couplers with different line impedances –due to different $k$, see Eq. (2.22) to (2.24)– that in turn offer the possibility of optimizing the chip size.

### 3.3.3. Measurements

Following the design process from Fig. 2.15, a reflecting RTPS was designed at 9 GHz in the substrate Arlon 25N, of 30 mil thickness, 3.38 relative electrical permittivity and 0.0025 loss tangent. The values of the structure, which correspond to the geometry from Fig. 2.16, are presented in Table 3.2.

The phase shifter was optimized to obtain a 300° phase agility and insertion loss ripple below 1 dB. Without resistance, it yields 302.74° phase range and 1.6 loss variation. If a 1000 Ω resistance is placed in parallel to the input of the phase shifter, the loss ripple is reduced to 0.66 dB, with the phase agility being almost unaffected, as seen in Fig. 3.18.

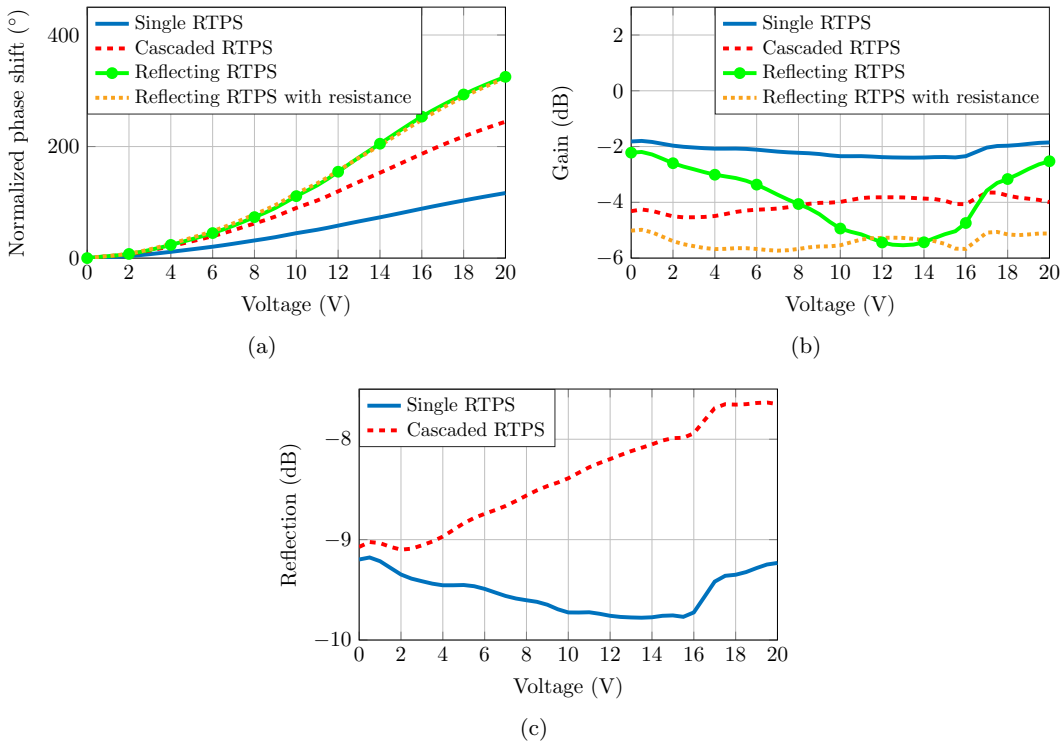


Figure 3.17: Comparison between different configurations for the same transforming hybrid coupler optimized for using a parallel resistance. (a) Phase agility. (b) Gain. (c) Reflection in two-port networks (matching observation).

| $W_1$ | $L_1$ | $W_2$ | $L_2$ | $W_3$ | $L_3$ | $W_4$ | $L_4$ | $W_5$ |
|---|---|---|---|---|---|---|---|---|
| 1.3 | 1.9 | 4.3 | 4.7 | 0.6 | 6.8 | 0.7 | 1.2 | 4.1 |

Table 3.2: Geometry values of the reflecting RTPS prototype according to Fig. 2.16. All measures in mm.

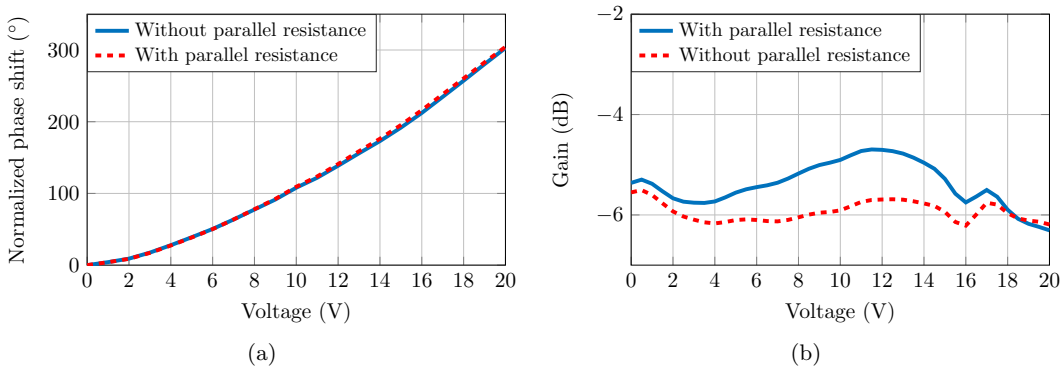


Figure 3.18: Full-wave simulation of the phase shifting response of the reflecting RTPS prototype, with and without parallel resistance. (a) Normalized phase shift. (b) Gain.

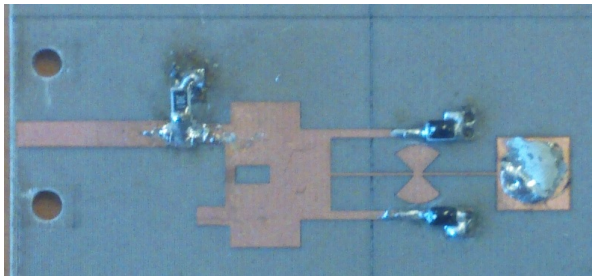

Figure 3.19: Pictured of the reflecting RTPS prototype.

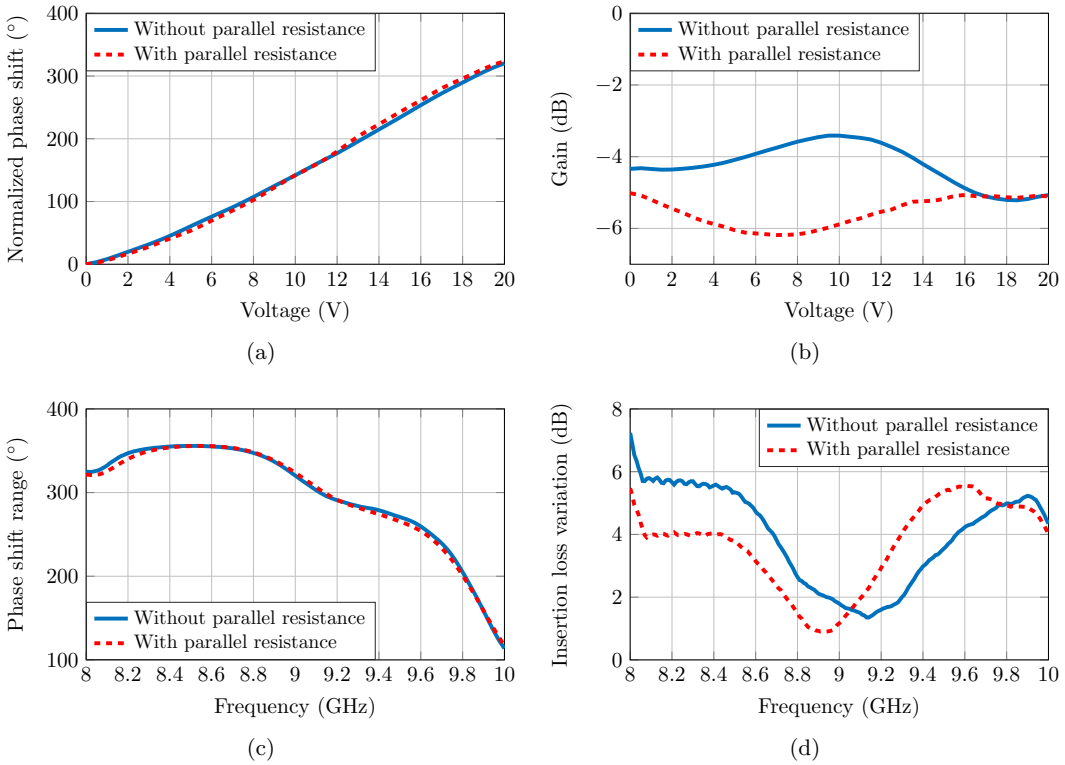


Figure 3.20: Measurements of the phase shifting response of the reflecting RTPS prototype, with and without parallel resistance. (a) Normalized phase shift. (b) Gain. (c) Phase shift bandwidth. (d) Insertion loss variation bandwidth.

A prototype, shown in Fig. 3.19 was manufactured and measured. Its chip size measures $15.8 \times 9.8\,\mathrm{mm}^2$, or $0.47\lambda_0 \times 0.3\lambda_0$. Due to its small size, even in a substrate with low electrical permittivity, it should be easy to fit in a reflectarray with $0.7\lambda_0$ element spacing.

A TRL calibration was employed to discount effects from the connector in the measurements, which are plotted in Fig. 3.20. The measurements were performed both with and without parallel resistors. Due to the packaging parasitics from the SMD resistors, three $330\,\Omega$ resistors were soldered in series since they were found to yield the impedance most similar to a pure $1000\,\Omega$ resistance.

The inclusion of the resistance does not affect the phase shift (320°, a slight increase from what was expected according to the simulation), but decreases the insertion loss

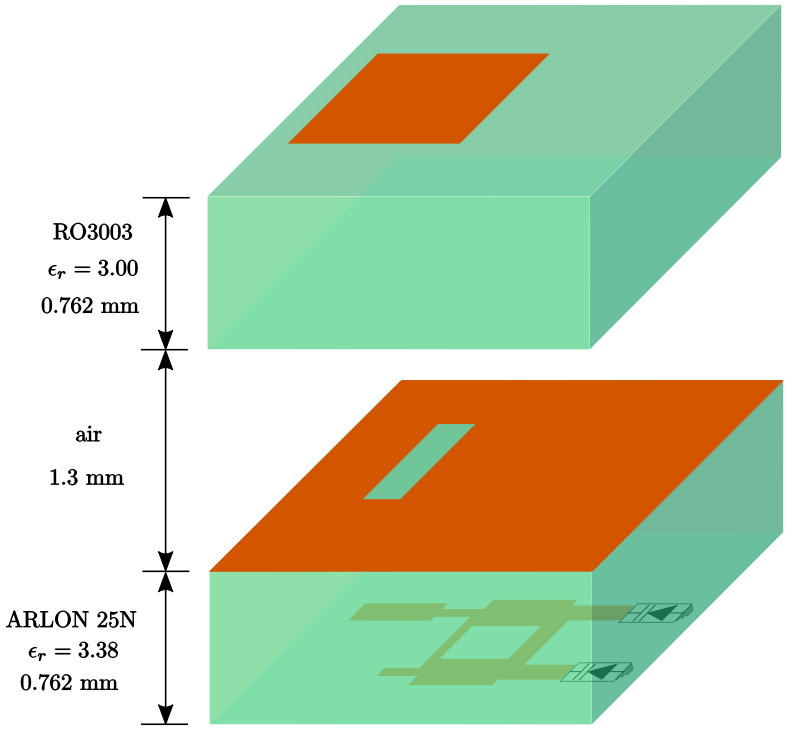


Figure 3.21: Tunable reflectarray cell design.

variation at frequencies below 9.1 GHz. Still, the decrease is not as good as expected at 9 GHz, with a reduction of only 0.57 dB, which can be attributed to the resistors parasitics. It is worth noting that with parallel resistance, the phase shifter bestows a phase shift range above 300° and a loss ripple below 4 dB from 8.07 to 9.13 GHz, which equates to a 12.33% bandwidth.

For the purpose of manufacturing a reflectarray at 9 GHz with no regards to bandwidth, the performance without resistance is good enough, and so, the reflecting RTPS will be used as the reconfigurable element of the unit cell.

## 3.4. Tunable reflectarray cell

With the tunable phase shifter designed, it is imperative to assess its performance once implemented in the reflectarray unit cell, following the design from Fig. 3.21.

### 3.4.1. Reflecting RTPS evaluation

It has been established that the matching of the array element changes depending on the angle of incident of the plane wave from the feed. Since the phase shifter was designed for a 50 Ω reference impedance, any changes to the impedance located in its input port might affect its phase shift and insertion loss. This can be simulated by renormalizing the measurements of the reflecting RTPS to various impedances.

Some examples are displayed in Fig. 3.22. Whilst each of the evaluated impedances are matched with a return loss over 10 dB to 50 Ω, they present significant alterations to

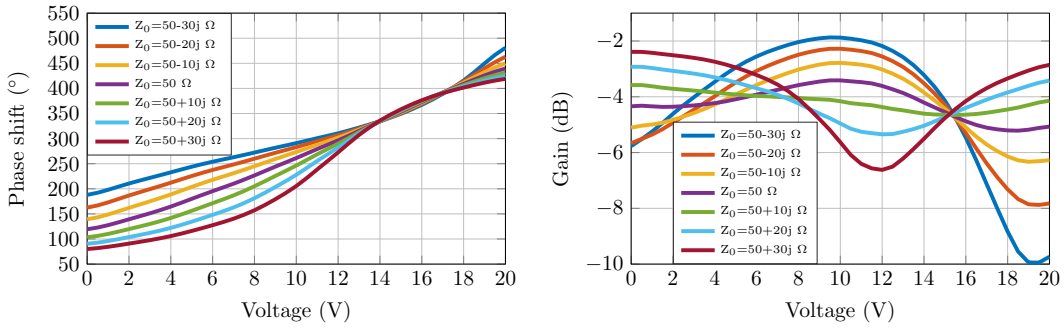


(a) (b)

Figure 3.22: Measurements of the reflecting RTPS renormalized to different impedances. (a) Phase shift. (b) Gain.

| $w_{patch}$ | $l_{patch}$ | $w_{slot}$ | $l_{slot}$ | $w_{line}$ | $l_{stub}$ |
|---|---|---|---|---|---|
| 15.52 | 9.55 | 1.04 | 7.32 | 1.76 | 1.38 |

Table 3.3: Geometry values of the designed reflectarray unit cell according to Fig. 3.2. All measures in mm.

the phase shift and insertion loss, which are more significant as the matching deteriorates. The insertion loss variation increases in each case, up to 8.8 dB for $50 + 30j\,\Omega$. There is also a difference in phase shift for each of the impedances, which is shown to get as high as 120°, more than one third the phase agility of the phase shifter.

Subsequently, it raises the concern that, even if the unit cell is matched at every angle of incidence, their different impedances might negatively impact the performance of the phase shifter and, worst of all, achieve an inconsistent phase shift at the same bias voltage. To minimize this impact, it is mandatory to achieve the best possible matching of the unit cell at each incidence angle. There are two approaches: optimizing each cell individually to its incidence angle –which would be very time consuming in large antennas– or dividing the reflectarray into subarrays, and optimizing one unit cell to several incidence angles.

For the same reflectarray as in the fixed case presented before ($4 \times 4$ elements, $0.7\,\lambda_0$ spacing at 9 GHz, feed located in $x = -100$ mm and $z = 200$ mm), a single unit cell was optimized for achieving a return loss above 20 dB at every incidence angle, with the geometry parameters from Table 3.3.

To properly evaluate the performance of the cell, the S-parameters matrices of the Floquet simulations at each incidence angle with a microstrip port were cascaded to the measurements of the reflecting RTPS, and the resulting reflection coefficient was analyzed for obtaining the phase shift and insertion losses, following the schematic of Fig. 3.23, where

$$S_{11cell} = S_{cp,cp} + \frac{S_{cp,\mathrm{mstrip}}\, S_{\mathrm{mstrip},cp}\, S_{11reflect}}{1 - S_{mstrip,mstrip}\, S_{11reflect}}, \tag{3.12}$$

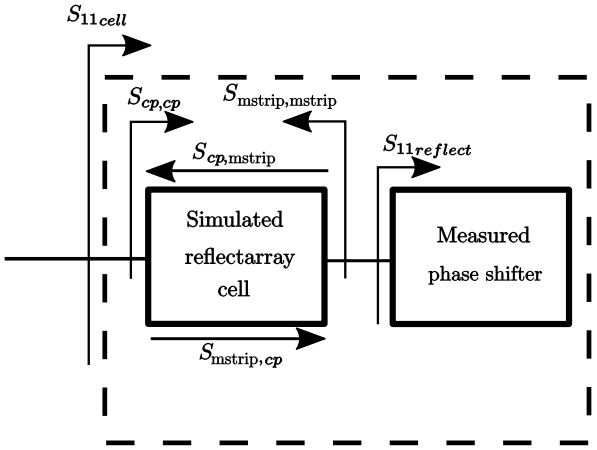


Figure 3.23: Schematic of the scattering parameters analysis for evaluating performance of tunable unit cell.

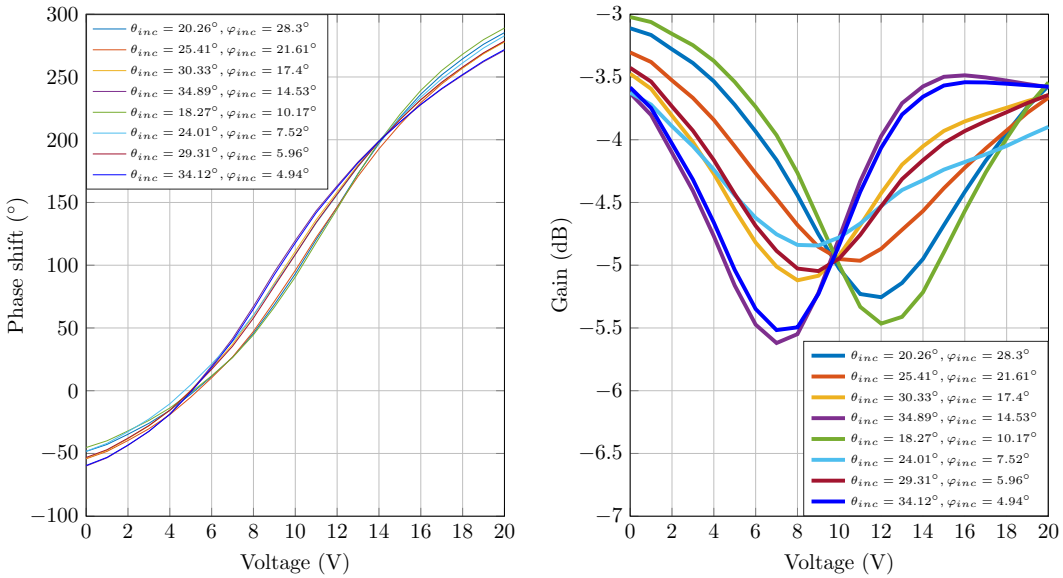


(a) (b)

Figure 3.24: Simulation of the tunable reflectarray unit cell at different incidence angles with the reflecting RTPS measurements. (a) Phase shift. (b) Gain.

with *cp* equating to the co-polar component of the reflectarray.

Thus, each of the 16 elements can be evaluated, with their phase shift and gain displayed in Fig. 3.24. The maximum phase shift difference between cells at the same bias voltage is of 30°, less than 10% of phase agility, which is more than 320°. While the insertion loss varies from cell to cell, the biggest possible difference is of 2.6 dB. With an acceptable performance, it stresses how important it is to accomplish matching with return losses well above 10 dB.

(a)

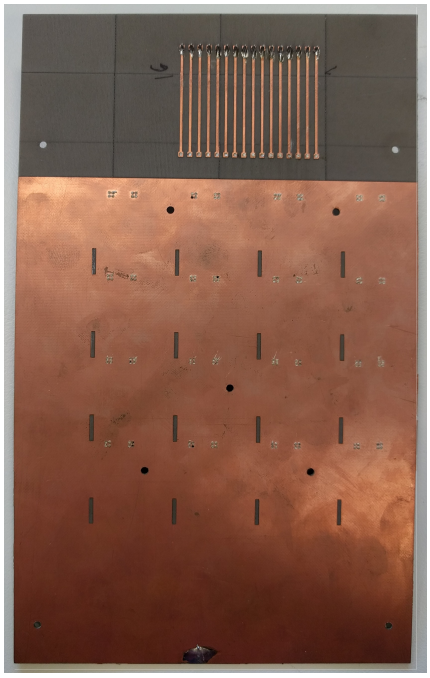

(b)

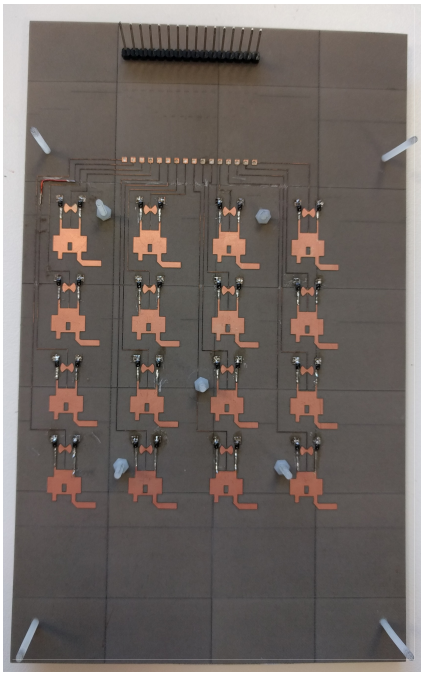

(c)

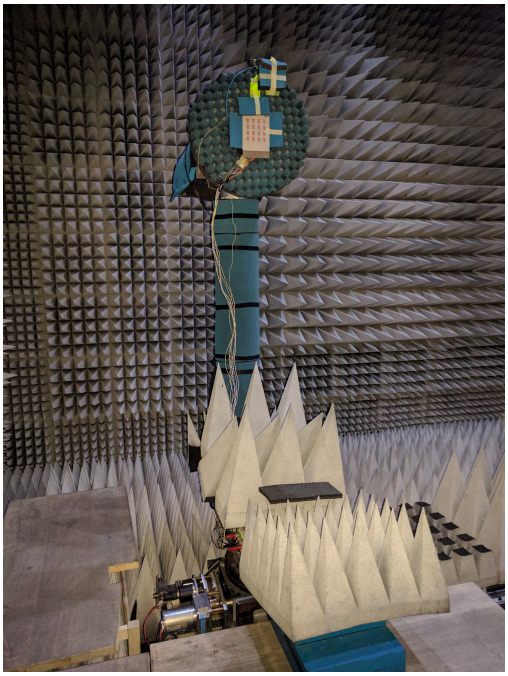

(d)

Figure 3.25: $4 \times 4$ reflectarray prototype. (a) Patch antennas layer. (b) Slots layer. (c) Phase shifters layer. (d) Anechoic chamber set-up.

### 3.4.2. Tunable reflectarray measurements

The optimized unit cell was employed to manufacture a $4 \times 4$ reflectarray antenna. 16 biasing lines were added on the phase shifters layer to control each varactor pair individually.

Since these lines are not located in the radiating elements layers and are separated from the feed by the ground plane from the slots layer, no spurious radiation can be expected from them. Holes were drilled to introduce nylon screws with 1.3 mm thick washers, that ensure proper separation between the Arlon 25N and Rogers 3003 substrates, as per Fig. 3.23. Each biasing line is controlled by the evaluation board of the 32-channel, 14 bits AD5535B digital to analog converter (DAC). Since the 14 bits are applied to a 50 V range, it equals roughly to a 12 bits resolution for a 20 V range, offering almost a 1 mV precision. An Arduino microcontroller was connected to the DAC for communicating the data to apply the correct biasing voltage at each output. To minimize voltage errors, the offset error (analog output when expecting 0 V) and gain error (analog output slope versus digital input) were taken into account for each channel. Thus, the digital codes pertaining to each desired phase shifter voltage are coded into the Arduino, which sends them to the DAC, producing the necessary analog output. The DC voltages to apply are derived from the reflecting RTPS measurements from Fig. 3.20.

To quickly evaluate the tunable properties of the reflectarray, a beam steering sweep was realized in the azimuth and elevation planes. The antenna was fixed to a rotating pole in an anechoic chamber, and measurements were realized in the plane in which the main beam was located. Pictures of the prototype and measurement set-up can be found in Fig. 3.25. The beam sweep in the azimuth plane (H-plane) was performed from $-10°$ to $30°$, shown in Fig. 3.26. The beam sweep in the elevation plane (E-plane) was performed from $-20°$ to $20°$, showcased in Fig. 3.27. The results are compared with the HFSS simulation of a reflectarray of same dimensions with different stub line lengths for each case.

As in the case of the measurements of the fixed reflectarray, there has been an increase of specular radiation (around $25°$ in azimuth) and diffraction, which widens the main beam an increases the level of secondary lobes. This could be averted by increasing the number of elements and thus, the antenna aperture. Still, the main beam is centered at the expected angle, with even more accuracy than the fixed reflectarray simulation. However, it is difficult to argue precision due to the high beamwidth, consequence of the small array factor. Nevertheless, the precision could potentially be improved by biasing the elements according to the phase shift from each cell –as in Fig. 3.24– instead from just the RTPS measurements.

The scan loss can be appreciated in Fig. 3.28. In the H-plane, the main beam gain decreases as the beam steers from the specular radiation. In the E-plane, the maximum gain is obtained at broadside, and the biggest loss is produced when the beam is focused at $-20°$, due to the appearance of a high secondary lobe level. This effect can be attributed to the main beam being the furthest away from the specular radiation. At the other angles, the scan loss is below 3 dB.

## 3.5. Conclusions

In this chapter, the guided-wave approach to designing a reflectarray was presented and analyzed. This approach offers the benefit of performing a modular design of the antenna,

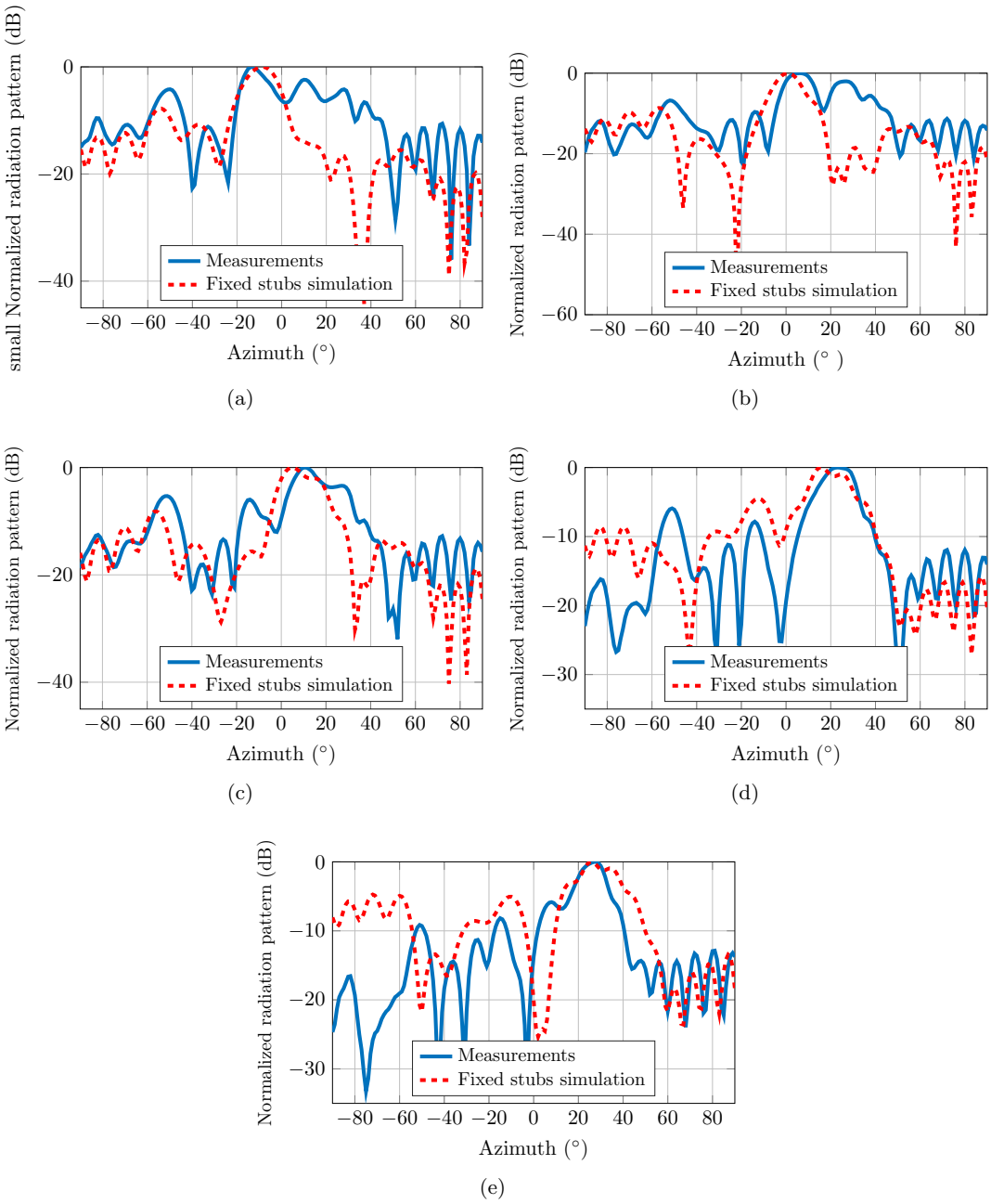


Figure 3.26: Main beam sweep in the H-plane. (a) −10°. (b) 0°. (c) 10°. (d) 20°. (e) 30°.

differentiating the radiating element of the array from the phase shifter. Thus, each element can be optimized independently. To that purpose, the unit cell employed is composed of a patch antenna, which is coupled through a slot in the ground plane to a microstrip line. Through the Floquet analysis of the commercial software HFSS, infinite periodicity condition are simulated, and so it is possible to characterize the unit cell of the array. Since the impinging wave of the feed antenna onto each radiating element is defined through the S-parameters of the dominant Floquet modes, the problem is reduced to the matching of the appropriate Floquet mode to the microstrip line.

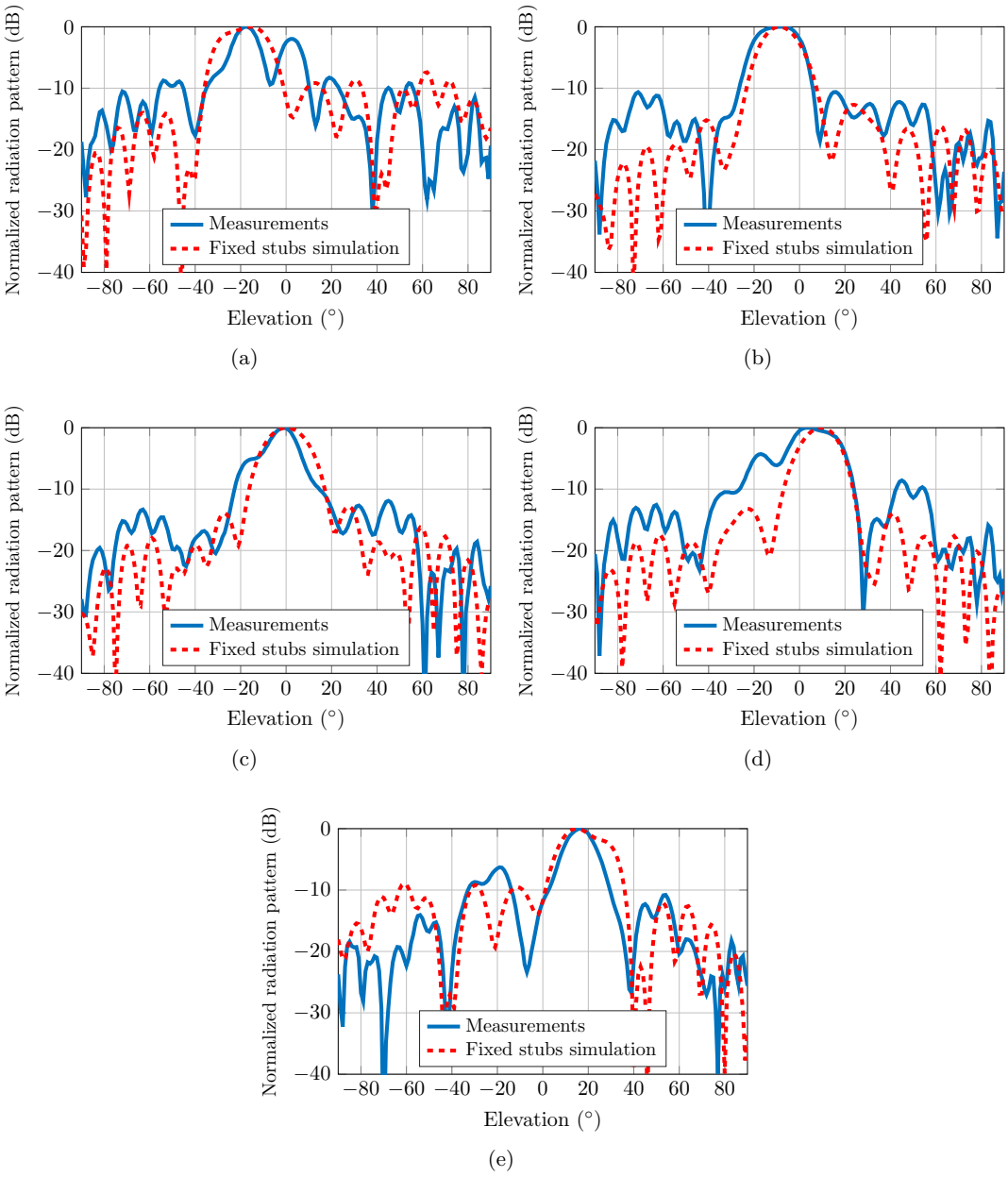


Figure 3.27: Main beam sweep in the E-plane. (a) −20°. (b) 10°. (c) 0°. (d) 10°. (e) 20°.

Typically, a cell is only designed at normal incidence, but it was shown that the matching deteriorates as the incidence angle of the impinging plane wave increases. It is then necessary to take the incidence angles into account to achieve proper matching for each element of the array. Once matching is adequate, the phase shifter element can be introduced in the transmission line. A known fixed reflectarray design consists in employing stub lines of different length to obtain the appropriate phase shift at each element. Using this method, two fixed $4 \times 4$ reflectarrays at 9 GHz were manufactured and measured for achieving beam steering at broadside and 45° azimuth, validating the simulations and optimizations of the unit cell.

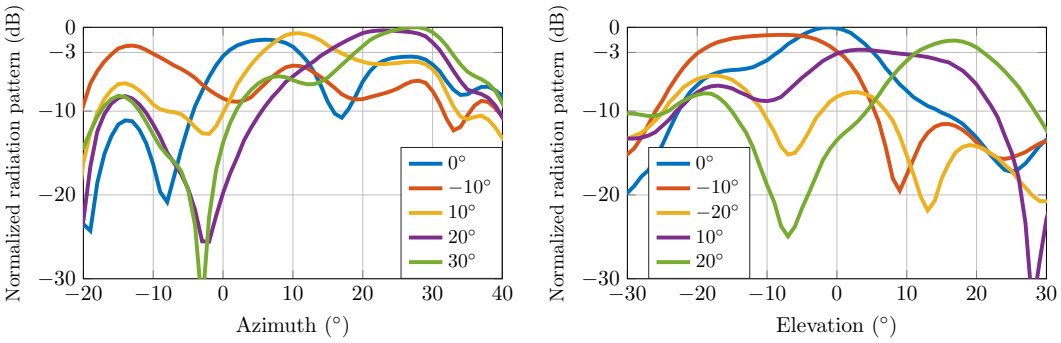


Figure 3.28: Scan loss measurements comparison of the tunable reflectarray. (a) H-plane. (b) E-plane.

For achieving reconfigurability, it is mandatory to introduce a tunable phase shifter. None of the reflecting-type phase shifters from Chapter 2 works as a one-port network in which the phase shifted signal is reflected back, which suits better the topology of the reflectarray unit cell. Subsequently, an analysis of the RTPS as a one-port circuit was performed by leaving one of the ports open-ended. In this topology, the previous matching restrictions of a RTPS can be forfeited, resulting in additional improvements in phase agility and insertion loss, surpassing those of two cascaded phase shifters. The performance can be further improved with the addition of a single parallel resistance at the input port. To further illustrate the benefits, equal impedance transforming hybrid coupler were analyzed in the different RTPS topologies, stressing how the one-port circuit produces the best results.

A phase shifter was manufactured in the substrate Arlon 25N, of $\epsilon_r = 3.38$, and measured, producing at 9 GHz a 320° phase agility with an insertion loss from 3.4 to 5.2 dB, whose variation can be further reduced to 1 dB by parallel resistors without affecting the phase agility. The phase shifter yields a phase shift range above 300° and a loss variation below 4 dB in a 12.33% bandwidth. The chip size is small enough to fit in a reflectarray with $0.7\lambda_0$ element spacing, and could fit in smaller unit cells if a substrate with higher electric permittivity had been employed.

In this reflecting RTPS topology, the port impedance has a notorious effect on the performance of the phase shifter. Renormalizing the measurements to different complex impedances, it was shown that the phase range and insertion loss greatly varies, even with impedances that are matched to the reference impedance with a return loss over 10 dB. This observation remarks how important it is to achieve excellent matching for each and every element of the array, since the phase difference between cells for the same biasing voltage could be over 100°. To minimize this effect, the unit cell of the $4 \times 4$ fixed reflectarray was optimized for achieving the best possible matching at every incidence angle. In bigger reflectarrays, with higher variation of incidence angles, different unit cells might be used for ensuring optimal matching, dividing the antenna into subarrays.

Combining the unit cell simulations with the phase shifter measurements, the expected

unit cell performance was obtained, with a variation between elements of phase shift below 30° and of insertion loss below 2.5 dB. Thus, a full $4 \times 4$ reconfigurable reflectarray was designed and manufactured, drawing seperate biasing lines for each element. The voltage of each pair of varactors was controlled by a digital to analog converter governed by a microcontroller. With the phase shift from the RTPS measurements, it is surmised which voltage must be applied at each element for obtaining a desired beam steering.

The reflectarray was characterized in an anechoic chamber. The radiation pattern suffers from the small size of the antenna, with noticeable diffraction and specular reflection. However, the tunability was found to be enough to obtain beam steering from $-10°$ to 30° in azimuth and from $-20°$ to 20° in elevation.

CHAPTER 4

# Guided-wave approach to a tunable array lens

## 4.1. Introduction

An array lens is an spatially-fed antenna in which one side is illuminated by a feed, and the radiation is produced in the other. The elements of the array perform phase correction so that the waves pertaining the side not illuminated produce a desired radiation pattern.

Controlling the resonance of the radiating elements allows to tune the transmitted phase. However, multiple resonators are needed to achieve good phase range [4], incurring in an increase of the thickness of the lens, or an increase of complexity in the control circuit due to using different resonators within the same unit cell.

In the guided-wave approach, the array element illuminated by the feed is coupled to a two-port circuit, which then guides the electromagnetic field to the array element on the other side, producing the radiation (Fig. 4.1). A phase shifter could be implemented in the two-port circuit, with the limitation of having to output the signal to the opposite side from which it was input. This can be achieved by constructing 3D structures [38], which increases array thickness and manufacturing complexity; by stacking an additional microstrip-fed patch [39], which extends the chip footprint; or by using differential microstrip lines with bridged-T phase shifters [37], that does not have the performance tunability of the reflection-type phase shifter.

In order to benefit from the work presented in Chapters 2 and 3, the most obvious lens design would consist of a patch antenna coupled through a slot to a microstrip line in both the receiving and transmitting sides of the array, as in Fig. 3.2. To achieve a small element spacing, the microstrip phase shifter element between them could be implemented

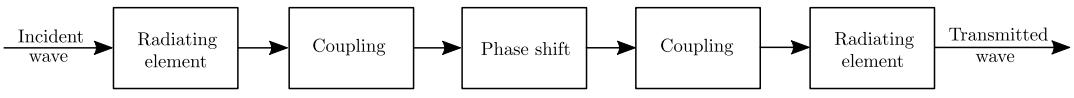


Figure 4.1: Schematic of the unit cell of a guided-wave reflectarray.

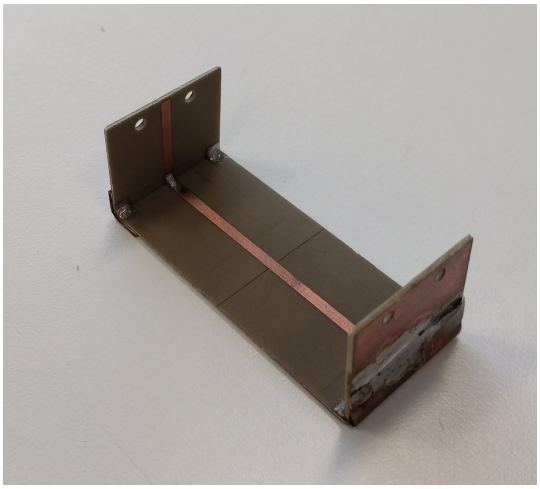

Figure 4.2: Picture of a reference plane change of a microstrip line with two bends.

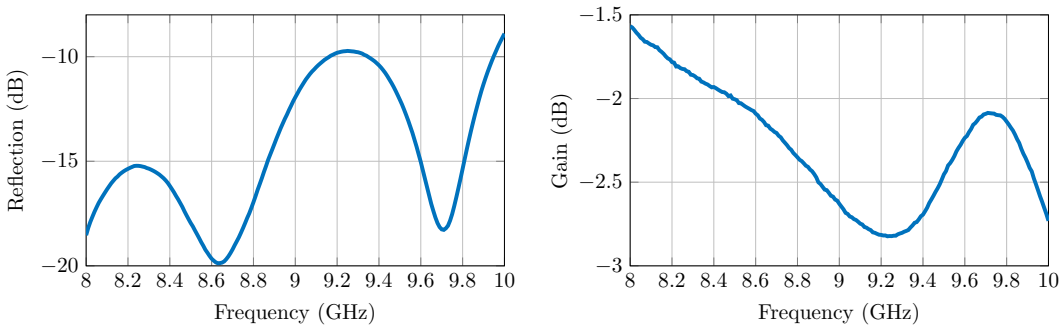


Figure 4.3: Measurements of a microstrip perpendicular reference plane change. (a) Reflection. (b) Gain.

in a perpendicular reference plane change as the one from Fig. 4.2, which would also favor cascading two or more phase shifters due to the space available in the perpendicular plane. However, it was found that the reference plane change incurred in an increase of insertion loss, as showcased in Fig. 4.3, besides adding an extra step in the manufacturing process, increasing the array thickness and resulting in a fragile structure.

Since exploring alternatives is more desirable, technologies other than microstrip ought to be looked into. This chapter proposes the use of substrate integrated waveguide (SIW), since thanks to its rectangular waveguide-like properties, it facilitates coupling a signal through opposing sides. Following the scattering parameters analysis of a reflective-type phase shifter from Chapter 2, a novel SIW phase shifter is designed utilizing slots loaded with tunable loads, achieving a compact chip size while maintaining similar performance to a RTPS. Then, a $2 \times 2$ reconfigurable array lens is designed and measured, serving to demonstrate the implementation and unit cell design with the SIW phase shifter.

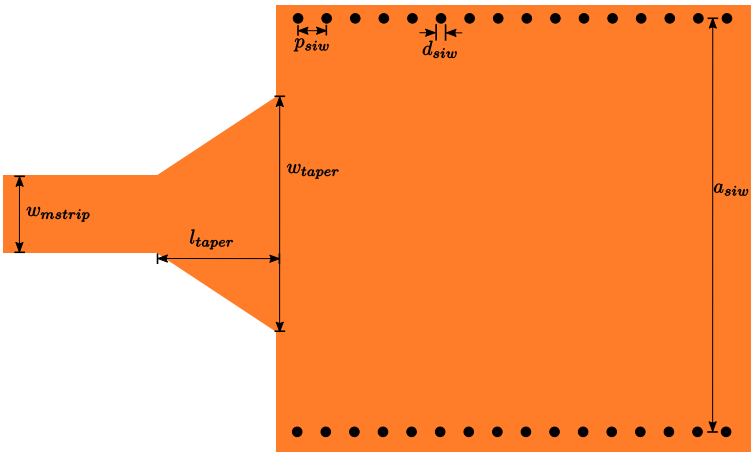


Figure 4.4: Layout of a SIW circuit with microstrip transition.

## 4.2. Substrate integrated waveguide

### 4.2.1. Operation principle

Substrate integrated waveguide (SIW) is a planar technology in which a waveguide structure is realized by embedding two rows of metalized via-holes connecting two plates of electrical conductor in a dielectric substrate. This way, a structure that behaves similarly to a rectangular waveguide is obtained, albeit with TM modes not being supported due to the gaps between the metal vias. The fundamental mode $TE_{10}$ is, nonetheless, propagated in the same way provided that the SIW meets appropriate geometrical dimensions [72]. The width of the equivalent rectangular waveguide filled with the same dielectric substrate can be obtained as [73]:

$$w_{eff} = a_{siw} - \frac{d_{siw}^2}{0.95\, p_{siw}}, \tag{4.1}$$

where $a_{siw}$ is the separation between the rows of via-holes, $d_{siw}$ is the diameter of said holes, $p_{siw}$ is the distance between the centers of adjacent holes in the same row and $w_{eff}$ is the width of the equivalent rectangular waveguide. While there are more refined expressions ( [74], [75]), Eq. (4.1) is accurate enough to act as a starting point for further optimization, if needed, in a full-wave simulator. Since rectangular waveguides are well-known structures, the equivalent width, the thickness of the substrate and its dielectric permittivity are used to calculate the cut-off frequencies of the TE modes, thus corroborating that at the operating frequency only the intended modes are being propagated. Additionally, to minimize radiation losses, the SIW geometry must comply with $p_{siw}/d_{siw} < 2.5$, that is, the gap between holes must be small enough to not permit radiation leakage [76].

To properly characterize or feed SIW circuits it is necessary to transition to technologies in which connections can be performed more conveniently. A transition to microstrip technology can be easily performed by adding a simple taper [77], as it is depicted in Fig. 4.4. While design equations exist [78], optimizing the taper length and width is easily done through tuning in full-wave simulations.

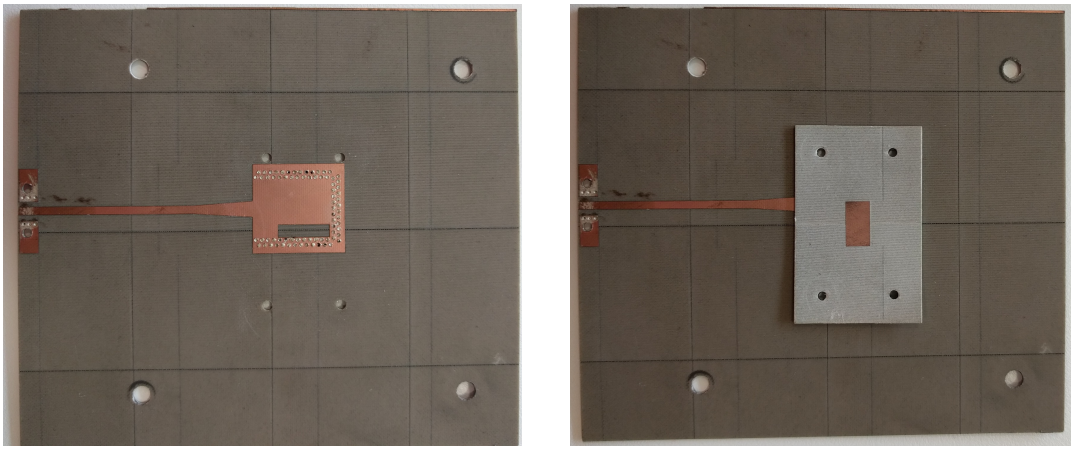

(a) (b)

Figure 4.5: Picture of SIW patch antenna with longitudinal coupling slot. (a) Without patch. (b) With patch.

Through proper values of SIW parameters and taper optimization, the propagation of the fundamental mode is guaranteed. The next step is ensuring an efficient way of coupling the field to a radiating element.

### 4.2.2. Coupling to patch antennas

The fundamental mode of the SIW can be fed to rectangular patch antennas in another substrate by a longitudinal or transverse coupling slot. One end of the SIW is short-ended with metallized via-holes covering the width of the guide, and the coupling slots are placed at the maximum (in the case of the longitudinal slot) or minimum (in the case of the transverse slot) of the resulting standing wave [79]. Both cases result in the radiation of linear polarization, though differing on being parallel or perpendicular to the propagating direction of the SIW. Designing a prototype for both instances can help elucidate which one is more useful in an array lens configuration.

A SIW was designed in the substrate Arlon 25N, of $\epsilon_r = 3.38$, 30 mil thickness and loss tangent 0.0025, with the design parameters $a_{siw} = 13.6$ mm, $d_{siw} = 0.8$ mm, $p_{siw} = 1.3$ mm, $l_{taper} = 12.7$ mm, $w_{taper} = 3.5$ mm and $w_{mstrip} = 1.73$ mm, obtaining the propagation of only the fundamental mode from 8 to 10 GHz. This SIW was used to realize patch antennas with the two different slot configurations, both feeding a patch antenna realized in the substrate RO3003, of $\epsilon_r = 3$, and thickness of 30 mil, located 1.3 mm away from the SIW in the $z$-axis, leaving a vacuum layer.

#### 4.2.2.1. Longitudinal slot

The longitudinal slot is placed $\lambda_g/4$ (where $\lambda_g$ stands for waveguide wavelength) away from the SIW short, and close to the SIW edges for coupling the longitudinal magnetic field where it is maximum. The position of the slot, its width, length, and that of the patch antenna can be optimized through a full-wave simulator. It was designed for working at 9

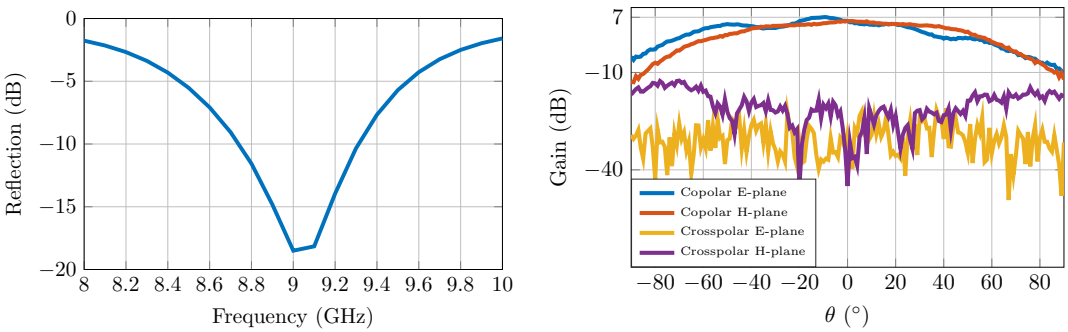


Figure 4.6: Measurements of SIW patch antenna with longitudinal coupling slot. (a) Reflection. (b) Gain.

GHz with a slot width of 2.82 mm, slot length of 11.19 mm, patch width of 5.38 mm and patch length 10.2 mm. The manufactured prototype is depicted in Fig. 4.5. The slot is located as near as possible to the metallic vias, and while its center is roughly $\lambda_g/4$ away from the short end, its further edge is next to the metallized vias.

Measurements were realized for matching and gain (Fig. 4.6). The bandwidth for matching with a return loss above 10 dB is of 6.7%, and the maximum co-polar gain is of 7 dB, similar to that of a microstrip patch antenna. The maximum gain is, however, slanted in the E-plane, and found at $\theta = -10°$. The maximum cross-polar gain is of -12.5 dB.

#### 4.2.2.2. Transverse slot

According to [79], the transverse slot has to be placed $\lambda_g/2$ away from the SIW short, and on the center of the SIW for coupling the transverse magnetic field where its maximum. Nevertheless, the slot can be placed next to the short via-holes, which is still a minimum of the standing wave, and thus reduce the chip footprint. As with the longitudinal slot, an antenna was designed and manufactured for working at 9 GHz, with slot width of 2.34 mm, slot length of 9.17 mm, patch width of 7.78 mm and patch length of 10.06 mm. Fig. 4.7 shows the prototype with the slot just next to the metalized vias.

The performed measures displayed in Fig. 4.8 showcase an increase in matching when compared to the longitudinal slot, obtaining a 9.3% bandwidth. The co-polar gain has increased to 8.1 dB and the deviation of the maximum of the E-plane is smaller, being measured at $\theta = -2°$. On the other hand, the cross-polar gain has also grown, reaching -8 dB in the worst case.

Despite considering gain, matching and cross-polar level, the chip footprint is the most important aspect as it can determine the element spacing in the array lens. While the SIW width is fixed and does not change for each slot, the waveguide length is dependent on them. For the longitudinal slot, the 11.19 mm covered by it can not be used for another purpose. In the transverse slot, that is only the case for its width, which is only 2.34 mm. That means that the chip footprint of the transverse slot is 20% of that of the longitudinal

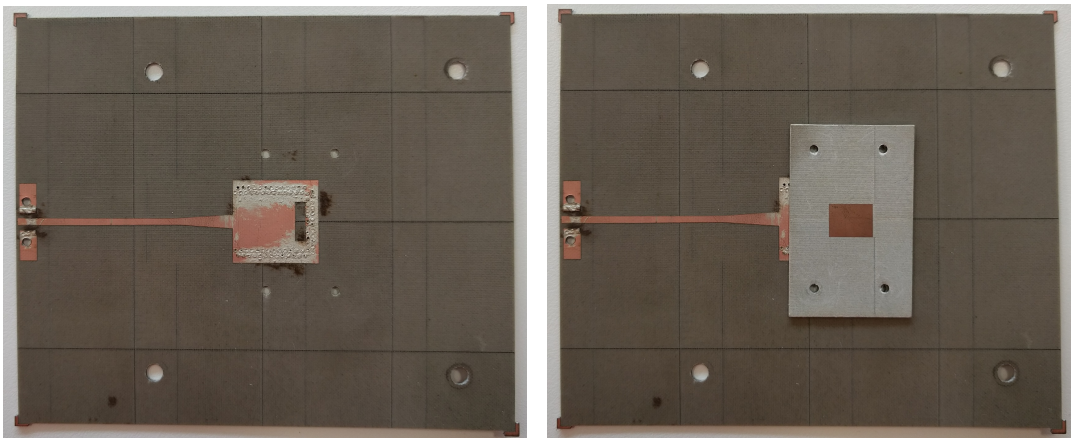

(a) (b)

Figure 4.7: Picture of SIW patch antenna with transverse coupling slot. (a) Without patch. (b) With patch.

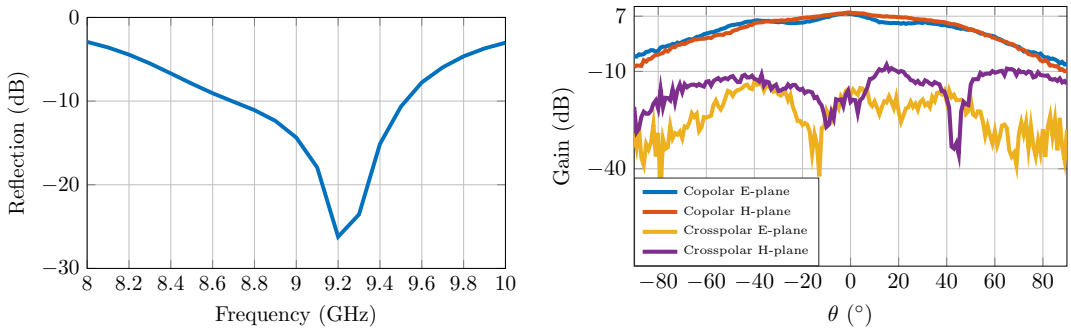


(a) (b)

Figure 4.8: Measurements of SIW patch antenna with transverse coupling slot. (a) Reflection. (b) Gain.

slot. Adding to this the increase in matching bandwidth and co-polar gain, the transverse slot offers superior characteristics for an array lens implementation.

Therefore, the radiation elements and the coupling to waveguide are defined. According to the schematic from Fig. 4.1, only the implementation of a phase shifter in SIW technology remains.

### 4.2.3. Hybrid couplers and RTPS

It was established in Chapter 2 that reflecting-type phase shifters offer good characteristics for being employed in tunable phased arrays. This kind of phase shifters require the implementation of hybrid couplers. In SIW technology, hybrid couplers are realized in a single layer by leaving an aperture in two parallel waveguides [80], realizing an H-shape in which a $TE_{20}$ mode is excited [81], or through a cruciform configuration [82], a prototype of which is shown in Fig. 4.9. This last structure is the most compact of the single layer SIW couplers found in the literature and offers different coupling levels between ports

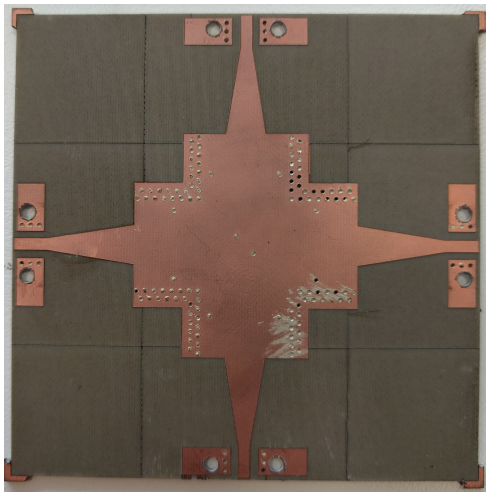

Figure 4.9: Prototype of a cruciform hybrid coupler.

thanks to the position of the metalized via-holes in the center of the cruciform structure. However, it does not offer impedance transforming capabilities, that were shown to be key tin controlling the phase shifter performance. Furthermore, even in this compact structure, the chip footprint is considerable due to having to fit 4 different waveguides ($30 \times 30\text{mm}^2$ in the prototype example), and there is still the need of adding the tunable loads with an appropriate impedance transformer.

In [83], a RTPS in SIW technology was realized by shorting two ports of the hybrid coupler with metallic via-holes and placing transverse slots loaded with varactors. Through the optimization of the slots, some control of the performance of the phase shifter was realized, but not as extensive as with impedance transformers. Besides, the chip size of the hybrid coupler makes the design undesirable for array lens implementations. In [84], a multilayer SIW hybrid coupler is implemented through a longitudinal slot, and the varactors are placed in a different layer, resulting in a 4-layers structure, and offering no control of the insertion loss variation. A new approach needs to be taken.

The possibility of changing the behaviour of a circuit using a varactor loaded slot is well-known [85]. Furthermore, using metamaterial resonators loaded with varactors opens up new ways of realizing tunable circuits [86]. Thus, drawing from these techniques can result in a new phase shifting structure that would replace the traditional coupler and short-terminated loads topology.

## 4.3. Phase shifter element

### 4.3.1. Impedance transforming hybrid coupler equivalence

In a waveguide, tilting resonant slots and offsetting their positions serves to achieve different coupling levels between ports in a multilayer configuration [87]. For the proposed topology, instead of coupling the fields to another waveguide, the center of the slots can be considered as ports where tunable loads would be located.

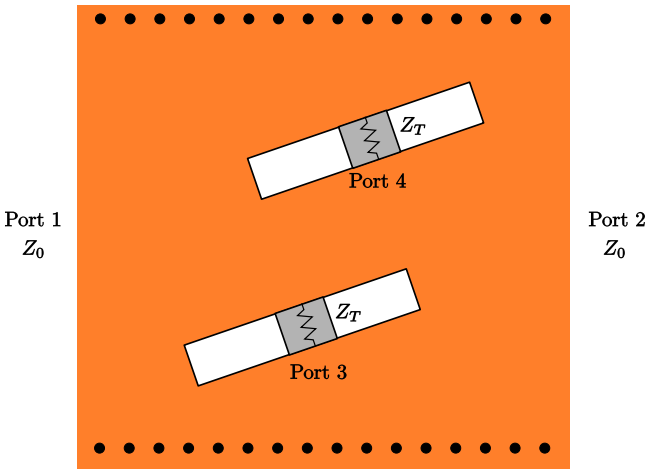


Figure 4.10: Ports layout of an impedance transforming hybrid coupler in SIW.

Relating to the impedance transforming hybrid coupler from Fig. 2.5, the SIW ends would act as ports 1 and 2 (referenced to the SIW impedance), while the center of the slots would act as lumped ports 3 and 4, which would have a different $Z_T$ impedance, according to Fig. 4.10. When the slots are properly matched, the signal transmitted from port 1 is received at ports 3 and 4 with a 90° phase difference, and port 2 is isolated (as indicated in Eq. (2.20)).

The structure can also be observed with every port referenced to the same $Z_0$ impedance. In Eq. (2.18), it was shown that the transmission coefficient between ports 1 and 2 has the same absolute value as the reflection coefficient in ports 3 and 4. Hence, when the slot impedance changes, so does the isolation between the SIW ports. The less field coupled by the slots, the more different it will be to the reference impedance.

To properly realize an impedance transforming hybrid coupler with loaded slots, the reflection coefficient at ports 3 and 4 must be the same as the one produced by the $Z_T$ impedance ($S_{33}$), which in turn is the impedance that would yield the proper RTPS performance. The transmission coefficient to those ports must have the same absolute value (balanced coupling, with $k = 1$) and have a phase difference of 90°, so that the signal gets canceled out at the input port regardless of what impedance is loaded on the slots.

### 4.3.2. Loaded tilted slots design

In the proposed topology, two tilted slots are placed on one layer of the SIW. For performing full-wave simulation, two lumped ports are placed on the center of each slot, with their width being that of the component packaging which will be soldered on, and their length equating the slot width. The coupling level is controlled by the width ($w_s$), length ($l_s$), inclination ($\Phi$), and position of the slots. The wider, longer and more tilted they are, the more field they will perturb, resulting in more coupling to the slots. Placing them further from the center width-wise results in a perturbation of a weaker field, decreasing the coupling ($s_2$). In addition, the amplitude balance and phase difference between the

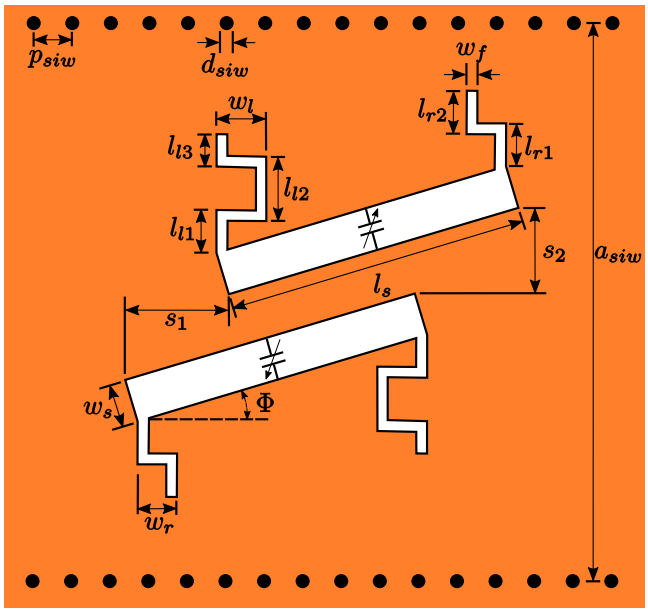


Figure 4.11: Layout of the loaded tilted slots SIW phase shifter.

coupling of each slot can be controlled by offsetting their position along the waveguide length ($s_1$).

While the field which would be coupled to the slots will always depend on the reflection coefficient of the desired $Z_T$ matching impedance, there are always two conditions that the coupling must comply with: equal magnitude for each slot and a phase difference of 90°. The combination of the described parameters must then be used to ensure those two conditions, while maintaining acceptable return losses.

The dominant $TE_{10}$ mode experiences a multi-mode excitation by the slots. The electric field is split in two halves reminiscing a $TE_{20}$ mode, but with a phase difference of 90° between the bottom and top half. After passing through the slots, the sum of the fields is again the $TE_{10}$ mode, minus the insertion losses incurred. A demonstration of this behavior is exhibited in Fig. 4.12, with the plotted fields calculated by a full-wave simulator.

Still, the described geometry presents one important limitation, which is the range of impedance matching that can be achieved. It provides no way of tuning the complex value of $S_{33}$ to the extent of which is necessary to optimize a reflection-type phase shifter. In order to achieve a desired impedance matching in SIW, metamaterials can be used [88]. Subsequently, two interdigitated capacitors are placed at each end of the slots, facing towards the nearest metalized via-holes wall so that they do not cause much field perturbation and mismatching (with slot width $w_f$ and different segment lengths for more tunability).

The final layout of the structure is shown in Fig. 4.11. By controlling the tilt, length, width and position of the slots, combined with the geometry of the interdigitated capacitor at their sides, a circuit is obtained that can yield the same scattering parameters as an impedance transforming hybrid coupler, with the center of the slots as the location where

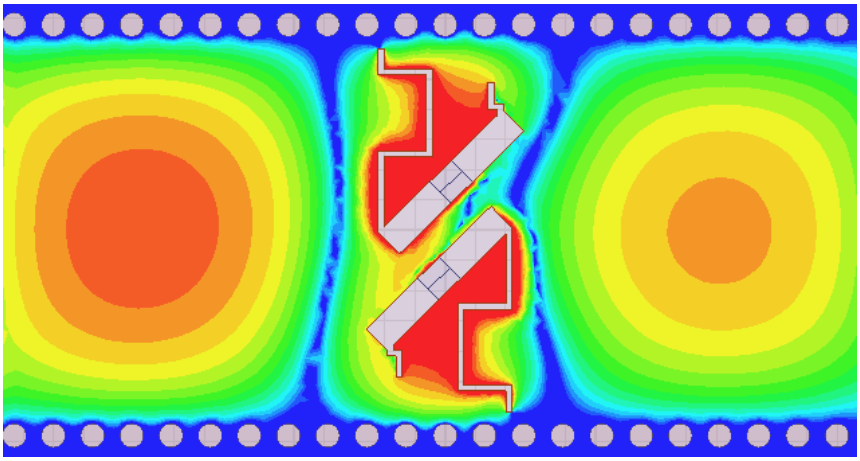

Figure 4.12: Magnitudes of the electric field in the loaded tilted slots SIW phase shifter.

| **Capacitance** | 0.3 pF | 0.5 pF | 0.7 pF | 1.3 pF | 2.7 pF |
|---|---|---|---|---|---|
| **Impedance (Ω)** | 0.5146 | 0.3945 | 0.3553 | 0.6113 | 1.7096 |
| | -32.3682j | -10.4862j | -1.5122j | +10.7130j | +16.0699j |

Table 4.1: Impedance of capacitors.

the tunable loads are placed.

### 4.3.3. Measurements

In order to test the viability of the proposed SIW phase shifter, two circuits were optimized using HFSS for the substrate Arlon 25N of 30 mil thickness, dielectric constant of 3.38 and 0.0025 loss tangent, and then manufactured and measured. The first one was designed for using different fixed capacitors, as to discount possible effects introduced by the bias network. The second one uses varactors and serves as a prototype of a tunable, continuous phase shifter, which could be used in an array lens.

#### 4.3.3.1. Fixed capacitors design

This prototype was designed with the purpose of soldering different capacitors to verify that the expected phase shift was obtained. The capacitors utilized are multi-layer ceramic capacitors from Johanson Technology in the 0402 packaging, with capacitance values of 0.3, 0.5, 0.7, 1.3 and 2.7 pF. The models provided by the manufacturer were used to ascertain which matching network would provide the best performance, and the equivalent impedances at 9 GHz are shown in Table 4.1. Applying Eq. (2.10), (2.11), with $\Gamma$ as the reflection coefficients from the different capacitors, the performance of the phase shifter for different $Z_T$ impedances is obtained, as indicated in Fig. 4.13.

The phase shifter was optimized for the slots to be matched to $Z_T = 14.72 + 9.86j\,\Omega$ at 9 GHz, which according to Fig. 4.13 achieves a good trade-off between phase agility and

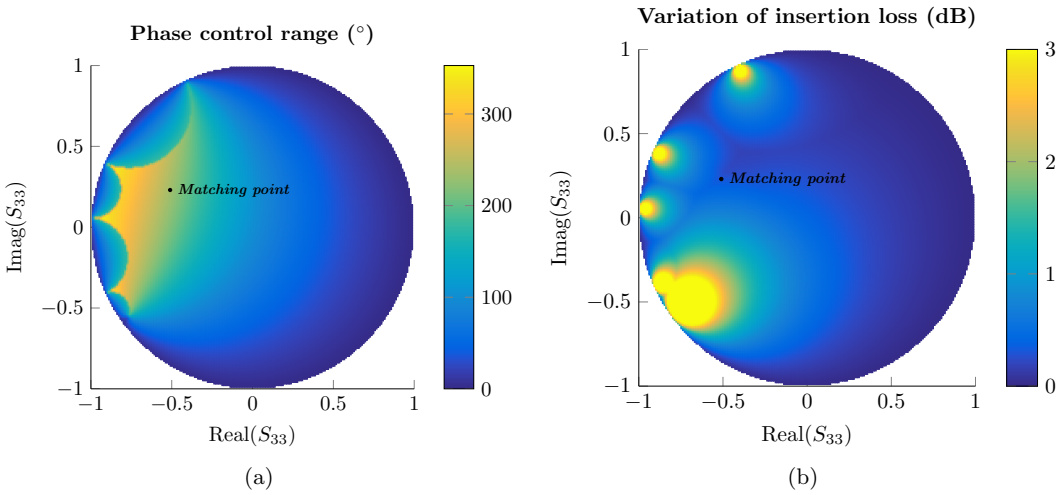


(a) (b)

Figure 4.13: Effects of various matching networks at 9 GHz for different fixed-capacitors. $S_{33}$ is referenced to 50 Ω. (a) Phase control range. (b) Insertion loss variation due to different matching points.

| $a_{siw}$ | $p_{siw}$ | $d_{siw}$ | $s_1$ | $s_2$ | $l_s$ | $w_s$ | $\Phi$ |
|---|---|---|---|---|---|---|---|
| 13.6 | 1.3 | 0.8 | 1.74 | 3.79 | 7 | 0.7 | 29 |
| $w_f$ | $w_l$ | $w_r$ | $l_{l1}$ | $l_{l2}$ | $l_{l3}$ | $l_{r1}$ | $l_{r2}$ |
| 0.2 | 2.5 | 2.5 | 2.4 | 2.6 | 0.6 | 1.79 | 0.2 |

Table 4.2: Design values of the measured loaded tilted slots SIW phase shifter with different capacitors according to Fig. 4.11. All measures in mm except Φ, which is in degrees.

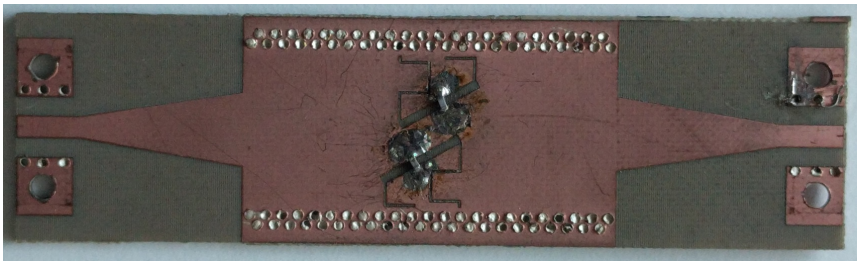

Figure 4.14: Tilted loaded slots SIW phase shifter prototype with different capacitors.

insertion loss. The design values are shown in Table 4.2, and the manufactured circuit in Fig. 4.14. While the slots take up all the SIW width, they only occupy 7.86 mm in length, which equates to $0.17 \cdot \lambda_{guide}$ at the center frequency. Comparatively, a typical RTPS would require double the width for the adjacent transmission line and a $1.2 \cdot \lambda_{guide}$ length for the hybrid coupler alone [89].

Full-wave simulations and circuit measurements at 9 GHz are shown in Fig. 4.15. The resulting phase agility is of roughly 240° in both cases. There is a noticeable difference at 0.5 pF, which can be attributed to a slight misalignment in the placement of the capacitors

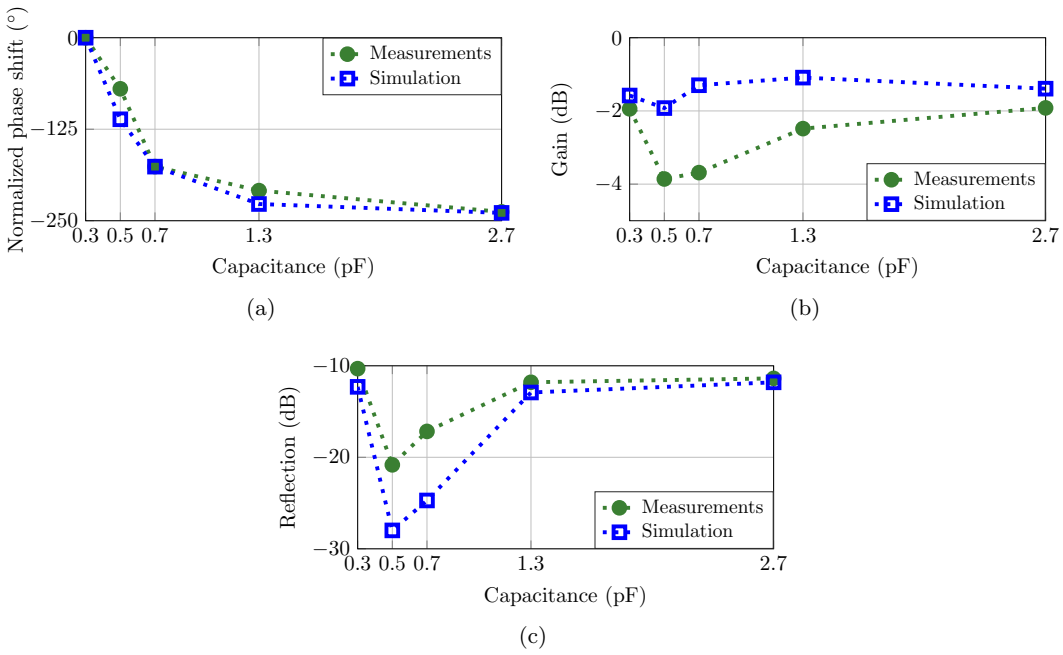


Figure 4.15: Comparison between measurements and simulations of the tilted load slots SIW phase shifter with different capacitors. (a) Phase shift. (b) Gain. (c) Reflection.

and the effect of the capacitance tolerance at what seems to be a more sensitive resonance. The same cause can be attributed to the increase of insertion loss variation from 0.8 in the simulations to 2 dB in the measurements.

At other frequencies the measured phase agility is as expected but with a slightly reduction in bandwidth, while there is an increase of variation of insertion loss in all cases (Fig. 4.16). The measured reflection coefficient does not show the pole at 9.4 GHz, but it is at similar level at other frequencies, with enhanced matching above 9.5 GHz.

#### 4.3.3.2. Varactor-tuned design

Next, the capacitors were replaced with the Aeroflex MGV-125-25-0805-2 varactor. Since the varactors will not be soldered to a ground plane access via-holes as in Chapters 2 and 3, a series model was realized to characterize only the varactor and its packaging parasitics, resulting in the impedances displayed in Table 4.4. The circuit was optimized with HFSS for matching $Z_T = 33.15 - 46.1j\,\Omega$, which should yield a phase agility of around 160° while maintaining a variation of insertion loss below 2 dB at 9 GHz, as indicated in Fig. 4.17.

The design values are shown in Table 4.3 and the manufactured circuit in Fig. 4.18. In this case, the phase shifter only takes up 5.37 mm in length, or $0.116 \cdot \lambda_{guide}$ at the center frequency. Two additional slots where etched between each slots to isolate the bias DC voltage. Two DC blocks capacitors were placed on top of them, and a wire was soldered from the patch between the two slots to an external patch in order to provide the reverse voltage that polarizes the varactors.

The measurements at 9 GHz (Fig. 4.19) show a increase in phase agility from 160 to 180°, which unfortunately also corresponds to an increase in variation of insertion loss

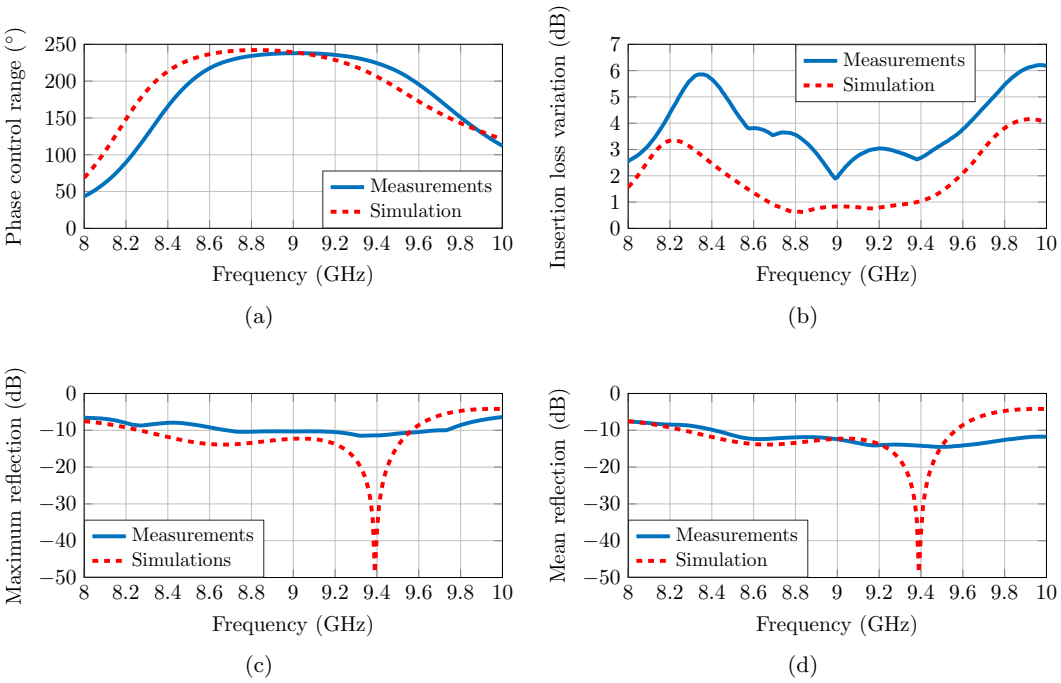


Figure 4.16: Bandwidth comparison between measurements and simulations of the tilted load slots SIW phase shifter with different capacitors. (a) Phase shift control range. (b) Insertion loss variation. (c) Maximum reflection. (d) Mean reflection.

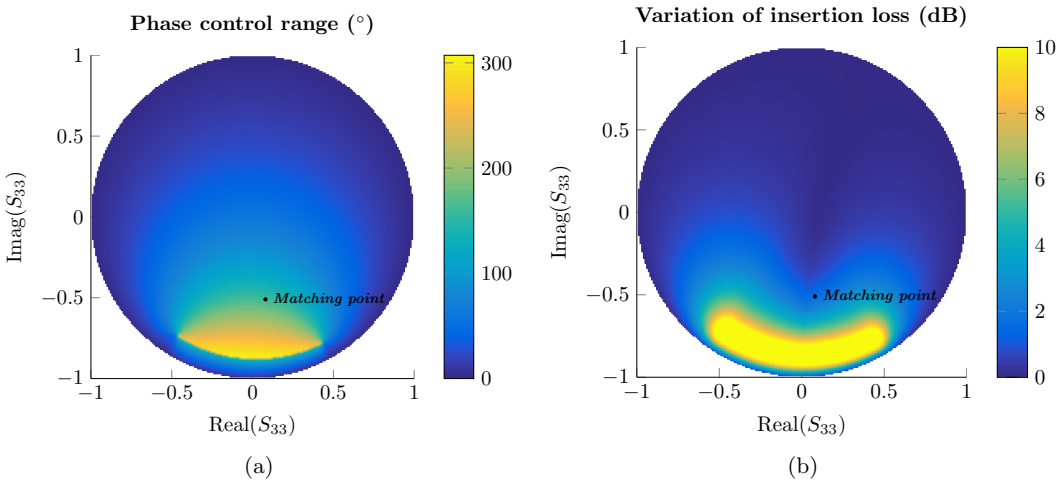


Figure 4.17: Effects of various matching networks at 9 GHz for the varactor. $S_{33}$ is referenced to 50 Ω. (a) Phase control range. (b) Insertion loss variation due to different matching points.

from 1.7 to 2.9 dB. This disagreement is due to various factors: parasitic effects from DC blocks and bias wire, capacitance tolerance (as documented by the manufacturer) and misalignment when soldering the varactors. In any case, the return losses are well above 10 dB. The offset in phase agility and variation of insertion loss notwithstanding, the response in the 8 to 10 GHz bandwidth (Fig. 4.20) shows good agreement between

| $a_{siw}$ | $p_{siw}$ | $d_{siw}$ | $s_1$ | $s_2$ | $l_s$ | $w_s$ | $\Phi$ |
|---|---|---|---|---|---|---|---|
| 13.6 | 1.3 | 0.8 | 1.1 | 2.48 | 5.8 | 1 | 44.4 |
| $w_f$ | $w_l$ | $w_r$ | $l_{l1}$ | $l_{l2}$ | $l_{l3}$ | $l_{r1}$ | $l_{r2}$ |
| 0.2 | 1.8 | 0.5 | 2.7 | 2.9 | 0.87 | 0.18 | 0.9 |

Table 4.3: Design values of the measured loaded tilted slots SIW phase shifter with varactors according to Fig. 4.11. All measures in mm except Φ, which is in degrees.

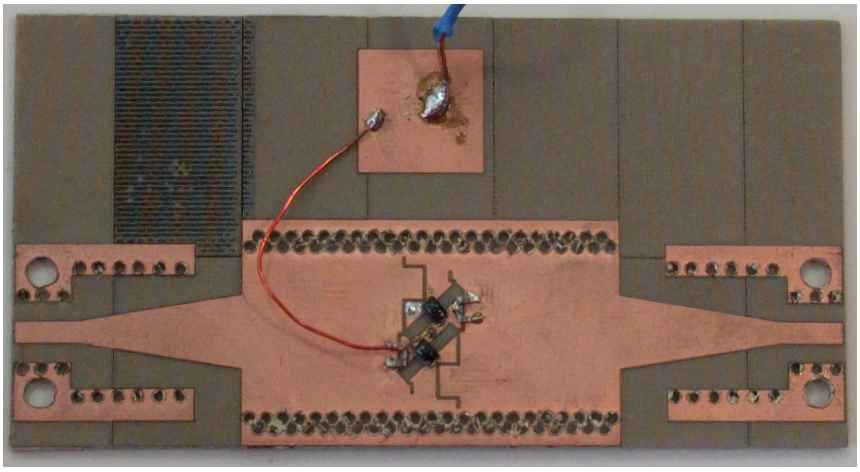

Figure 4.18: Tilted loaded slots SIW phase shifter prototype with varactors.

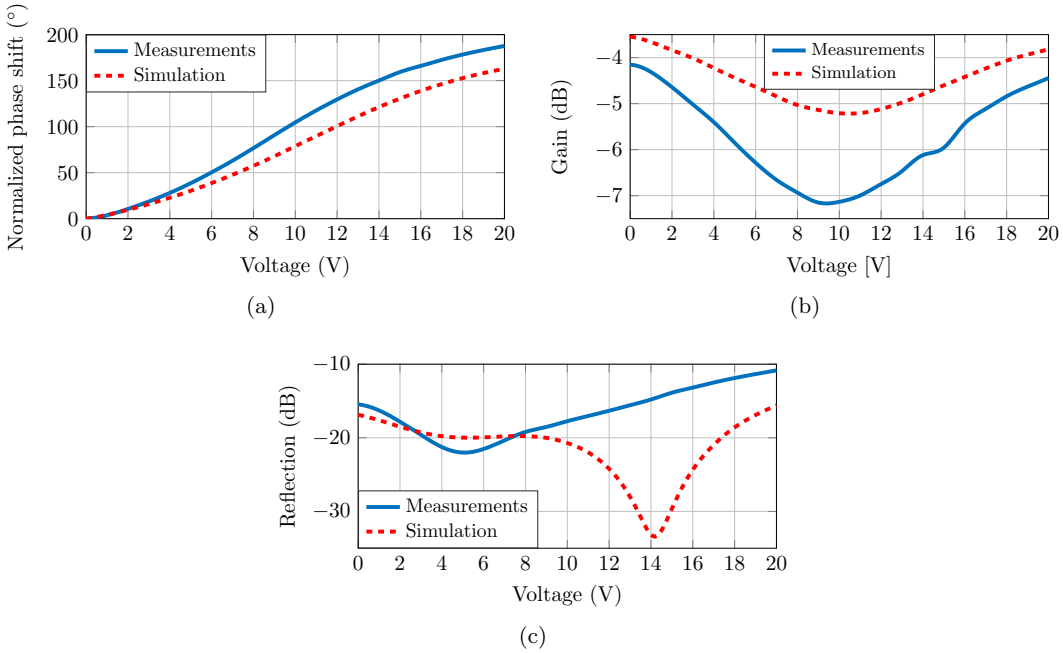


Figure 4.19: Comparison between measurements and simulations of the tilted load slots SIW phase shifter with different varactors. (a) Phase shift. (b) Gain. (c) Reflection.

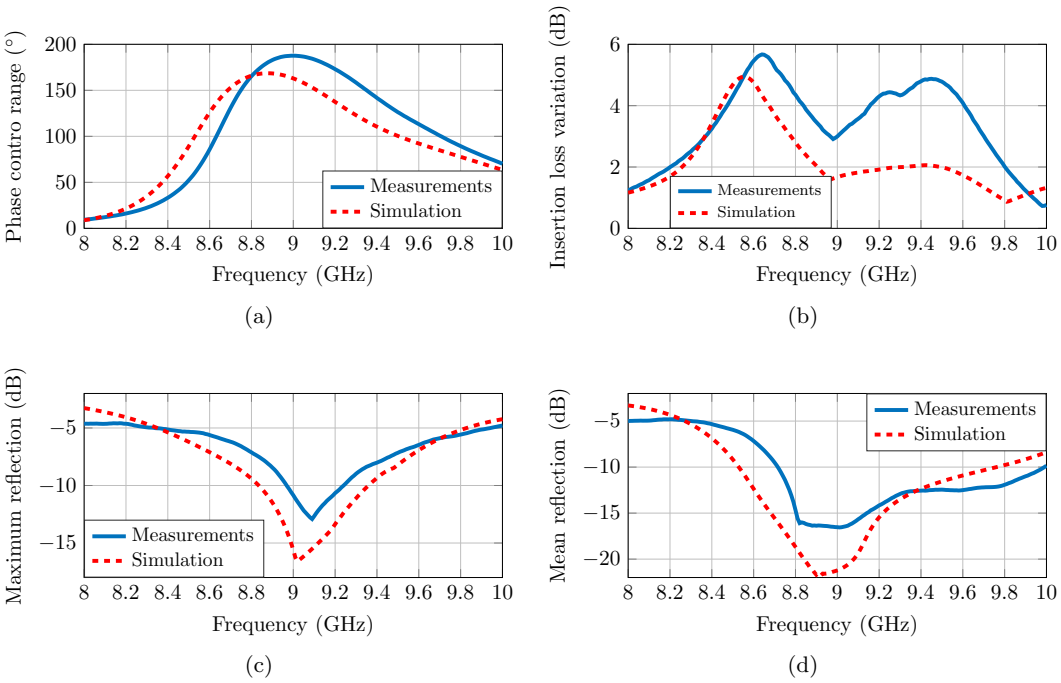


Figure 4.20: Bandwidth comparison between measurements and simulations of the tilted load slots SIW phase shifter with varactors. (a) Phase shift control range. (b) Insertion loss variation. (c) Maximum reflection. (d) Mean reflection.

simulation and measurements. The maximum reflection bandwidth is small due to an increased reflection at 20 V, consequence of the same causes that produce the increase of insertion loss variation. The mean reflection is a better representation of how it affects the bandwidth. From 8.72 to 9.35 GHz, the mean reflection is below -10 dB, the phase control range above 150° and the insertion loss ripple below 5 dB, which constitutes a 7% bandwidth.

In conclusion, the performance of the SIW phase shifter is close to the previously discussed RTPS based on microstrip technology, albeit it is more sensitive to maladjustment of the position of the varactors. Thanks to the novel topology, the circuit size is an order of magnitude below what is found in the literature, making it ideal for array integration. Subsequently, all the individual elements for making an array lens cell, as in Fig. 4.1, are designed an tested. Combining them in a single structure is the final step.

## 4.4. Tunable array lens cell

### 4.4.1. Fixed cell analysis

Thanks to the guided-way approach, a fixed cell can be optimized independently, so that the phase shifter may be incorporated later. As it was proven in Chapter 3 with the reflectarray, the Floquet modes analysis of HFSS is a reliable tool for optimizing the coupling of the radiation element to a waveguide in infinite periodicity conditions and

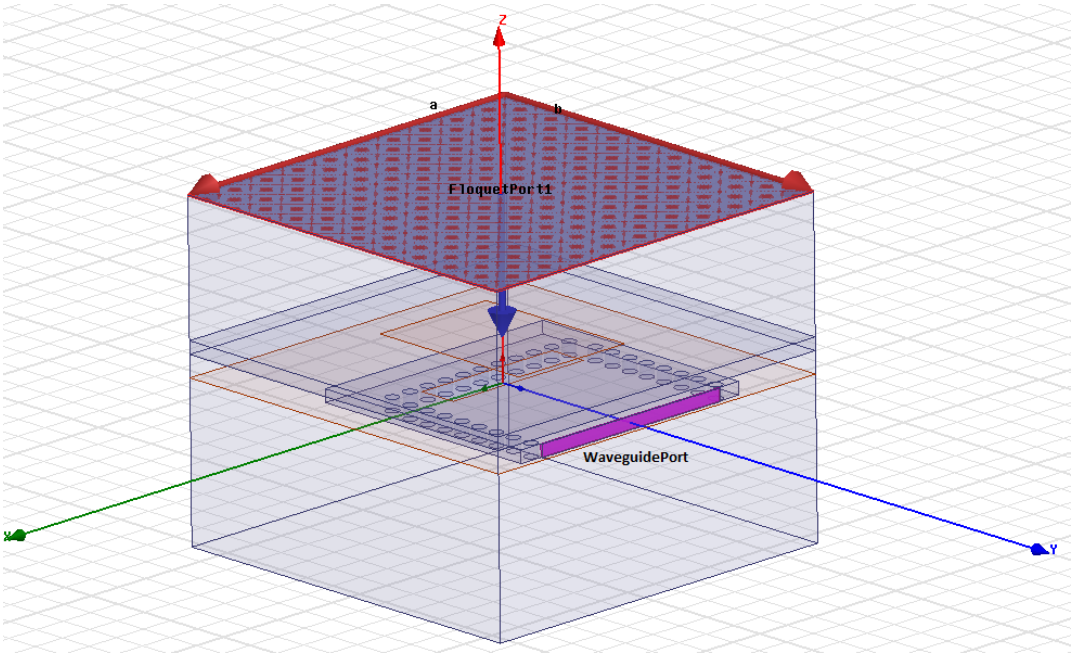


Figure 4.21: Floquet analysis set-up with HFSS of the fixed array lens cell.

for different incidence angles of the impinging wave. Due to the symmetry of the array lens (see Fig. 4.1), only one half (which could be seen as either the receiving or the transmitting end) needs to be simulated. One Floquet port represents the incident or outgoing wave, and a waveguide port receives or excites the $TE_{10}$ mode in the SIW. That way, the transverse slot design from Fig. 4.7 is optimized, using the set-up from Fig. 4.21. The conversion of the parameters from the Floquet modes $TE_{00}$ and $TM_{00}$ to $x$ and $y$ polarization is the same as in Eq. (3.6), but with the microstrip mode replaced with the $TE_{10}$ mode from the SIW.

For a $0.7\lambda$ element spacing at 9 GHz and at a normal incidence angle, the fixed cell was optimized for the SIW used in the phase shifter, with a transverse slot of 2.35 mm width and 9.56 mm length, and a patch of 7.8 mm width and 10.47 mm length.

| **Bias voltage (V)** | 0 | 1 | 2 | 3 | 4 |
|---|---|---|---|---|---|
| **Diode impedance (Ω)** | 11.118 +84.585j | 10.693 +81.891j | 10.239 +78.566j | 9.72 +75.211j | 9.29 +71.809j |
| **Bias voltage (V)** | 5 | 6 | 7 | 8 | 9 |
| **Diode impedance (Ω)** | 8.844 +68.446j | 8.373 +65.082j | 7.981 +61.751j | 7.624 +58.444j | 7.215 +55.185 |
| **Bias voltage (V)** | 10 | 11 | 12 | 13 | 14 |
| **Diode impedance (Ω)** | 6.878 +51.944j | 6.567 +48.879j | 6.246 +45.878j | 5.956 +42.971j | 5.693 +40.193j |
| **Bias voltage (V)** | 15 | 16 | 17 | 18 | 19 |
| **Diode impedance (Ω)** | 5.46 +37.604j | 5.279 +35.143j | 5.091 +32.934j | 4.916 +30.881j | 4.79 +29.08j |
| **Bias voltage (V)** | 20 | | | | |
| **Diode impedance (Ω)** | 4.677 +27.436j | | | | |

Table 4.4: Varactor diode impedance of the series model for different bias voltages.

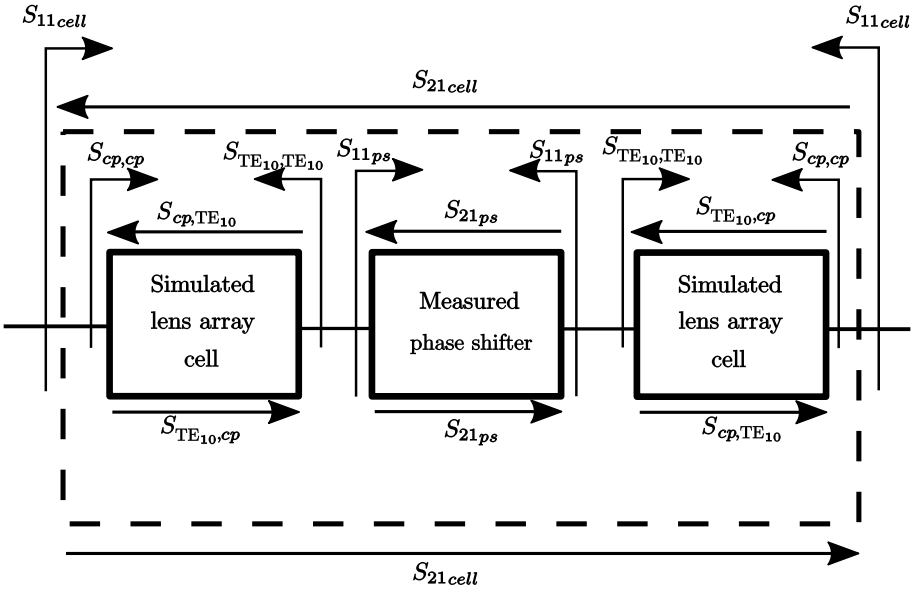


Figure 4.22: Schematic of the scattering parameters analysis for evaluating performance of tunable array lens unit cell.

### 4.4.2. Phase shifter integration

One advantage of the array lenses over the reflectarrays is that the feeding antenna is usually located directly above the array center (Fig. 3.7), since it cannot block the phased-corrected wave, which is transmitted on the other side. Due to this, the variation of $\theta_{inc}$ will be smaller for the same distance and array size. Besides, since the array lens is transmitting the signal and not reflecting it, it is less sensitive to the matching changes produced by different incidence angles, and so the performance should not drastically change unless the mismatchings were grave. This can be evaluated by cascading the simulation of the fixed cell with the phase shifter and the same simulation matrix with the ports reversed, as indicated in Fig. 4.22. Since the SIW phase shifter is symmetric, it is obtained that the reflection coefficient of the cell at both ports is

$$S_{11cell} = \frac{S_{cp,cp}\, {S_{\mathrm{TE_{10}},\mathrm{TE_{10}}}}^2 \left({S_{11ps}}^2 - {S_{21ps}}^2\right) + S_{cp,cp} \left(1 - 2\, S_{\mathrm{TE_{10}},\mathrm{TE_{10}}}\, S_{11ps}\right)}{1 + {S_{\mathrm{TE_{10}},\mathrm{TE_{10}}}}^2 \left({S_{11ps}}^2 - {S_{21ps}}^2\right) - 2\, S_{\mathrm{TE_{10}},\mathrm{TE_{10}}}\, S_{11ps}} + \\ + \frac{S_{cp,\mathrm{TE_{10}}}\, S_{\mathrm{TE_{10}},cp} \left(S_{\mathrm{TE_{10}},\mathrm{TE_{10}}}\, {S_{21ps}}^2 - S_{\mathrm{TE_{10}},\mathrm{TE_{10}}}\, {S_{11ps}}^2 + S_{11ps}\right)}{1 + {S_{\mathrm{TE_{10}},\mathrm{TE_{10}}}}^2 \left({S_{11ps}}^2 - {S_{21ps}}^2\right) - 2\, S_{\mathrm{TE_{10}},\mathrm{TE_{10}}}\, S_{11ps}}, \tag{4.2}$$

and the transmission coefficient, which corresponds to the phase-corrected wave, is defined by

$$S_{21cell} = \frac{S_{cp,\mathrm{TE_{10}}}\, S_{\mathrm{TE_{10}},cp}\, S_{21ps}}{1 + {S_{\mathrm{TE_{10}},\mathrm{TE_{10}}}}^2 \left({S_{11ps}}^2 - {S_{21ps}}^2\right) - 2\, S_{\mathrm{TE_{10}},\mathrm{TE_{10}}}\, S_{11ps}}, \tag{4.3}$$

where *cp* stands for the antenna co-polar mode and $TE_{10}$ for the SIW propagating mode.

Using Equations (4.2) and (4.3), in conjunction with the fixed cell simulation and the varactor-tuned SIW phase shifter measurements, the behavior of each cell can be

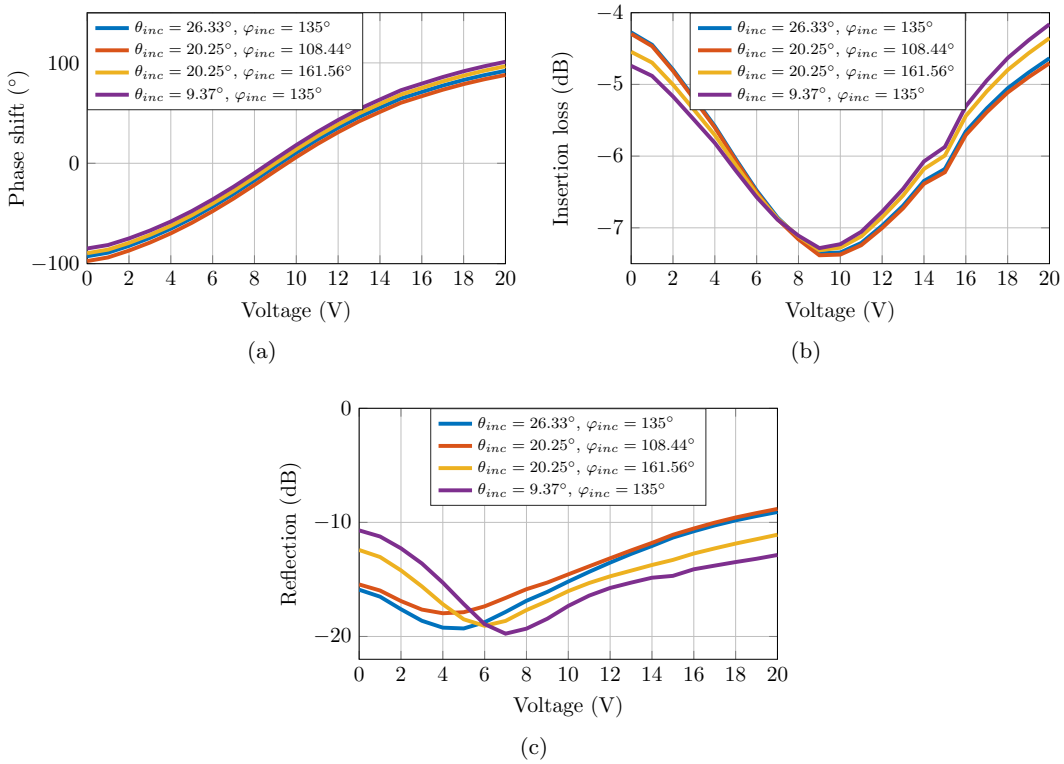


Figure 4.23: Simulation of the tunable array lens unit cell at different incidence angles with the measured SIW phase shifter. (a) Phase shift. (b) Gain. (c) Reflection.

characterized for a $4 \times 4$ array with $0.7\lambda$ element spacing, with the feeding antenna placed 100 mm away in the propagation direction. The four quadrants of the array share the same incidence angles since the feed is centered, and therefore only one quarter of the cells need to be analyzed. It is demonstrated in Fig. 4.23 how, despite having optimized the cell for only the normal incidence and having some mismatching, there is little variation in gain and phase shift (variation of less than 14°), confirming how the array lens configuration is less affected by small changes of impedance.

Regardless, this analysis presumes that the SIW phase shifter does not have its properties altered by the patch antennas, and that it performs exactly has measured.

The phase shifter can be located on each of the two plates of electrical conductor of a SIW indistinctly. However, the proximity to an electrical conductor may produce coupling and disturb the electric field on the slots, changing the expected phase shift range and insertion loss. This is a possible scenario when the patch antenna is on the same side as the phase shifter, and inevitably in the array lens, since there will be patch antennas on both sides. Running a HFSS simulation of the SIW phase shifter integrated in the lens unit cell permits to anticipate the effects of the proximity of the radiating patch. The simulations results are presented in Fig. 4.24. When the phase shifter slots are on the opposite side to the patch, it behaves normally (it is shielded by the metallic wall of the other side of the SIW). When it is on the same side and directly below it, the phase shift range greatly decreases, and so worsens the insertion loss and matching. If it

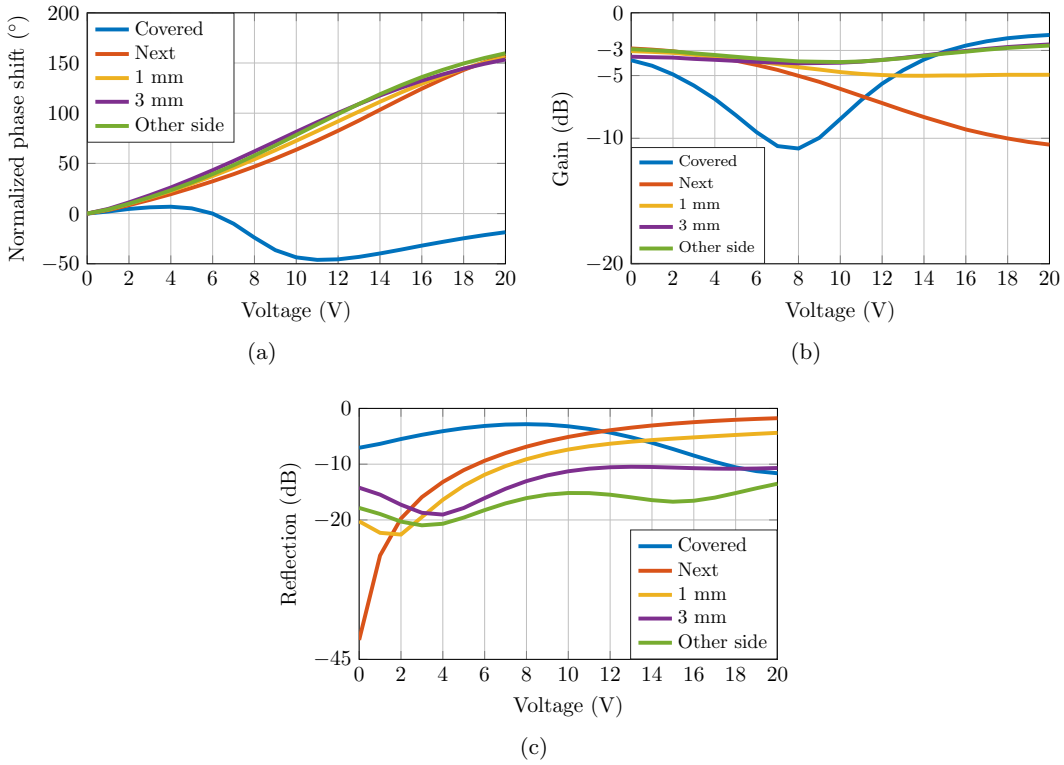


Figure 4.24: Comparison between measurements and simulations of the tilted load slots SIW phase shifter with different varactors. (a) Phase shift. (b) Gain. (c) Reflection.

is next to the patch (lengthwise), the phase shift is slightly affected but conserving the same range, whilst the insertion losses and matching worsens significantly. As the slots are more separated from the patch, the insertion losses and matching get closer to the performance of the unaltered phase shifter. For instance, with a separation of 3 mm the matching already yields return losses above 10 dB and the insertion loss variation is near optimal.

### 4.4.3. Unit cell design

The lens unit cell consists of two radiating patch antennas, which are communicated through coupling to a SIW that has transverse slots etched on each layer of electrical conductors to that effect. Between the two transverse slots, a SIW phase shifter is located. The main restriction is the proximity to a patch antenna: it should be far enough to ensure proper performance. Besides this limitation, there can be space for more than one phase shifter, depending on the element spacing. The possibility of adding a phase shifter on the other side of the SIW may be exploited to avoid the proximity to a patch antenna and still have two cascaded phase shifters. Fig. 4.25 shows the lens cell design with one or two cascaded phase shifters fitting narrowly between the transverse slots. No substrate should be above the phase shifters so there is enough vertical space to solder the varactors. More space could be freed by using a substrate with higher permittivity for the patch antennas, diminishing their size and so allowing to reduce the element spacing.

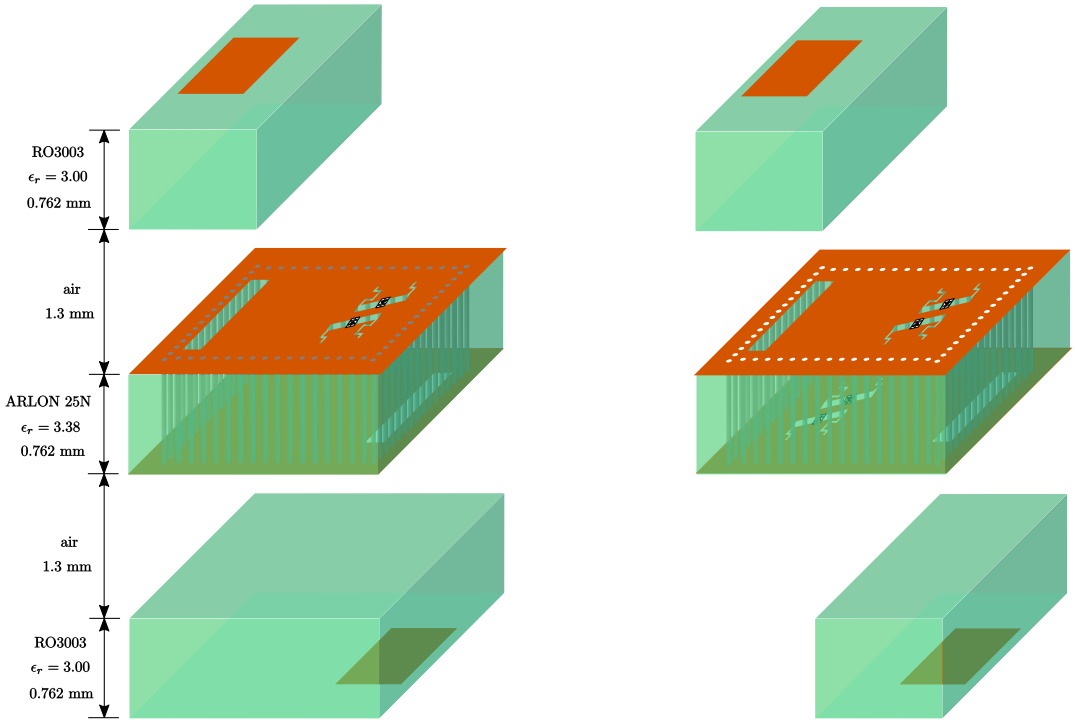


Figure 4.25: Tunable array lens cell design. (a) One SIW phase shifter. (b) Two SIW phase shifters.

The design with one phase shifter was used to simulate a $2 \times 2$ array lens, with $0.7\lambda_0$ element spacing at 9 GHz, with the feeding $2 \times 2$ array included in the simulation, depicted in Fig. 4.26. Due to the via-holes structure of the SIW requiring a lot of computation power, a bigger array was not simulated. The ground plane of the patches which receive the wave from the feed is considered infinite as to completely block the impinging wave, eliminating it from the simulation results. By changing the impedance of the loads on the slots to the corresponding varactor impedance for each bias voltage, beam scanning can be performed, which follows the same phase correction as in Eq. (3.9).

Due to the small size of the array is it not possible to achieve a discernible wide range of beam steering. The simulations were performed for a beam scan between $-10°$ and $10°$ in both azimuth and elevation. The results are plotted in Fig. 4.27. They validate the approach taken for simulating the unit cell and how to integrate the phase shifter without altering its properties.

### 4.4.4. Prototype

Each cell needs to have two varactors and DC blocks soldered accurately, which is a laborious task due to the small size of tilted slots. Besides, a RF choke should be soldered from the center of the SIW phase shifter to the bias circuitry, to avoid unwanted resonances. This makes manufacturing a sizeable array time consuming and needing much more components that the presented reflectarray. Subsequently, a small $2 \times 2$ array lens

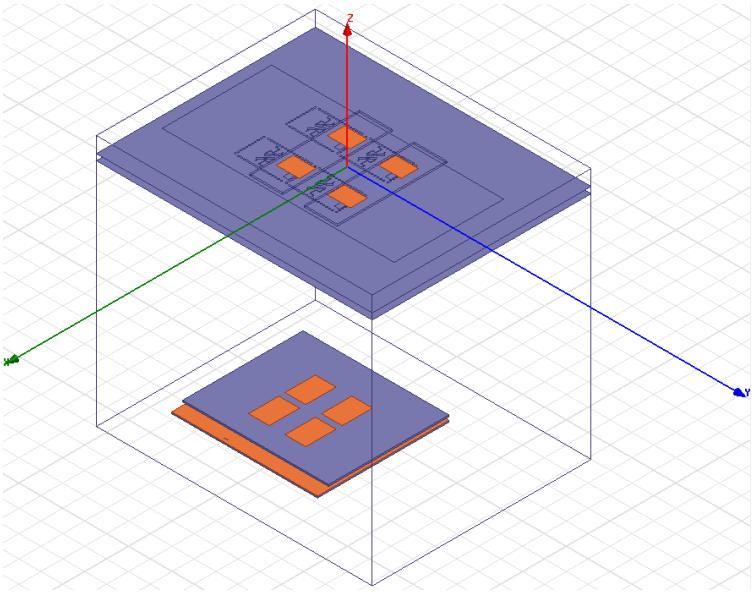


Figure 4.26: Simulation set-up of the $2 \times 2$ array lens with infinite ground.

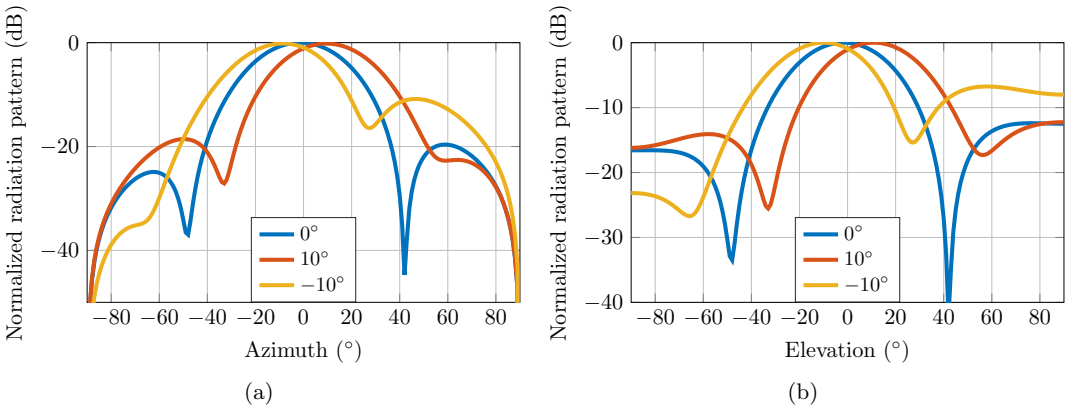


Figure 4.27: Simulation of the beam steering of a $2 \times 2$ array lens with infinite ground. (a) Azimuth. (b) Elevation.

was manufactured, displayed in Fig. 4.28.

It is not possible to correctly realize beam scanning due to the small number of elements, since the lens is as directive as the feeding antenna and there is low spill-over efficiency, resulting impossible to block the radiation from the feed. Instead, the beam that is produced when there is no voltage biasing the varactors is corrected to point at broadside when applying the voltages for a $-45°$ beam steering in azimuth. The non-biased beam is misaligned in the first place due to the offset existing between the receiving and transmitting layers, with the feeding antenna centered on the first. The measurements set-up is the same as in the reflectarray, but this time with the feeding antenna being screwed onto the rotating pole (Fig. 4.29). The results are showcased in Fig. 4.30. The differences between simulations and measurements are due to the use of an infinite perfect electric conductor in the simulation, shielding the spill-over from the feeding antenna.

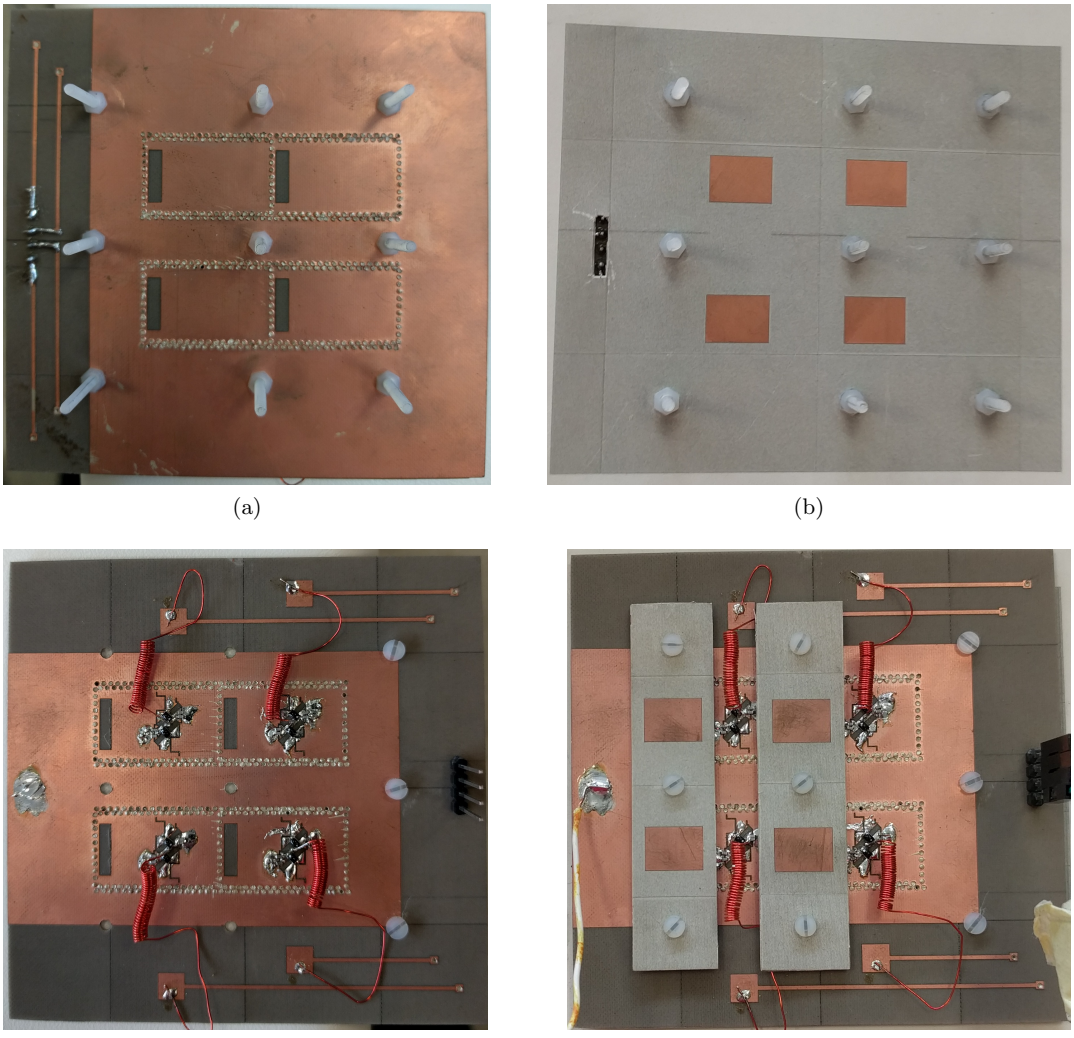

(a) (b)

(c) (d)

Figure 4.28: Picture of the manufactured array lens. (a) Slots of the incident side. (b) Patch antennas of the incident side. (c) Slots and phase shifters of the transmitting side. (d) Patch antennas of the transmitting side.

However, this results do not validate experimentally the beam steering capabilities of the array lens. It would be necessary to manufacture an array with higher number of elements. Another possible validation would be the measuring of the unit cell inside a rectangular waveguide, thus replicating periodicity conditions.

## 4.5. Conclusions

The array lens has two radiating layers, one on which the wave of the feeding antenna impinges, and another which radiates the phase-corrected wave. In the guided-wave approach, a phase shifter needs to be inserted between them. The phase shifters discussed in Chapters 2 and 3 were made in microstrip technology, which does not lend itself easily for coupling between two different layers, requiring additional elements such as extra mi-

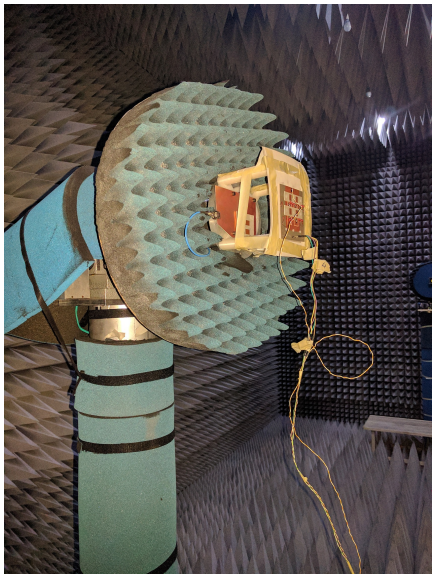

Figure 4.29: Anechoic chamber set-up for the array lens measurements.

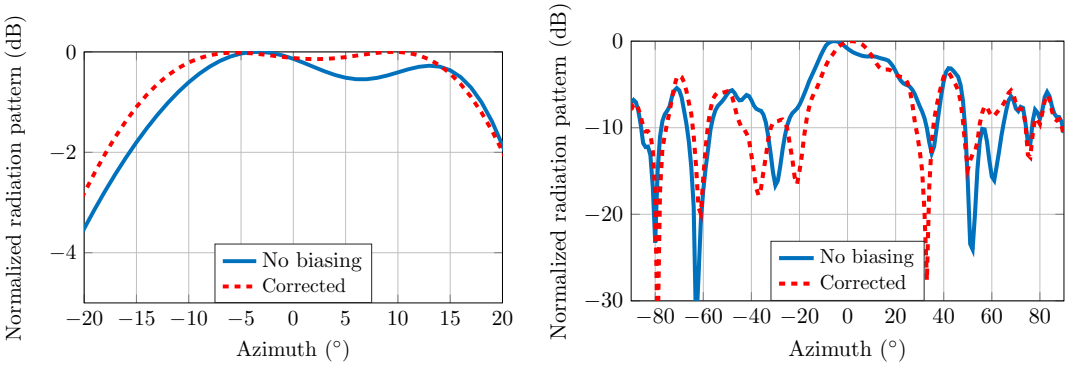


Figure 4.30: Radiation pattern of the $2 \times 2$ array lens. (a) Simulations. (b) Measurements.

crostrip patches. A possible solution consists in realizing a 90° change of reference plane, thus having the coupling and phase shifting in different planes. This, however, makes the manufacturing process more complicated, increases insertion losses and causes the structure to be more fragile. Besides, the presented reflective-type phase shifter works better in a reflection configuration, that is, when the signal is reflected at the input port. If not, two or more phase shifters needs to be cascaded for increasing the phase agility, and thus doubling the chip footprint.

The substrate integrated waveguide technology allows to obtain a structure equivalent to a rectangular waveguide but with the benefits of ease of manufacture and low costs of planar technology. It easily couples to two different layers maintaining just a single waveguide, without having to add extra elements. The use of a transverse slot etched on whichever side of the SIW was revealed to be the most efficient solution for coupling to a radiating patch due to the small space required, favoring the use of smaller element

spacings. Nevertheless, the SIW phase shifters present in the literature require the use of parallel waveguides, producing a big chip size and offering little control of their performance.

Instead of employing a hybrid coupler for realizing a RTPS, a new structure was proposed using tilted slots loaded with tunable impedances. This structure acts as an impedance transforming hybrid coupler but greatly reduces its size due to being composed only of the slots. The performance is controlled in the same way, by matching the slots to an optimal complex impedance. A fixed capacitors phase shifter was designed and fabricated in the substrate Arlon 25N of $\epsilon_r = 3.38$ and thickness of 30 mil, where the capacitors are replaced to obtain different phase shifts. It achieved a 240° phase agility and 2 dB insertion loss ripple. The insertion loss has increased from the 0.8 dB observed in simulations due to misalignment in the soldering of the capacitors, which was performed manually. Most importantly, the slots only occupy 7.86 mm in length, which equates to $0.17 \cdot \lambda_{guide}$ at the operating frequency, 9 GHz. A phase shifter like the ones in the literature would have required twice the width and a $1.2 \cdot \lambda_{guide}$ length for the hybrid coupler. The improvement in that regard is prominent.

In the same conditions, a varactor-tuned phase shifter was designed and optimized. In order to isolate the DC biasing, slots where etched and covered with DC blocks, as to not disturb the normal operation of the SIW. The phase shifter takes up only 5.37 mm in length, and produces a phase agility of 180° with an insertion loss ripple of 3 dB. It is matched with return losses above 10 dB, with a phase control range of 150° and an insertion loss ripple below 5 dB for a 7% bandwidth. While the results do not produce a full phase control range, it would be easy to cascade another phase shifter due to its small size, and it could be optimized further in that configuration as it was shown in Chapter 2. It is capital though, to ensure that the phase shifter slots are not close to another radiating element, as it could interfere with the electromagnetic field of the slots. Simulations were carried out that determined that the phase shifter is unaltered when it is located in a different side than the radiating element, but the insertion losses are affected when it is too close if on the same side.

The periodicity conditions of the unit cell were simulated using the Floquet mode analysis of HFSS. The cell consists of a transverse slot on each side of the SIW, for coupling to patch antennas located on top of each other, with the phase shifter between them, while leaving enough space between the tilted slots and the patch antennas as to not interfere with the performance of the phase shifter. With a cell optimized for a normal incident angle, the effects of increased incident angles were shown to not be as severe as with the reflectarray. Paired with the fact that a centered feeding antenna produces less variation of incidence angles, it makes the lens array much easier to optimize than the reflectarray.

A $2 \times 2$ lens array with infinite ground was simulated, obtaining beam scanning from $-10$ to 10° in both azimuth and elevation. The scan could not be wider due to the small number of elements and the required computation power for simulating a bigger lens array. Due to manufacturing complexities, a prototype of only $2 \times 2$ elements was fabricated. Its

size is not enough to realize proper beam steering, and so only a small correction of the main beam for broadside radiation was realized. The manufacturing of a bigger lens array or the measurement of a unit cell inside a waveguide for replicating infinite periodicity conditions should be performed to obtain better experimental validation.

CHAPTER 5

# Conclusions and future research lines

## 5.1. Final conclusions

This thesis has been dedicated to the study of reconfigurable reflectarray and array lens antennas, particularly those employing the guided-wave approach, that allows to perform a modular analysis, optimizing separately the radiating element and the phase shifter. The continuous phase shifters offer the most reconfigurability, but they are specially constrained by limitations in phase agility, insertion losses and circuit footprint, which this thesis aimed to overcome, offering more control over their performance.

In a reflection-type phase shifter (RTPS), a single tunable load does not yield a 360° phase control range, and has to be increased through solutions that offer no performance control or require costly monolithic circuits. An alternative solution has been presented with the addition of passive matching networks, which can be realized with stubs and transmission lines. By matching the tunable loads to complex impedances, it is possible to alter the phase shifter performance for different pairs of phase control range and insertion losses. A model of the commercial varactor Aeroflex MGV-125-25-0805-2 was made at 9 GHz to analyze the effect that every possible matching network would have on its phase shifting performance. It was observed that the matching points that provide the highest phase agility always correlated with the highest insertion losses. However, there are matching impedances which offer a good trade-off between phase and losses. It was also observed a correlation between low insertion loss ripple and phase linearity. From the initial phase range of 55° that the varactor yields, a 160° phase range can be achieved without significantly affecting the insertion losses. A further increase to 210° can be obtained with an insertion loss variation below 3 dB. This solution is, however, marred by the increase in chip size: not only a hybrid coupler is needed, but also the implementation of the impedance matching networks. To overcome this problem, the impedance matching should be performed within the hybrid coupler structure.

Impedance matching 90° hybrid couplers are restricted to real impedances and are

severely limited by the realizability of the required impedance of their transmission lines. This thesis establishes that by adding lines of arbitrary impedance and length at each port, it is possible to increase the range of impedances to which they can be matched. An even-odd analysis of the structure defines the value of the impedance and length of each of the composing transmission lines for obtaining the desired impedance matching at each port with different coupling coefficients. Nevertheless, it is impossible to match imaginary impedances, and the bigger the imaginary component of a complex impedance, the wider the range of impedances that will be needed to implement the transforming hybrid coupler.

By optimizing the impedances of the added transmission lines and deriving the rest of the values from the equations obtained from the even-odd analysis, a design procedure is constituted. This procedure was used to design and manufacture hybrid couplers in microstrip technology at 2 GHz with a reference impedance of $50\,\Omega$. One prototype is matched to a $Z_T = 450\,\Omega$, which is a real impedance matching which would not have been possible without this new topology due to the low line widths that are necessary to accomplish it. Another prototype matching to a $Z_T = 70 - 200j\,\Omega$ was manufactured, showing excellent agreements between measurements and simulations. A further optimization of the hybrid coupler can be performed if the ports corresponding to the reference impedance are not perfectly matched, but are instead matched to a complex impedance that still produces low reflection. That way, the length of the transmission lines corresponding to those ports can be trimmed. Another prototype corresponding again to a matching to $Z_T = 70-200j\,\Omega$ was realized, but this time with the improvements in circuit size through the matching to a complex $Z_0 = 50 - 20j\,\Omega$, even though the measurements would still be referenced to $50\,\Omega$. The results show no decline in performance when compared to the hybrid coupler previously realized, achieving a net gain in circuit size –an area reduction of 25%– without disadvantages.

Then, the complex impedance transforming hybrid couplers can be used as a RTPS when the matching impedance $Z_T$ is chosen as the one corresponding to the desired performance of the phase shifter according to the analysis of the tunable load. By matching a hybrid coupler to $Z_T = 30 - 57j\,\Omega$, a phase shifter was manufactured at 9 GHz with the commercial varactor Aeroflex MGV-125-25-0805-2 and the substrate Arlon 25N, of electrical permittivity $\epsilon_r = 3.38$, obtaining a phase shift range of 180.3° with insertion losses from 3.3 to 5.5 dB, and with a chip size 60% smaller than the circuit that would be realized with a normal hybrid coupler with added impedance matching networks at each port for same performance. The phase agility is above 150° in a 10% bandwidth, while the insertion loss variation remains under 3 dB in a 20% bandwidth.

Better trade-offs between phase agility and insertion loss ripple could be achieved if the insertion losses were equalized. The solutions found in the literature require the use of lumped inductances, whose packaging parasitics would pose a problem when optimizing the phase shifter. The purpose of the inductances can also be achieved by properly fixing the length of the transmission lines in the transforming hybrid coupler corresponding to the ports where the tunable loads are located, ensuring that their electrical lengths performs

an impedance transformation in which the varactor makes the imaginary impedance go through a value of 0 somewhere near the middle bias-voltage. That way, the tunable load is seen as a structure made up of the transmission line and the varactor, and so the rest of the hybrid coupler can be studied as a real impedance matching hybrid coupler. Thus, new equations are obtained, relating the phase shifter performance to the real matching impedance of the hybrid coupler and the transformed impedance of the tunable load. It is observed then, that the insertion losses can be equalized by placing a parallel resistance that increases the real impedance of the transformed load at some biasing points. That is, the insertion losses increase, but they experience less variation. With a pure resistance, the insertion loss ripple at 9 GHz is decreased to 0.3 dB while obtaining a 180° phase agility. A prototype was manufactured obtaining such phase range, but with insertion losses from 4.4 to 5.6 dB (1.2 dB ripple), with such an increase due to the parasitics from the resistor packaging. The circuit is matched with return losses above 10 dB for a 9.1% bandwidth, and presents an insertion loss variation below 1.5 dB and phase agility above 150° in a 9.8% bandwidth.

This thesis proposes an alternative approach of equalizing losses consists in designing non-balanced complex impedance transforming hybrid couplers; that is, with coupling coefficients different than 1. In those cases there will be some mismatching, consequence of the tunable loads not corresponding to the matching impedance and the reflected signal not canceling out at the input. This apparently detrimental characteristic may be employed to equalize the insertion loss when cascading phase shifters. While the phase range is doubled, the insertion loss ripple might experience a smaller increase. However, only a 0.5 dB minimization in loss variation was observed to be possible for a 320° phase range if a matching with return losses above 10 dB was to be kept. If matching were not a concern, a further reduction to 1.35 dB would have been possible, instead of the 2.5 dB loss ripple that would be obtained with balanced hybrid couplers.

Altogether, a extensive optimization of the RTPS was realized for employment in reconfigurable arrays, controlling the performance with the complex impedance matching, reducing the circuit footprint by designing a hybrid coupler that can match to different complex impedances and coupling coefficients, and equalizing insertion losses by adding parallel resistances or cascading phase shifters with different coupling levels. The actual guided-wave approach implementation requires, nevertheless, another aspects to consider.

In a guided-wave reflectarray, the main requirement is that the space-wave from the feed is converted into a guided wave and not reflected directly at the scatterer. The periodicity condition of the unit cell must be taken into account. An optimization of the geometry parameters of the unit cell is performed so that both the microstrip quasi-TEM mode and the combination of Floquet modes that correspond with the co-polar mode of the antenna are matched and being transmitted with low insertion loss. The definition of the Floquet modes depend on the incidence angle –the angle formed between the propagation vector of the space wave and the position of the array element, in $\theta$ and $\varphi$– but can always be expressed in $x$ and $y$-polarized modes, which facilitates the analysis. A unit cell was optimized at the normal incidence angle, and then the stub length of each cell

was individually optimized for realizing beamforming at broadside and at 45° in azimuth in a 4 × 4 fixed reflectarray. A prototype was manufactured in which, by changing the layer corresponding to the stubs, the two different beams are radiated. There is a good agreement between measurements and simulations, even when compared the expected radiation pattern from a ideal phased array, proving that the analysis of the unit cell was correctly performed.

Since the guided-wave in the reflectarray has to be reflected back to the scatterer, the RTPS has to be used in a single port fashion, where the input is also the output. That is, the signal is reflected back, thanks to an open-ended port, to the input port with a phase shift and insertion losses. However, the analysis previously performed assumed a two-port use. This requires a new definition of the phase shift performance where the matching of the RTPS is shown to affect the phase range and insertion losses. The previous matching restriction that affected the RTPS when the coupling was not balanced can be ignored, since the signal is going to be reflected in any case. Hence, a further optimization of the performance can be realized, obtaining the phase agility of cascaded phase shifters with insertion loss ripples below 1 dB with a single RTPS, showing to be an improved topology. In addition, a single parallel resistance can be placed at the input/output port for equalizing insertion losses. While this does not yield smaller loss ripples, it does improve the range of transforming hybrid couplers that might be used for achieving a given trade-off between phase agility and insertion losses, which in turn result in faster optimizations and more degrees of freedom in the design. A prototype was manufactured at 9 GHz in the substrate Arlon 25N, obtaining a 320° phase range with insertion loss from 3.4 to 5.2 dB, which is further reduced to a 1 dB ripple if a parallel resistor is employed. The phase agility is above 300° and the insertion loss variation below 4 dB in a 12.33% bandwidth, which is wider than that of a typical reflectarray. The chip footprint is small enough to fit an element spacing of 0.7λ, but it could be reduced if a substrate of higher electric permittivity would have been used.

This RTPS topology is, however, sensitive to changes in the port impedance. Small changes of impedance that would still considered to be well matched result in huge deviations in the phase agility (above 100°) and insertion losses. Since the unit cell was optimized only at the normal incidence angle, it raises the concern that its matching would be affected at other incidence angles, resulting in different phase shift behavior at each array element. A new optimization of the unit cell parameters was performed for ensuring excellent matching at every angle of incidence of the previously designed 4 × 4 reflectarray. Different unit cells would have to be used, dividing the array in sub-arrays, if the matching could not be obtained at every incidence angle. The fixed reflectarray did not pose this problem since each cell was individually tuned for achieving the required phase shift at each incidence angle, a luxury that is not possible when employing the RTPS, since it has a single design. With the newly optimized unit cell, simulations were performed with the RTPS measurements, obtaining a phase shift difference below 30° and insertion loss difference below 2.5 dB between cells.

A 4 × 4 tunable reflectarray was manufactured and measured in an anechoic cham-

ber, with separate biasing lines for each element. Each biasing line is controlled by the evaluation board of a 14 bits digital to analog converter, which is in turn governed by an Arduino board. Voltages were applied for performing beam scanning in azimuth and elevation, obtaining beam steering from $-10°$ to $30°$ in azimuth and from $-20°$ to $20°$ in elevation. The scanning range is limited by the small reflectarray size, since the gain diminishes as the main beam steers away from the specular reflection angle. Still, the reconfigurability is sufficiently demonstrated. The single-port RTPS topology has excellent performance and it stresses how important it is to take into account the different angles of incidence when designing a reflectarray.

The array lenses require two opposite radiating surfaces, which a waveguide-like structure has to communicate producing a phase correction. The use of microstrip technology would require extra patches –which would increase the element spacing since the circuit footprint should increase to accommodate for a patch in the same layer as the phase shifter– or a $90°$ change of plane of reference, which increases the array thickness, produces insertion losses, increases manufacturing complexity and results in a more fragile structure. Instead, the use of substrate integrated waveguide (SIW) is proposed. The SIW coupling to a patch antenna can be realized by shorting one end of the SIW with metalized via-holes, and etching a longitudinal or transverse slot, depending on the desired polarization direction. It was found that placing the transverse slot next to the short-circuit does not present any adverse effects, radiating as a typical patch antenna, and optimizing the circuit footprint by taking up less longitudinal space. Since the slots and patch antennas can be placed on whichever side (corresponding to the plates of electrical conductor) of the SIW indistinctly, it would be possible to receive the space wave from the feed antenna in one side, couple it to the SIW and transmit it to a patch antenna on the opposite side after performing the phase correction.

A direct translation from microstrip to SIW of the RTPS is not advisable. The SIW hybrid couplers require a lot of space due to having to fit different waveguides, which are much wider than the typical microstrip line. Besides, there is no equivalent method to control the performance of the tunable load to the same extent. A new structure is proposed instead, exploiting the unique characteristics of the SIW technology. By placing two tilted slots with a certain length, width and separation, with added interdigitated capacitors to better control their impedance, the hybrid coupler is replaced by a much smaller structure. The tunable loads are placed in the center of the tilted slots, and the whole structure acts as a reflection-type phase shifter: the $TE_{10}$ mode is split into a quasi $TE_{20}$ mode in which the electromagnetic fields are offset by $90°$. When the value of the slots geometry parameters are properly assigned, the scattering parameters analysis –with lumped ports placed where the tunable loads are to be located– yields a scattering matrix equivalent to that of a impedance transforming hybrid coupler. Hence, when loaded with the tunable slots it behaves in the same way as the traditional RTPS: the fields reflected from the slots back to the input port get canceled out due to being out of phase, and the fields reflected forth are summed up, recomposing the $TE_{10}$ mode with a phase shift and insertion losses dependent on the tunable load and the matching impedance of the slots.

Due to the novelty of the structure, a prototype using fixed capacitors was developed first. By soldering capacitors of various values on the slots, different phase shifts are obtained, with the prototype bestowing good agreement between measurements and simulations. Another prototype was then designed and manufactured using the varactor Aeroflex MGV-125-25-0805-2 as tunable load. To isolate the DC bias voltage, additional slots were etched, leaving an isolated area between the tilted slots. Those additional slots are covered with DC block capacitors, as to not harm the performance of the phase shifter. A cable is soldered to the DC isolated area for applying the bias voltage, which could also serve as RF choke to avoid any interference from the bias circuitry. The prototype, realized in the Arlon 25N substrate, yielded at 9 GHz a phase agility of 180°, with insertion losses from 4.15 to 7.15 dB (3 dB ripple). It has mean return losses above 10 dB, with a phase agility of 150° and an insertion loss variation below 5 dB for a 7% bandwidth. The loss variation is bigger and the bandwidth lower than expected from simulations, and slightly worse if compared with the previous RTPS in microstrip technology. It is attributed to a lack of accuracy when manually soldering the varactors, since it requires precision for soldering the components on the slots center, and the small space between the slots makes the task harder. In any case, the phase shifter is only 5.37 mm long, equating to a $0.116 \cdot \lambda_{guide}$ length. A SIW phase shifter comprised of a hybrid coupler would have required at least a $1.2 \cdot \lambda_{guide}$ length, besides increasing the width due to a parallel SIW. Despite minor shortcomings in the insertion loss, the size reduction when compared to the alternatives is most important. Even though a full phase control range was not obtained, it is easy to cascade another instance of the phase shifter due to its small size, being possible to locate it on the opposite layer of electrical conductor if so desired. However, the proximity to a radiating patch must be considered. If the tilted slots are too close to it, the performance of the phase shifter will be affected, especially the insertion losses. A distance of 3 mm was observed to be enough for achieving a performance close to optimal. It is also worth noting that the phase shifter is not affected by the patch in any case if it is located on the opposite plate.

The guided-wave matching of the array lens unit cell can be simulated in the same way as the reflectarray, by using Floquet mode analysis in HFSS, with the only change consisting in matching the co-polar mode to the $TE_{10}$ mode of a SIW instead of matching it to the quasi-TEM mode of a microstrip line. Furthermore, the array lens unit cell is shown to be less affected by the mismatching resulting from different angles of incidence. Even a unit cell optimized only for normal incidence shows little phase and insertion loss variation for different incidence angles. Coupled with the fact that the feeding antenna in an array lens is practically always centered, and thus the range of incidence angles is kept to a minimum, it is easier to optimize the guided wave approach for an array lens unit cell than for a reflectarray. The principal size restriction of the unit cell is the separation that must be maintained between the phase shifting slots and the radiating patches. However, this condition also makes possible the use of two cascaded phase shifters, placed on opposite plates, without affecting the element spacing at all.

The main problem with simulating an array lens based on SIW technology in HFSS is

the required computation power. Simulating a SIW phase shifter already requires much processing time due to the meshing of the metalized via-holes and the tilted slots, and it is much aggravated when the structure is periodically repeated, which also results in a less accurate simulation. Thus, only a $2 \times 2$ tunable array lens was simulated, with an infinite ground plane for completely blocking the wave from the feeding antenna and so taking it out of the radiation pattern results. A beam scanning from $-10°$ to $10°$ was obtained in both azimuth and elevation. Due to manufacturing difficulties, a small prototype of $2 \times 2$ was manufactured. Since there is low spill-over efficiency, the field radiated by the feeding antenna contaminates the measurements, and thus the beam steering cannot be obtained. However, it was found that by applying the voltages corresponding to a beam pointing to $\theta = -45°$, the measured beam can be corrected to point at broadside, displaying some tunability. While the results obtained from the SIW antenna and the SIW phase shifter are satisfactory, the reconfigurability of the array lens is not experimentally validated, and more work has to be done in that regard. Nevertheless, the presented work is of consequence as it constitutes the first proposal of a array lens in SIW technology.

## 5.2. Future lines of work

The work presented in this thesis can be extended in several ways, from immediate tasks following the conclusions at which were arrived, to longer-term research focusing on achieving more reconfigurability options in active antennas.

The reflection-type phase shifter from Chapters 2 and 3 are near the optimal theoretical point at the operating frequency. However, the bandwidth was not a factor in the analysis. There are many bandwidths improvements in the literature of hybrid couplers, including left-handed transmission lines [90], via-holes [91, 92], air-gaps [93], stubs [94], coupled [95, 96] and $\pi$ shaped lines [97]. These techniques should be looked into to ascertain how they can be combined with the transforming impedance capability.

The proposed array lens needs a more exhaustive experimental validation. One obvious step to do so is manufacturing a bigger array for performing beam scanning. Still, measuring a unit cell in infinite periodicity conditions is an alternative, achieved by fitting the unit cell into a rectangular waveguide [98], which will produce an impinging wave at an incidence angle dependent on the frequency. Also, since the simulation of SIW structures in HFSS requires so much computation power, an alternative simulation method must be contemplated –or developed– for faster and more efficient simulations, thus enabling the possibility of simulating the complete array lens.

Regarding the SIW phase shifters, improvements can be made in the cascaded configuration. Since it is easy to place two phase shifters on opposite layers of the SIW without affecting the size of the unit cell, the phase shifter could be improved by taking that into account and designing it specifically in that topology, using coupling coefficients different than 1 and distinct spacings that could increase the phase agility and reduce the insertion loss variation, even if it is at the expense of some matching. Also, the use of frequency selective surfaces operating in stop-band on SIW are of interest since they could facilitate the implementation of amplifiers [99], that could not only compensate the insertion losses,

but produce gain. Ideally, an amplifier would be inserted between the two cascaded phase shifters.

Figure 5.1: Picture of a manufactured half-mode SIW.

One aspect of the SIW that cannot be improved is the waveguide width, depending on the operating frequency and substrate thickness. Nevertheless, there is research concerning the development of circuits employing a half-mode SIW, in which the width is reduced in almost half by exciting a quasi-$TE_{0.5,0}$ mode, while maintaining the same waveguide-like properties [100]. Recent developments comprise the realization of miniaturized antennas [101], new methods for coupling radiating elements [102] and multilayer hybrid couplers [103]. The correct employment of this technology can potentially lead to a further reduction of the chip size of the array lens.

Finally, it can be taken into consideration that reflectarrays and lens arrays do not necessarily need to be fed by a far-field wave. A near-field feeding can reduce the antenna volume as it decreases the focal distance [104], and it is possible to accurately simulate the resulting radiation pattern [105]. This can also have a reconfigurability application: instead of using a fixed antenna as a feed, a tunable antenna may be employed for obtaining different near-field radiations, thus reducing the complexity of the reflector or lens, or increasing the number of possible applications. Research must be done to assess this possibility.

## 5.3. List of publications related to this work

The original work from this thesis has been featured in international journals and conferences, listed below.

### 5.3.1. International journals

- **P. Alcón**, N. Esparza, L. F. Herrán, F. Las-Heras, "Complex impedance transformers based on branch-line hybrid couplers", *Progress In Electromagnetics Research C*, vol. 69, pp. 147-157, 2016.

- **P. Alcón**, S. V. Hum, N. Esparza, L. F. Herrán, F. Las-Heras, "Substrate integrated waveguide phase shifter based on loaded tilted slots", *IEEE Microwave and Wireless Components Letters*, (Under review).

- Two additional journal papers are being prepared based on the work presented in this thesis. One is dedicated to the topologies for equalizing losses in reflection-type phase shifters, aiming for publication in the journal IEEE Transactions on Microwave Theory and Techniques. The other focuses on the design of a reflectarray cell with tunable stub and the effects of angles of incidence, for the journal IEEE Transactions on Antennas and Propagation.

### 5.3.2. International conferences

- **P. Alcón**, N. Esparza, L. F. Herrán, F. Las-Heras, "Analysis and design of a directional coupler with integrated matching network for reflective-type phase shifters", *2016 46th European Microwave Conference (EuMC)*, London, 2016, pp. 659-662.
- **P. Alcón**, N. Esparza, L. F. Herrán, F. Las-Heras, "On the design of generic matching networks in reflective-type phase shifters for antennas", *2015 9th European Conference on Antennas and Propagation (EuCAP)*, Lisbon, 2015, pp. 1-5.

## 5.4. Other publications

During the thesis period, two extra publications were realized on the subject of frequency selective surfaces: one international journal and one international conference.

- N. Esparza, **P. Alcón**, L. F. Herrán, F, Las-Heras, "Substrate integrated waveguides structures using frequency selective surfaces operating in stop-band (SBFSS-SIW)", *IEEE Microwave and Wireless Components Letters*, vol. 26, no. 2, pp. 113-115, Feb. 2016.
- N. Esparza, **P. Alcón**, L. F. Herrán, F, Las-Heras, "Design of substrate integrated waveguides structures based on stop-band response FSSs (SBFSS-SIW)", *2016 46th European Microwave Conference (EuMC)*, London, 2016, pp. 9-12.

## 5.5. Projects related to this work

Some of the work related to this thesis has contributed to the development of research projects.

- **"Técnicas de imaging mediante problema inverso de dispersión: nuevos algoritmos y técnicas de medida (iScat)"**, Code: TEC2011-24492, Funding: Ministerio de Economía y Competitividad (Spanish Goverment), Term: 01/01/2012 —31/12/2014. Main researcher: Fernando Las-Heras Andrés.
- **"Múltiples fuentes de información para mejorar técnicas de EM inverso para aplicaciones de reflectometría e imaging (MIRIIEM)"**, Code: TEC2014 -54005-P, Funding: Ministerio de Economía y Competitividad (Spanish Goverment), Term: 01/01/2015–31/12/2017. Main researchers: Marcos R. Pino and Luis Fernando H. Ontañón.

# References


[1] D. G. Berry, R. G. Malech, and W. A. Kennedy, "The reflectarray antenna," *IEEE Trans. Antennas Propag.*, pp. 645–651, Nov. 1963.

[2] J. Huang, "Microstrip reflectarray," in *Proc. Antennas Propag. Soc. Int. Symp. Dig.*, vol. 2, 1991, pp. 612–615.

[3] J. A. Encinar, "Recent advances in reflectarray antennas," in *Proceedings of the Fourth European Conference on Antennas and Propagation (EuCAP)*, 2010, pp. 1–6.

[4] S. V. Hum and J. P. Carrier, "Reconfigurable reflectarrays and array lenses for dyanmic antenna beam control: A review," *IEEE Trans. Antennas Propag.*, vol. 62, no. 1, pp. 183–198, Jan. 2014.

[5] H. Kamoda, T. Iwasaki, J. Tsumochi, and T. Kuki, "60-ghz electrically reconfigurable reflectarray using p-i-n diode," in *Microwave Symposium Digest*, 2009, pp. 1177–1180.

[6] H. Kamoda, T. Iwasaki, J. Tsumochi, T. Kuki, and O. Hashimoto, "60-ghz electronically reconfigurable large reflectarray using single-bit phase shifters," *IEEE Trans. Antennas Propag.*, vol. 59, no. 7, pp. 2524–2531, Jul. 2011.

[7] S. Montori, F. Cacciamani, C. Tomassoni, L. Marcacciol, and R. V. Gatti, "Novel 1-bit elementary cell for reconfigurable reflectarray antennas," in *41st European Microwave Conference (EuMC)*, 2011, pp. 1288–1291.

[8] A. E. Martynyuk, J. R. Zamudio, and N. A. Martynyuk, "Reflectarray based on three-bit spatial phase shifters: Mathematical model and technology of fabrication," in *Eucap 2009. 3rd European Conference on Antennas and Propagation*, 2009, pp. 2774–2778.

[9] F. A. Tahir, H. Aubert, and E. Girard, "Optimisation of mems-controlled reflectarray phase shifter cell," *IEEE Trans. Antennas Propag.*, vol. 5, no. 3, pp. 271–276, Feb. 2011.

[10] J. Perruisseau-Carrier, E. Girard, and H. Legay, "Analysis of reconfigurable reflectarray cell comprising a multitude of mems control elements," in *2010 Proceedings*

*of the Fourth European Conference on Antennas and Propagation (EuCAP)*, 2010, pp. 1–4.

[11] S. Montori, E. Chiuppesi, L. Marcaccioli, R. V. Gatti, and R. Sorrentino, "1-bit rf-mems-reconfigurable elementary cell for very large reflectarray," in *Mediterranean Microwave Symposium (MMS)*, 2010, pp. 98–101.

[12] B. Wu, M. Okoniewski, and M. E. Potter, "Design and fabrication of a ternary switch for mems-controlled reflectarray elements," *IEEE Antennas and Wireless Propagation Letters*, vol. 8, pp. 998–1001, 2009.

[13] L. Boccia, G. Amendola, and G. D. Massa, "Performance improvementt for a varactor-loaded reflectarray element," *IEEE Trans. Antennas Propag.*, vol. 58, no. 2, pp. 585–589, Feb. 2010.

[14] C. Liu and S. V. Hum, "An electronically tunable single-layer reflectarray antenna element with improved bandwidth," *IEEE Antennas and Wireless Propagation Letters*, vol. 9, pp. 1241–1244, 2010.

[15] M. Hajian, B. Kuijpers, K. Buisman, A. Akhnoukh, M. Plek, L. C. N. de Vreede, and J. Zijdeveld, "Active scan-beam reflectarray antenna loaded with tunable capacitor," in *3rd European Conference on Antennas and Propagation*, 2009, pp. 1158–1161.

[16] A. Moessinger, R. Marin, J. Freese, S. Mueller, A. Manabe, and R. Jakoby, "Investigations on 77 ghz tunable reflectarray unit cells with liquid crystal," in *First European Conference on Antennas and Propagation (EuCAP)*, 2006, pp. 1–4.

[17] R. Cahill, J. A. Encinar, M. Arrebola, R. Simms, R. Dickie, V. F. Fusco, and N. Mitchell, "Recent progress in electronically tunable reflectarray technology using liquid crystals," in *Proceedings of the 5th European Conference on Antennas and Propagation (EUCAP)*, 2011, pp. 2866–2870.

[18] A. Moessinger, S. Dieter, W. Menzel, S. Muellerr, and R. Jakoby, "Realization and characterization of a 77 ghz reconfigurable liquid crystal reflectarray," in *13th International Symposium on Antenna Technology and Applied Electromagnetics and the Canadian Radio Science Meeting (ANTEM/URSI)*, 2009, pp. 1–4.

[19] S. Bildik, S. Dieter, C. Fritzsch, M. Frei, C. Fischer, W. Menzel, and R. Jakoby, "Reconfigurable liquid crystal reflectarray with extended tunable phase range," in *41st European Microwave Conference (EuMC)*, 2011, pp. 1292–1295.

[20] G. Perez-Palomino, J. A. Encinar, M. Barba, and E. Carrasco, "Design and evaluation of multi-resonant unit cells based on liquid crystals for reconfigurable reflectarrays," *IET Microwaves Antennas & Propagation*, vol. 6, pp. 348–354, Feb. 2012.

[21] M. Sazegar, A. Giere, Y. Zheng, H. Maune, A. Moessinger, and R. Jakoby, "Reconfigurable unit cell for reflectarray antenna based on barium-strontium-titanate thick-film ceramic," in *European Microwave Conference*, 2009, pp. 598–601.

[22] Y. Shen, S. Ebadi, P. Wahid, and X. Gong, "Tunable reflectarray unit cell element using bst technology," in *IEEE Radio and Wireless Symposium (RWS)*, 2012, pp. 43–46.

[23] S. A. Long and G. H. Huff, "A fluidic loading mechanism for phase reconfigurable reflectarray elements," *IEEE Antennas and Wireless Propagation Letters*, vol. 10, pp. 876–879, 2011.

[24] E. Carrasco, M. Barba, and J. A. Encinar, "Electronically switchable-beam reflectarray antenna," in *Proceedings of the Fourth European Conference on Antennas and Propagation (EuCAP)*, 2010, pp. 1–5.

[25] E. Carrasco, M. Barba, and J. A. Encinar, "X-band reflectarray antenna with switching-beam using pin diodes and gathered elements," *IEEE Trans. Antennas Propag.*, vol. 60, no. 12, pp. 5700–5708, Dec. 2012.

[26] O. Bayraktar, O. A. Civi, and T. Akin, "Beam switching reflectarray monolithically integrated with rf mems switches," *IEEE Trans. Antennas Propag.*, vol. 60, no. 2, pp. 854–862, Feb. 2012.

[27] E. Carrasco, M. Barba, B. Reig, C. Dieppedale, and J. A. Encinar, "Characterization of a reflectarray gathered element with electronic control using ohmic rf mems and ppatches aperture-coupled to a delay line," *IEEE Trans. Antennas Propag.*, vol. 60, no. 9, pp. 4190–4021, 2012.

[28] T. Pochiraju and V. Fusco, "Amplitude and phase controlled reflectarray element based on impedance transformation unit," *IEEE Trans. Antennas Propag.*, vol. 57, no. 12, pp. 3821–3826, Dec. 2009.

[29] K. K. Kishor and S. V. Hum, "An amplifying reconfigurable reflectarrray antenna," *IEEE Trans. Antennas Propag.*, vol. 60, no. 1, pp. 197–205, Jan. 2012.

[30] F. Venneri, S. Costanzo, and G. D. Massa, "Reconfigurable aperture-coupled reflectarray element tuned by single varactor diode," *Electronics Letters*, vol. 48, no. 2, pp. 68–69, Jan. 2012.

[31] W. E. Kock, "Path-length microwave lenses," *Proc. IRE*, vol. 37, no. 8, pp. 852–855, Jan. 1949.

[32] D. M. Pozar, "Flat lens antenna concept using aperture coupled microstrip patches," *Electronic Letters*, vol. 32, no. 23, pp. 2109–2111, 1996.

[33] C. G. M. Ryan, M. R. Chaharmir, J. Shaker, J. R. Bray, Y. M. M. Antar, and A. Ittipiboon, "A widebandd transmitarray using dual-resonant double square rings," *IEEE Trans. Antennas Propag.*, vol. 58, no. 5, pp. 1486–1493, 2010.

[34] A. Abbaspour-Tamijani, K. Sarabandi, and G. M. Rebeiz, "Antenna-filter-antenna arrays as a class of bandpass frequency-selective surfaces," *IEEE Trans. Microw. Theory Techn.*, vol. 52, no. 8, pp. 1781–1789, Aug. 2004.

[35] P. P. de la Torre and M. Sierra-Castaner, "Electronically reconfigurable patches for transmit-array structures at 12 ghz," in *2008 IEEE Antennas and Propagation Society International Symposium*, 2008, pp. 1–4.

[36] J. Y. Lau and S. V. Hum, "Analysis and characterization of a multipole reconfigurable transmitarray element," *IEEE Trans. Antennas Propag.*, vol. 59, no. 1, pp. 70–79, Jan. 2011.

[37] J. Y. Lau and S. V. Hum, "Reconfigurable transmitarray design approaches for beamforming applications," *IEEE Trans. Antennas Propag.*, vol. 60, no. 12, pp. 5679–5689, Dec. 2012.

[38] P. Padilla, A. Muñoz-Acevedo, M. Sierra-Castañer, and M. Sierra-Pérez, "Electronically reconfigurable transmitarray at ku band for microwave applications," *IEEE Trans. Antennas Propag.*, vol. 58, no. 8, pp. 2571–2579, Aug. 2010.

[39] C. Huang, W. Pan, X. Ma, B. Zhao, J. Cui, and X. Luo, "Using reconfigurable transmitarray to achieve beam-steering and polarization manipulation applications," *IEEE Trans. Antennas Propag.*, vol. 63, no. 11, pp. 4801–4810, Nov. 2015.

[40] C. C. Cheng, B. Lakshminarayanan, and A. Abbaspour-Tamijani, "A programmable lens-array antenna with monolithically integrated mems switches," *IEEE Trans. Microw. Theory Techn.*, vol. 57, no. 8, pp. 1874–1884, Aug. 2011.

[41] U. Mayer, M. Wickert, N. Joram, J. Wagner, R. Eickhoff, I. Santamaria, C. Scheytt, C., and R. Kraemer, "Integrated adjustable phase shifters," *IEEE Microwave Magazine*, vol. 11, no. 6, pp. 97–108, 2010.

[42] R. V. Garver, "360° varactor linear phase modulator," *IEEE Trans. Microw. Theory Techn.*, vol. 17, no. 3, pp. 137–147, Mar. 1969.

[43] Y. H. Liew, "A novel 360° analog phase shifter with linear voltage phase relationship," in *1999 Asia Pacific Microwave Conference*, vol. 1, 1999, pp. 17–20.

[44] J. Upshur and B. Geller, "Low-loss 360° x-band analog phase shifter," *IEEE MTT-S International Microwave Symposium Digest*, vol. 1, pp. 487–490, 1990.

[45] F. Ellinger, R. Vogt, and W. Bachtold, "Ultracompact reflective-type phase shifter mmic at c-band with 360° phase-control range for smart antenna combining," *IEEE Journal of Solid-State Circuits*, vol. 37, no. 4, pp. 481–486, 2002.

[46] C. Charles and D. Allstot, "A 2-ghz integrated cmos reflective-type phase shifter with 675° control range," in *IEEE International Symposium on Circuits and Systems*, 2006.

[47] H. Zarei, C. T. Charles, and D. J. Allstot, "Reflective-type phase shifters for multiple-antenna transceivers," *IEEE Trans. Circuits Syst.*, vol. 54, no. 8, pp. 1647–1656, Aug. 2007.

[48] C. Toker, M. Saglam, M. Ozme, and N. Gunalp, "Branch-line couplers using unequal line lengths," *IEEE Trans. Microw. Theory Techn.*, vol. 49, no. 4, pp. 718–721, 2001.

[49] S. Cheng, E. Ojefors, P. Hallbjorner, and A. Rydberg, "Compact reflective microstrip phase shifter for traveling wave antenna applications," *IEEE Microw. Wireless Compon. Lett.*, vol. 16, no. 7, pp. 431–433, Jul. 2006.

[50] K. Miyaguchi, M. Hieda, K. Nakahara, H. Kurusu, M. Nii, M. Kasahara, T. Takagi, and S. Urasaki, "An ultra-broad-band reflection-type phase-shifter mmic with series and parallel lc circuits," *IEEE Transactions on Microwave Theory and Techniques*, vol. 49, no. 12, pp. 2446–2452, 2001.

[51] K. Hettak and G. A. Morin, "Compact variable reflective-type sige phase shifter using lumped elements for 5 ghz applications," in *2010 European Microwave Integrated Circuits Conf. (EuMIC)*, Sep. 27–28, 2010, pp. 102–105.

[52] David M. Pozar, *Microwave Engineering.* Wiley, 1990.

[53] R. Gupta, S. Anderson, and W. Getsingert, "Impedance-transforming 3-db 90° hybrids," *IEEE Trans. Microw. Theory Techn.*, vol. 35, no. 12, pp. 1303–1307, Dec. 1987.

[54] Q. Wang, J. Lim, and Y. Jeong, "Design of a compact dual-band branch line coupler using composite right/left-handed transmission lines," *Electronic Letters*, vol. 52, no. 8, pp. 630–631, Apr. 2016.

[55] H. Kim, H. Wi, S. Wang, J. Kim, and W. Jung, "Broadband 3 db microstrip hybrid coupler with low dielectric substrate for x-band applications," in *2016 IEEE 17th Annual Wireless and Microwave Technology Conference (WAMICON)*, 2016, pp. 1–3.

[56] Y. Morimoto, A. Waghmare, K. Dhwaj, and T. Itho, "A compact branch line coupler using novel periodically grounded slow-wave structure," in *2016 IEEE MTT-S International Microwave Symposium (IMS)*, 2016, pp. 1–3.

[57] K. E. K. Hettak, "3d ultra miniature mmic tfms 90° coupler fabricated with a standard air bridge process," in *Microwave Conference (EuMC), 2011 41st European*, 2011, pp. 846–849.

[58] M. Nosrati, "An extremely miniaturized microstrip branch-line coupler," *Microw. Opt. Technol. Lett.*, vol. 51, no. 6, pp. 1403–1406, Jun. 2009.

[59] Y. S. Wong, S. Y. Zheng, and W. S. Chan, "Multifolded bandwidth branch line coupler with filtering characteristic using coupled port feeding," *Progress In Electromagnetics Research*, vol. 118, pp. 17–35, 2011.

[60] Y. J. Cheng, L. Wang, J. Wu, and Y. Fan, "Directional coupler with good restraint outside the passband and its frequency-agile application," *Progress In Electromagnetics Research*, vol. 135, pp. 759–771, 2013.

[61] C. Gai, Y. C. Jiao, and Y. L. Zhao, "Compact dual-band branch-line coupler with dual transmission lines," *IEEE Microw. Wireless Compon. Lett.*, vol. 26, no. 5, pp. 325–327, May 2016.

[62] J. Reed and G. J. Wheeler, "A method of analysis of symmetrical four-port networks," *IEEE Trans. Microw. Theory Techn.*, vol. 4, no. 4, pp. 246–252, Oct. 1956.

[63] C. S. Lin, S. F. Chang, C. C. Chang, and Y. H. Shu, "Design of a reflection-type phase shifter with wide relative phase shift and constant insertion loss," *IEEE Trans. Microw. Theory Techn.*, vol. 55, no. 9, pp. 1862–1868, Sep. 2007.

[64] C. S. Lin, S. F. Chang, and W. C. Hsiao, "A full-360° reflection-type phase shifter with constant insertion loss," *IEEE Microw. Wireless Compon. Lett.*, vol. 18, no. 2, pp. 106–108, Feb. 2008.

[65] Ramesh Garg, *Microstrip Antenna Design Handbook*. Artech House, 2001.

[66] Arun K. Bhattacharyya, *Phased Array Antennas*. Wiley, 2006.

[67] "HFSS," http://www.ansys.com/products/electronics/ansys-hfss, accessed: Mars 29, 2017.

[68] E. Almajali, D. A. McNamara, J. Shaker, and M. R. Chaharmir, "Derivation and validation of the basic design equations for symmetric sub-reflectarrays," *IEEE Trans. Antennas Propag.*, vol. 60, no. 2, pp. 2336–2346, Feb. 2012.

[69] E. Almajali, D. A. McNamara, J. Shaker, and R. Chaharmir, "On beam squint in offset-fed reflectarrays," *IEEE Antennas Wireless Propag. Lett.*, vol. 11, pp. 937–940, 2012.

[70] E. R. F. Almajali and D. A. McNamara, "Angle of incidence effects in reflectarray antenna design: Making gain increases possible by including incidence angle effects," *IEEE Antennas Propag. Mag.*, vol. 58, no. 5, pp. 52–64, Oct. 2016.

[71] John Huang, Jose Antonio Encinar, *Reflectarray Antennas*. Wiley, 2007.

[72] M. Bozzi, A. Georgiadis, and K. Wu, "Review of substrate-integrated waveguide circuits and antennas," *IET Microwaves, Antennas & Propagation*, vol. 5, no. 8, pp. 909–920, Jun. 2011.

[73] Y. Cassivi, L. Perregrini, P. Arcioni, M. Bressan, K. Wu, and G. Conciauro, "Dispersion characteristics of substrate integrated rectangular waveguide," *IEEE Microw. Wireless Compon. Lett.*, vol. 12, no. 9, pp. 333–335, Sep. 2002.

[74] W. Che, K. Deng, D. Wang, and Y. Chow, "Analytical equivalence between substrate-integrated waveguide and rectangular waveguide," *IET Microw. Antennas Propag.*, vol. 2, no. 1, pp. 35–41, Feb. 2008.

[75] F. Xu and K. Wu, "Guided-wave and leakage characteristics of substrate integrated waveguide," *IEEE Trans. Microw. Theory Techn.*, vol. 53, no. 1, pp. 66–73, Jan. 2005.

[76] M. Bozzi, M. Pasian, L. Perregrini, and K. Wu, "On the losses in substrate integrated waveguides and cavities," *Int. J. Microw. Wirel. Technol.*, vol. 1, no. 5, pp. 395–401, 2009.

[77] D. Deslandes and K. Wu, "Integrated microstrip and rectangular waveguide in planar form," *IEEE Microw. Wireless Compon. Lett.*, vol. 11, no. 2, pp. 68–70, Aug. 2001.

[78] D. Deslandes, "Design equations for tapered microstrip-to-substrate integrated waveguide transitions," in *IEEE MTT-S Int. Microwave Symp. Digest*, 2010, pp. 704–707.

[79] W. M. A. Wahab, D. Busuioc, and S. Safavi-Naeini, "Low cost planar waveguide technology-based dielectric resonator antenna (dra) for millimeter-wave applications: Analysis, design, and fabrication," *IEEE Trans. Antennas Propag.*, vol. 58, no. 8, pp. 2499–2507, Aug. 2010.

[80] Z. C. Hao, W. Hong, J. X. Chen, H. X. Zhou, and K. Wu, "Single-layer substrate integrated waveguide directional couplers," *IEEE Antennas Propag. Mag.*, vol. 153, no. 5, pp. 426–431, Oct. 2006.

[81] W. M. Abdel-Wahab and S. Safavi-Naeini, "Low loss h-shape siw hybrid coupler for millimeter-wave phased arrays antenna systems," in *Proceedings of the 2012 IEEE International Symposium on Antennas and Propagation*, 2012, pp. 1–2.

[82] T. Djerafi and K. Wu, "Super-compact substrate integrated waveguide cruciform directional coupler," *IEEE Microw. Wireless Compon. Lett.*, vol. 17, no. 11, pp. 757–759, Nov. 2007.

[83] Y. Ding and K.Wu, "Varactor–tuned substrate integrated waveguide phase shifter," in *2011 IEEE MTT-S International Microwave Symposium*, Jun. 5–10, 2011, pp. 1–4.

[84] E. Sbarra, L. Marcaccioli, R. V. Gatti, and R. Sorrentino, "Ku-band analogue phase shifter in siw technology," in *2009 European Microwave Conference (EuMC)*, 2009, pp. 264–267.

[85] A. Khidre, F. Yang, and A. Z. Elsherbeni, "A patch antenna with a varactor-loaded slot for reconfigurable dual-band operation," *IEEE Trans. Antennas Propag.*, vol. 63, no. 2, pp. 755–760, Feb. 2015.

[86] M. Norooziarab, Z. Atlasbaf, M. Rafaei-Booket, and F. Farzami, "A tunable transmission line based on an siw loaded by a new single-cell metamaterial," in *Telecommunications (IST), 2012 Sixth International Symposium on*, Nov. 6–8, 2012, pp. 75–79.

[87] A. Ali, F. Coccetti, H. Aubert, and N. J. G. Fonseca, "Novel multi-layer siw broadband coupler for nolen matrix design in ku band," in *2008 IEEE Antennas and Propagation Society International Symposium*, Jul. 5–11, 2008, pp. 1–4.

[88] M. A. Abdalla, W. Wahba, H. Elregaily, A. A. Allam, and A. A. Nazir, "A compact and wide band siw metamaterial impedance transformer," in *Antennas and Propagation (MECAP), 2012 Middle East Conference on*, Dec. 29–31, 2012, pp. 1–5.

[89] F. Carrera, D. Navarro, M. Baquero-Escudero, and V. M. Rodrigo-Peñarrocha, "Compact substrate integrated waveguide directional couplers in ku and k bands," in *The 40th European Microwave Conference*, Sep. 28–30, 2010, pp. 1178–1181.

[90] Q. Wang, J. Lim, and Y. Jeon, "Design of a compact dual-band branch line coupler using composite right/left-handed transmission lines," *Electronics Letters*, vol. 52, no. 8, pp. 630–631, Apr. 2016.

[91] H. Kim, H. Wi, S. Wang, J. Kim, and W. Jung, "Broadband 3 db microstrip hybrid coupler with low dielectric substrate for x-band applications," in *2016 IEEE 17th Annual Wireless and Microwave Technology Conference (WAMICON)*, 2016, pp. 1–3.

[92] Y. Morimoto, A. Waghmare, K. Dhwaj, and T. Itho, "A compact branch line coupler using novel periodically grounded slow-wave structure," in *2016 IEEE MTT-S International Microwave Symposium (IMS)*, 2016, pp. 1–3.

[93] K. Hettak and K. Elgaid, "3d ultra miniature mmic tfms 90° coupler fabricated with a standard air bridge process," in *Microwave Conference (EuMC), 2011 41st European*, 2011, pp. 846–849.

[94] M. Nosrati, "An extremely miniaturized microstrip branch-line coupler," *Microwave and Optical Technology Letters*, vol. 51, no. 6, pp. 1403–1406, Jun. 2009.

[95] Y. Wong, S. Zheng, and W. Chan, "Multifolded bandwidth branch line coupler with filtering characteristic using coupled port feeding," *Progress In Electromagnetics Research*, vol. 118, pp. 17–35, 2011.

[96] Y. Cheng, L. Wang, J. Wu, and Y. Fan, "Directional coupler with good restraint outside the passband and its frequency-agile application," *Progress In Electromagnetics Research*, vol. 135, pp. 759–771, 2013.

[97] C. Gai, Y. Jiao, and Y. Zhao, "Compact dual-band branch-line coupler with dual transmission lines," *IEEE Microw. Wireless Compon. Lett.*, vol. 26, no. 5, pp. 325–327, May 2016.

[98] P. Hannan and M. Balfour, "Simulation of a phased-array antenna in waveguide," *IEEE Trans. Antennas Propag.*, vol. 13, no. 3, pp. 342–353, 1965.

[99] N. Esparza, P. Alcón, L. F. Herrán, and F. Las-Heras, "Substrate integrated waveguides structures using frequency selective surfaces operating in stop-band (sbfss-siw)," *IEEE Microw. Wireless Compon. Lett.*, vol. 26, no. 5, pp. 325–327, May 2016.

[100] Q. Lai, C. Fumeaux, W. Hong, and R. Vahldieck, "Characterization of the propagation properties of the half-mode substrate integrated waveguide," *IEEE Trans. Microw. Theory Techn.*, vol. 57, no. 8, pp. 1996–2004, Aug. 2009.

[101] S. Banerjee, B. Rana, S. K. Parui, S. Chatterjee, and N. Dey, "Hmsiw-based miniaturized sensing antennas for s- and c-band applications," *IEEE Sensors Letters*, vol. 1, no. 1, pp. 1–5, Feb. 2017.

[102] G. V. K. Reddy, S. Mukherjee, and A. Biswas, "Design of hmsiw fed dual frequency microstrip patch antenna for x-band applications," in *2016 IEEE International Symposium on Antennas and Propagation (APSURSI)*, 2016, pp. 203–204.

[103] Z. Zhang, Y. Fan, Y. Cheng, and Y. Zhang, "A novel multilayer e-plane half-mode substrate integrated waveguide (hmsiw) 3-db coupler with improved out-of-band rejection," in *2016 Progress in Electromagnetic Research Symposium (PIERS)*, 2016, pp. 1088–1091.

[104] S. B. Cho, E. S. Jo, and D. Kim, "A novel method to reduce physical dimensions of reflectarray antennas using near-field feeding," in *2016 URSI Asia-Pacific Radio Science Conference (URSI AP-RASC)*, 2016, pp. 1296–1298.

[105] M. Arrebola, Y. Alvarez, J. A. Encinar, and F. Las-Heras, "Accurate analysis of printed reflectarrays considering the near field of the primary feed," *IEEE Trans. Antennas Propag.*, vol. 3, no. 2, pp. 187–194, Mar. 2009.